

A FAST DYNAMIC SMOOTH ADAPTIVE MESHING SCHEME WITH APPLICATIONS TO COMPRESSIBLE FLOW

RAAGHAV RAMANI
 Department of Mathematics
 University of California
 Davis, CA 95616 USA
rramani@math.ucdavis.edu

STEVE SHKOLLER
 Department of Mathematics
 University of California
 Davis, CA 95616 USA
shkoller@math.ucdavis.edu

May 20, 2022

Abstract

We develop a fast-running smooth adaptive meshing (SAM) algorithm for dynamic curvilinear mesh generation, which is based on a fast solution strategy of the time-dependent Monge-Ampère (MA) equation, $\det \nabla \psi(x, t) = G \circ \psi(x, t)$. The novelty of our approach is a new so-called *perturbation formulation* of MA, which constructs the solution map ψ via composition of a sequence of near identity deformations of a uniform reference mesh. This allows us to utilize a simple, fast, and high order accurate implementation of the deformation method [21]. We design SAM to satisfy both internal and external consistency requirements between stability, accuracy, and efficiency constraints, and show that the scheme is of optimal complexity when applied to time-dependent mesh generation for solutions to hyperbolic systems such as the Euler equations of gas dynamics. We perform a series of challenging mesh generation experiments for grids with large deformations, and demonstrate that SAM is able to produce smooth meshes comparable to state-of-the-art solvers [22, 18], while running approximately 50-100 times faster. The SAM algorithm is then coupled to a simple Arbitrary Lagrangian Eulerian (ALE) scheme for 2D gas dynamics. Specifically, we implement the C -method [66, 67] and develop a new ALE interface tracking algorithm for contact discontinuities. We perform numerical experiments for both the Noh implosion problem as well as a classical Rayleigh-Taylor instability problem. Results confirm that low-resolution simulations using our SAM-ALE algorithm compare favorably with high-resolution uniform mesh runs.

CONTENTS

1	Introduction	2
1.1	Mesh redistribution	4
1.2	Prescribing the Jacobian determinant	4
1.3	Fast Smooth Adaptive Meshing	5
1.4	Application to ALE gas dynamics	6
1.5	Outline	6
2	Preliminaries	7
2.1	Domains, meshes, and mappings	7
2.2	Eulerian and ALE variables	8
2.3	Derivatives and important geometric quantities	8
2.4	Computational platform and code optimization	9
3	Fast static adaptive meshing	9
3.1	Mathematical formulation of static mesh generation	9
3.2	The basic mesh generation procedure via the deformation method	10

3.3	Numerical solution of the Poisson problem	12
3.4	Numerical solution of the flowmap equation	13
3.5	Error analysis	14
3.6	Algorithmic complexity and CPU runtime	18
3.7	Benchmarking against a state-of-the-art mesh generation scheme	22
4	Fast dynamic adaptive meshing	25
4.1	Dynamic formulation	25
4.2	Reformulation in terms of near-identity maps	26
4.3	Restarted dynamic mesh generation	28
4.4	Numerical implementation aspects	28
5	Dynamic mesh generation experiments	29
5.1	Static mesh with large zoom-in factor	30
5.2	Propagating circular front	30
5.3	Uniformly rotating patch	31
5.4	Differential rotation with small scales	35
6	SAM-ALE scheme for gas dynamics	36
6.1	The 2D ALE-Euler system	36
6.2	The C-method for 2D ALE-Euler	39
6.3	Coupled SAM-ALE algorithm	42
7	SAM-ALE simulations of gas dynamics	42
7.1	Noh implosion	42
7.2	Rayleigh-Taylor instability	45
	Appendices	47
	Appendix A The C-method for 2D ALE-Euler	47
	Appendix B Boundary smoothing for non-Neumann functions	50
	Appendix C The MK scheme	50
	C.1 Machine comparison	50
	Acknowledgements	51
	References	58

1. INTRODUCTION

The efficiency of smooth moving-mesh methods for numerical simulations of gas dynamics¹ and related systems has been investigated in recent years [3, 86, 36, 37, 64, 60, 26, 51, 27]; however, to the best of our knowledge, compelling evidence of the gain in efficiency relative to fixed uniform-mesh simulations in multiple space dimensions have rarely been provided. In a recent result [51], the authors demonstrate that low-resolution adaptive simulations are roughly 2-6 times faster than high-resolution uniform simulations of comparable quality; most results in this area focus on novel solution methodologies but not on the ultimate speed-up that may be gained by the algorithms that they produce. The papers cited above focus on one half of the moving-mesh methodology, namely, the numerical discretization of the physical PDEs. They develop state-of-the-art high-resolution shock-capturing techniques, but use well-established and somewhat standard meshing algorithms. Our point-of-view is that it is essential to simultaneously develop both numerical methods for hyperbolic systems (for discontinuous solutions) as well as novel meshing strategies.²

¹Moving-mesh simulations are often referred to as *adaptive simulations* and we shall use this terminology herein.

²This philosophy is in agreement with [64], in which the authors state that the main obstacle in their moving-mesh simulations is the lack of a simple, robust, and efficient algorithm for dynamic and smooth adaptive mesh generation, particularly in 3D geometries, and for multi-phase flows with unstable interfaces.

Herein, we propose a novel and fast³ Smooth Adaptive Meshing (SAM) algorithm for multi- D simulations requiring mesh adaptivity. We present adaptive-simulation speed-up results for two classical but extremely challenging gas dynamic problems: the Noh shock implosion problem, and the (highly unstable) Rayleigh-Taylor (RT) problem. For the Noh problem, our adaptive simulations are free of the numerous numerical anomalies that are present in almost all reported results, while running approximately 6 times faster than a comparable uniform-mesh simulation. The four-fold speed-up provided by SAM for the RT problem is, to the best of our knowledge, the first of its kind.⁴

Solutions to nonlinear conservation laws exhibit a wide range of dynamically evolving and interacting spatial scales, and static uniform (i.e. Eulerian) meshes are both inaccurate and inefficient at representing small scale solution structures. The most well-developed of adaptive mesh methods are so-called h -refinement methods, widely used in many commercial codes [71, 10, 30, 31]. In these adaptive mesh refinement (AMR) methods, an initially uniform mesh is locally dyadically refined (coarsened) via the addition (deletion) of node points [5, 61]. These methods have by now been developed to a high degree of sophistication and are widely used in many different applications. However, they necessarily involve the use of time-dependent data structures and are thus rather complicated to implement in a fluids code.

A more serious issue lies with the dyadic refinement at the heart of AMR schemes, which results in an artificially discontinuous transition from coarse scale to fine scale representation of numerical solutions on AMR meshes. Several theoretical and numerical studies [5, 79, 58] have demonstrated the spurious reflection, refraction, and scattering of waves that propagate across discontinuously refined grids. This is a particular problem for advection-dominated flows, such as large-scale atmospheric and oceanic dynamics simulations, which require the accurate transport of acoustic and inertial-gravity waves. Similarly, many problems in gas dynamics, such as self-similar implosions and unstable contact discontinuities, are extremely sensitive to small perturbations. Spurious wave reflections due to discontinuously refined grids corrupt these numerical solutions, with the anomalies persisting, or even worsening, as the mesh is globally refined [30, 77].

A simple alternative to AMR is to keep the number of cells fixed and instead move individual nodes in the mesh to concentrate near features of interest. Lagrangian-type schemes move mesh points with the velocity of the fluid, thereby providing a simple way to track material interfaces and free surfaces. However, when the flow has strong vorticity, Lagrangian grids are highly distorted or tangled i.e. some cells in the grid are non-convex or have folded over, at which point the simulation breaks down.

Arbitrary Lagrangian Eulerian (ALE) methods aim to mitigate the problem of mesh tangling. In the *indirect* ALE approach, the mesh points are first moved in a Lagrangian fashion, then subsequently rezoned to untangle grid points that may have crossed each other during the Lagrangian phase. Finally, a remapping phase is employed to transfer the solution from the old mesh to the new mesh. The rezoning phase is usually the most difficult [59], and current rezoning strategies are somewhat heuristic in nature [47]. In this work, we consider the *direct* ALE approach, in which an adaptive mesh is generated directly without any initial Lagrangian phase or subsequent mesh rezoning. For simplicity, we consider $2D$ tensor product meshes and develop a novel fast numerical

³We will demonstrate that our SAM algorithm is the first to be able to solve classical Rayleigh-Taylor problems on coarse, but adaptive, grids faster than simulations on uniform grids.

⁴Most attempts at using moving-mesh adaptivity to numerically simulate the RT instability result in runs that prematurely blow-up due to mesh tangling, meaning that those algorithms are not sufficiently stable to provide a competitive speed-up factor. Recent papers [59, 4] instead focus on novel and sophisticated meshing techniques with the goal of simply simulating the RT instability until the final simulation time without the code crashing; however, these meshing algorithms are too expensive to provide speed-up over uniform-mesh simulations.

algorithm for smooth adaptive mesh generation for ALE gas dynamics simulations. Our fast Smooth Adaptive Meshing (SAM) scheme utilizes a *mesh redistribution* procedure, in which mesh points are smoothly relocated to regions of interest, while keeping the number of cells and mesh topology fixed. In the rest of this section, we describe in further detail some aspects of our numerical method.

1.1. Mesh redistribution

Our SAM scheme falls under the category of r -refinement schemes, or adaptive mesh redistribution methods. In contrast to Lagrangian-rezone methods, a grid is generated via a user-prescribed monitor function which determines the grid size and orientation. High-resolution representation of numerical solutions is obtained by defining the monitor function appropriately, e.g., using solution derivatives. Moreover, the adaptive grids can be generated to align with the geometry of evolving fronts [40], and to naturally capture self-similar dynamics or scale-invariant structures [12, 11].

Historically, the first r -refinement methods were based on the variational approach, examples of which include the equipotential [82], variable diffusion [83], cost function [6], and harmonic mapping [28] methods. The variational approach also currently appears to be the method of choice for use in direct ALE schemes, several of which employ the popular MMPDE framework [41, 49]. These variational methods, however, require the accurate numerical solution of a coupled set of d complicated nonlinear auxiliary PDEs in \mathbb{R}^d , for which simple, fast, and accurate algorithms are in general not available. For these reasons, among others, r -refinement methods have yet to become incorporated into large scale established hydrodynamics codes. See, for example, [42, 13, 22, 18] and the references therein for thorough reviews of r -adaptive methods and their associated difficulties.

1.2. Prescribing the Jacobian determinant

The fundamental guiding principle for smooth adaptive mesh generation is control of the local cell volume of the adaptive grid. In the time-dependent multi- D setting, we assume that we have a given smooth positive *target Jacobian function* $\mathbf{G}(x, t)$ describing the size of the cells in the moving target adaptive mesh. We then seek to construct a diffeomorphism $\psi(x, t)$ mapping a uniform mesh to the target mesh by requiring that $\det \nabla \psi(x, t) = \mathbf{G}(\psi(x, t), t)$. A semi-discretization in time yields a sequence of nonlinear elliptic equations of Monge-Ampère (MA) type

$$\det \nabla \psi_k(x) = \mathbf{G}_k(\psi_k(x)), \quad (1)$$

where each \mathbf{G}_k is again a given positive target Jacobian function. Each map ψ_k deforms the uniform mesh and causes mesh contraction in regions where \mathbf{G}_k is small, and mesh expansion in regions where \mathbf{G}_k is large.

Solutions to the MA equation are unique in $1D$ and the associated $1D$ grids are therefore uniquely determined. For $d \geq 2$, however, the single scalar MA equation is insufficient to determine the map ψ since there are multiple degrees of freedom per cell i.e. 3 components of $\nabla \psi$ in $2D$, and 8 components in $3D$.

The question then becomes how to choose a particular solution ψ that is in some sense optimal. One such choice that has received a great deal of attention in recent years is the Monge-Kantorovich (MK) formulation based on optimal transport, in which a map ψ is (uniquely [8, 16]) constructed to minimize the L^2 displacement of the mesh points. This is attractive from a numerical perspective, since smaller grid velocities can reduce interpolation and other numerical errors [50].

On the other hand, the MK formulation results in a fully nonlinear second order elliptic equation, whose numerical solution is difficult to obtain. One approach is to consider a parabolized formulation by introducing an artificial time variable τ then iterating until a steady state is reached [73, 9]. In

this case, the Jacobian constraint is only satisfied in the asymptotic limit $\tau \rightarrow \infty$, and many iterations may be required to obtain a sufficiently accurate solution, particularly for target meshes with large deformations. An alternative, fully nonlinear approach using preconditioned Newton-Krylov solvers is designed in [22, 18], leading to a robust, scalable algorithm that is, to the best of our knowledge, the state-of-the-art in the field. However, the Newton-Krylov iterative approach is still relatively slow for our ultimate goal of efficient adaptive gas dynamics simulations; specifically, its implementation in our ALE scheme (to be described below) leads to adaptive mesh simulations with computational runtimes greater than would otherwise be obtained with a uniformly high-resolution mesh, thereby defeating the purpose of using an adaptive meshing scheme in the first place.

1.3. Fast Smooth Adaptive Meshing

Our SAM scheme, like the MK scheme, constructs a diffeomorphism ψ as the solution to the nonlinear Monge-Ampère equation. We construct each map ψ_k to optimize for algorithmic efficiency, in contrast to the MK approach which chooses ψ_k to minimize the average mesh displacement. The key to our fast algorithm is a new *perturbation formulation* of (1) along with an efficient implementation of the deformation method [21]. As will be demonstrated in Section 3, the deformation method constructs a solution to the nonlinear Monge-Ampère equation via a single elliptic solve for a linear Poisson problem, along with the integration of an ODE for a flowmap $\eta(x, \tau)$ between pseudo-time $\tau = 0$ and $\tau = 1$.

In contrast to other methods [68, 33], our perturbation formulation constructs each map ψ_{k+1} as the image of the map ψ_k acting on a *near identity deformation* $\delta\psi_{k+1} \approx e$ of a uniform reference mesh. The formulation on a uniform mesh is crucial, since it enables the use of simple, efficient, and high-order accurate spectral solvers and interpolation schemes for the linear Poisson problem and flowmap integration. Our perturbation formulation additionally extends in a straightforward way to a “multilevel” algorithm that is capable of producing smooth meshes with very large zoom-in factors, thereby permitting high-resolution representation of small scale structures with few mesh points.

The fast implementation of our dynamic meshing scheme in turn relies upon a fast static meshing scheme. The numerical implementation of the static deformation method has been investigated in several previous works by Liao and coworkers [52, 56, 53]. In this work, we present a new framework for understanding the stability, accuracy, and efficiency of the deformation method based on simple error analysis and convergence tests. Our analysis leads us to design a simple, fast, stable, and high-order accurate algorithm using standard and widely available numerical methods. In particular, we propose an efficient spectral solver with boundary smoothing for the Poisson equation, and standard RK4 time integration with an optimized bicubic interpolation routine for the flowmap equation. A key implication of our numerical design choices for SAM is an internal consistency between stability, accuracy, and efficiency constraints, as well as an external consistency with the stability condition associated with ALE gas dynamics. As we shall demonstrate, this internal and external consistency results in a numerical SAM algorithm with optimal complexity for hyperbolic systems.

Our SAM algorithm is approximately two orders of magnitude faster than the MK nonlinear solvers [22, 18], and the computed numerical solutions exhibit both greater accuracy as well as better convergence rates under global mesh refinement. While SAM grids are produced without any optimization of specific grid properties, we show that they have similar levels of average grid displacement and distortion as the “optimal” MK grids, which we note are only optimal in the asymptotic limit of zero mesh spacing. We perform a number of challenging mesh generation experiments designed to replicate flows with high vorticity and large deformations, and demonstrate that the meshes produced with our dynamic SAM scheme are smooth and accurate.

1.4. Application to ALE gas dynamics

To demonstrate the efficacy of our SAM scheme in practical applications, we formulate a simple coupled SAM-ALE method for $2D$ gas dynamics. Several moving-mesh methods for the $2D$ Euler system have been developed based on the MMPDE approach and finite volume (FV) and finite element (FE) methods [74, 75]. A formulation on smooth tensor product meshes enables the use of finite difference (FD) methods, which are both simpler and more efficient than FV and FE methods⁵, and have been investigated in several recent papers [62, 46, 51]. In this work, we further develop the C -method [66, 67], a simplified WENO-based solver with space-time smooth nonlinear artificial viscosity and explicit tracking of material interfaces.

Special care is given to the so-called *geometric conservation law* (GCL), and we show that our nonlinear WENO reconstruction procedure respects the free-stream preservation property on adaptive meshes. The C -method dynamically tracks the location and geometry of evolving fronts, and is used to add both directionally isotropic and anisotropic artificial viscosity to shocks and contacts. Herein, we implement the C -method in the ALE context and introduce a new ALE front-tracking algorithm for contact discontinuities, which we subsequently use to construct suitable target Jacobian functions for SAM. Previous works have mainly investigated target Jacobian functions constructed based on interpolation errors [43, 40], or weighted combinations of solution gradient estimates [78], which sometimes fail to capture small scale vortical structures [74]. Our simple ALE front-tracking algorithm, in contrast, allows us to generate smooth adaptive meshes that capture small scale Kelvin-Helmholtz roll-up zones in unstable RT problems. We apply our coupled SAM-ALE scheme to two challenging test problems, namely the Noh implosion and RT instability. For the Noh problem, we find that the 50×50 SAM-ALE solution is more accurate than the 200×200 uniform solution, while running approximately 6 times faster. Moreover, the SAM-ALE solution is completely free of spurious numerical anomalies, such as lack of symmetry, unphysical oscillations, and wall-heating. For the RT problem, we find that the 64×128 SAM-ALE solution is comparable to the 256×512 uniform solution, while running 4 times faster.

1.5. Outline

Section 2 introduces notation and definitions that will be used throughout the paper. In Section 3, we develop the basic SAM algorithm for static mesh generation, upon which we shall build our dynamic scheme. We present some basic error analysis and computational complexity studies, and benchmark the algorithm against the MK scheme. In Section 4, we consider dynamic mesh generation and introduce the perturbation formulation of the (MA) system. We show that the basic SAM algorithm can be applied to the modified system, resulting in a fast dynamic SAM algorithm. We then perform, in Section 5, a series of challenging mesh generation experiments to demonstrate the capabilities of the scheme. In Section 6, we formulate a simple coupled SAM-ALE scheme for the $2D$ compressible Euler system, and describe some aspects of our numerical method. Finally, in Section 7, we apply SAM-ALE to the Noh and RT test problems and compare the results with low-resolution and high-resolution uniform solutions. Three sections are included in the Appendices: the first concerns the C -method regularization for the $2D$ ALE-Euler system, the second describes a simple boundary smoothing technique, and the third provides a machine comparison test for the purposes of benchmarking our SAM algorithm.

⁵FV schemes are 4 times more expensive than FD schemes in $2D$, and 9 times more expensive in $3D$ [81].

2. PRELIMINARIES

2.1. Domains, meshes, and mappings

The focus of this work is mesh adaptation on $2D$ rectangles, though all of our meshing algorithms can be easily extended to $3D$ cuboids. Let $\Omega_{\text{ref}} \subset \mathbb{R}^2$ be a *reference* domain with coordinates $x = (x^1, x^2) \in \Omega_{\text{ref}}$, and given explicitly by the rectangle $\Omega_{\text{ref}} = (x_{\text{min}}^1, x_{\text{max}}^1) \times (x_{\text{min}}^2, x_{\text{max}}^2)$. The boundary $\partial\Omega_{\text{ref}}$ consists of the four sides of the rectangle $\partial\Omega_{\text{ref}} = \Gamma_l \cup \Gamma_r \cup \Gamma_d \cup \Gamma_u$, where e.g. $\Gamma_l = \{x_{\text{min}}^1\} \times [x_{\text{min}}^2, x_{\text{max}}^2]$, and similarly for the other sides. The outward pointing unit normal vector to $\partial\Omega_{\text{ref}}$ is defined everywhere on $\partial\Omega_{\text{ref}}$, except at the four corners, and is denoted by ν . The domain Ω_{ref} is also sometimes referred to in the literature as the *logical* or *computational* domain, and in the context of ALE gas dynamics, the *ALE* domain.

We denote by $\Omega \subset \mathbb{R}^2$ the *physical* or *Eulerian* domain, with coordinates $y = (y^1, y^2) \in \Omega$ and boundary $\partial\Omega$. We assume that Ω_{ref} and Ω represent the same mathematical domain i.e. $\Omega_{\text{ref}} = \Omega$. The purpose of using the different notations Ω_{ref} and Ω is to clearly distinguish between functions defined on each of these domains, as we shall explain in the next subsection.

We discretize Ω_{ref} and Ω with $m + 1$ nodes in the horizontal direction, and $n + 1$ nodes in the vertical direction. and denote by \mathcal{T}_{ref} and \mathcal{T} the grids (or meshes) on each of these domains. Each of these meshes contains $N = m \times n$ cells. The domain Ω_{ref} is discretized uniformly, and we refer to \mathcal{T}_{ref} as the *reference* or *uniform* mesh. The *physical* or *adaptive* mesh \mathcal{T} is *a priori* unknown and will be generated through a meshing scheme. The mesh \mathcal{T} is not assumed to be uniform, but contains the same number of cells and retains the same mesh connectivity structure as the uniform mesh \mathcal{T}_{ref} c.f. Figure 1. The fixed uniform mesh spacing is denoted by $\Delta x = (\Delta x^1, \Delta x^2)$, while the (non-uniform) local mesh spacing on \mathcal{T} is denoted by $\Delta y = (\Delta y^1, \Delta y^2)$.

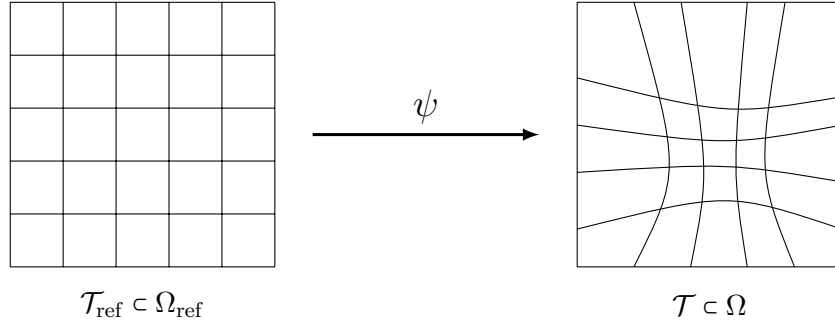


Figure 1: The uniform $m \times n$ mesh \mathcal{T}_{ref} and the adaptive $m \times n$ mesh $\mathcal{T} = \psi(\mathcal{T}_{\text{ref}})$.

The physical domain Ω can also be discretized uniformly with a uniform mesh \mathcal{U} . Since $\Omega_{\text{ref}} = \Omega$, the meshes \mathcal{U} and \mathcal{T}_{ref} are identical. We stress, however, that functions defined on each of these meshes are very different.

The mesh \mathcal{T} will be the image of \mathcal{T}_{ref} under the action of a suitable map $\psi : \Omega_{\text{ref}} \rightarrow \Omega$. The map ψ is bijective, continuously differentiable, and with continuously differentiable inverse $\psi^{-1} : \Omega \rightarrow \Omega_{\text{ref}}$ i.e. ψ is a smooth diffeomorphism. Our SAM scheme solves for the map ψ by prescribing its Jacobian determinant, as we shall explain in Sections 3 and 4. Nodes in \mathcal{T} on the boundary $\partial\Omega$ will be allowed to move tangential to the boundary, with the exception of the four nodes at the corners of Ω , which must remain fixed.

In the dynamic setting, we consider ψ to be a time-dependent map $\psi : \Omega_{\text{ref}} \times [0, T] \rightarrow \Omega$ where, for each $t \in [0, T]$, the map $\psi(\cdot, t) : \Omega_{\text{ref}} \rightarrow \Omega$ is a smooth diffeomorphism with prescribed Jacobian c.f. Figure 8.

2.2. Eulerian and ALE variables

A *physical* or *Eulerian* function (scalar, vector-valued, or tensor) is defined on Ω and denoted with the upright mathematical font $\mathbf{f} : \Omega \rightarrow \mathbb{R}^k$. For a time-dependent function $\mathbf{f} : \Omega \times [0, T] \rightarrow \mathbb{R}^k$ we shall write $\mathbf{f}(y, t)$.

Since ψ maps Ω_{ref} to Ω , we write $y = \psi(x, t)$ for $(x, t) \in \Omega_{\text{ref}} \times [0, T]$. Given an Eulerian variable $\mathbf{f} : \Omega \rightarrow \mathbb{R}^k$, we define its *computational* or *ALE* counterpart $f : \Omega_{\text{ref}} \times [0, T] \rightarrow \mathbb{R}^k$ by

$$f(x, t) := [\mathbf{f} \circ \psi](x, t) \equiv \mathbf{f}(\psi(x, t), t), \quad \forall (x, t) \in \Omega_{\text{ref}} \times [0, T]. \quad (2)$$

We shall also denote the function composition in (2) by $\mathbf{f} \circ \psi(x, t)$. When there is no confusion, we omit the function arguments and write \mathbf{f} or f .

In the discrete setting, computational variables are defined at the nodal points of the uniform reference mesh \mathcal{T}_{ref} . Physical/Eulerian variables, on the other hand, can be defined on either the adaptive mesh $\mathcal{T}(t)$ or the uniform mesh \mathcal{U} on Ω .

2.3. Derivatives and important geometric quantities

We denote spatial derivatives on Ω_{ref} by

$$\partial_i \equiv \frac{\partial}{\partial x_i},$$

and derivatives on Ω by

$$D_i \equiv \frac{\partial}{\partial y_i}.$$

Higher order derivatives are then denoted in the standard fashion e.g. $\partial_{ij} = \partial_i \partial_j$ and $D_{ij} = D_i D_j$. We use the notation $\nabla \equiv (\partial_1, \partial_2)^T$ and $D \equiv (D_1, D_2)^T$ for the gradient operators with respect to x and y coordinates, respectively. The Laplacian operators are denoted by the symbols $\Delta = (\partial_1^2 + \partial_2^2)$ and $D^2 = (D_1^2 + D_2^2)$. The operator Δ should not be confused with the discrete mesh spacing, denoted by Δx^i or Δy^i .

The time derivative of a function f is written as $\partial_t f$, or sometimes with the subscript notation f_t . Throughout, we shall use Einstein's summation convention wherein a repeated index in the same term indicates summation over all values of that index. We shall also use the standard Kronecker delta symbol δ_j^i and Levi-Civita symbol ϵ_j^i .

Given an Eulerian variable $\mathbf{f}(y, t)$ and its ALE counterpart $f(x, t)$, we can relate their spatial and temporal derivatives by applying the chain rule to (2). For simplicity, assume that \mathbf{f} is a scalar function. Then we compute

$$\partial_i f(x, t) = \partial_i \psi^j(x, t) D_j \mathbf{f}(y, t),$$

or, in matrix notation,

$$\nabla f(x, t) = \begin{pmatrix} \partial_1 \psi^1 & \partial_1 \psi^2 \\ \partial_2 \psi^1 & \partial_2 \psi^2 \end{pmatrix} \begin{pmatrix} D_1 \mathbf{f} \\ D_2 \mathbf{f} \end{pmatrix} = \nabla \psi^T D \mathbf{f}(y, t).$$

Inverting the above yields

$$D \mathbf{f}(y, t) = \nabla \psi^{-T} \nabla f(x, t). \quad (3)$$

We now introduce the following important geometric quantities, all defined on $\Omega_{\text{ref}} \times [0, T]$:

$$\mathcal{A} = [\nabla \psi]^{-1} \quad (\text{inverse of the deformation tensor}), \quad (4a)$$

$$\mathcal{J} = \det \nabla \psi \quad (\text{Jacobian determinant}), \quad (4b)$$

$$a = \mathcal{J} \mathcal{A} \quad (\text{cofactor matrix of the deformation tensor}). \quad (4c)$$

We assume that there exists $\varepsilon > 0$ such that

$$\mathcal{J}(x, t) \geq \varepsilon > 0, \text{ for every } (x, t) \in \Omega_{\text{ref}} \times [0, T].$$

Thus, the Jacobian determinant in $2D$ reads

$$\mathcal{J}(x, t) = \partial_1 \psi^1 \partial_2 \psi^2 - \partial_1 \psi^2 \partial_2 \psi^1.$$

For a matrix $M = (M_i^j)$, the subscript i indexes the columns of M , while the superscript j indexes the rows.

By explicit computation, we can verify the so-called Piola identity, which states that the columns of the cofactor matrix are divergence-free:

$$\partial_j a_i^j = 0, \text{ for } i = 1, 2. \quad (5)$$

In coordinate notation, we can thus write (3) as

$$D_i \mathbf{f}(y, t) = \frac{1}{\mathcal{J}(x, t)} a_i^j(x, t) \partial_j f(x, t) = \frac{1}{\mathcal{J}} \partial_j (a_i^j f), \quad (6)$$

where we have used the Piola identity (5) in the second equality.

By the chain rule again, we can compute

$$\partial_t f(x, t) = \partial_t \mathbf{f}(y, t) + \psi_t^i(x, t) D_i \mathbf{f}(y, t),$$

where $\psi_t(x, t) \equiv \partial_t \psi(x, t)$ is the *mesh velocity*. Using (6), we see that

$$\partial_t \mathbf{f}(y, t) = \partial_t f - \frac{\psi_t^i}{\mathcal{J}} a_i^j \partial_j f. \quad (7)$$

2.4. Computational platform and code optimization

All of the algorithms in this work were coded in Fortran90, and all of the numerical simulations performed were run on a Macbook Pro laptop with a 2.4 GHz Intel Core i5 processor and 8 GB of RAM. The operating system is macOS High Sierra 10.13.6, and the gfortran compiler is used. The codes for the numerical methods described in the paper are implemented in the same programming framework, but are not otherwise specially optimized, apart from specific calculations described in the paper. The same input, output, and timing routines are used in all of the codes. This consistency allows for a reliable comparison of the different algorithms and their associated imposed computational burdens.

3. FAST STATIC ADAPTIVE MESHING

3.1. Mathematical formulation of static mesh generation

We construct an adaptive mesh \mathcal{T} as the image of the uniform mesh \mathcal{T}_{ref} under the action of a suitable smooth diffeomorphism $\psi : \Omega_{\text{ref}} \rightarrow \Omega$ c.f. Figure 1. Our objective is to compute the map ψ by prescribing its Jacobian determinant $\mathcal{J}(x) = \det \nabla \psi(x)$. Specifically, given a strictly positive *target Jacobian function* $\mathbf{G} : \Omega \rightarrow \mathbb{R}^+$, the map ψ is found as the solution to the following nonlinear nonlocal Monge-Ampère (MA) equation

$$\begin{cases} \det \nabla \psi(x) = \mathbf{G} \circ \psi(x), & x \in \Omega_{\text{ref}} \\ \psi(x) \cdot \nu = x \cdot \nu, & x \in \partial \Omega_{\text{ref}} \end{cases} \quad (8a)$$

$$\quad (8b)$$

with ν the unit outward normal to the boundary $\partial\Omega_{\text{ref}}$.

The function \mathbf{G} is a user prescribed or constructed function that compresses the mesh in regions where \mathbf{G} is small, and expands the mesh in regions where \mathbf{G} is large. Note that \mathbf{G} is a physical target Jacobian function defined on the physical domain Ω . Assuming that a map ψ satisfying (8) is found, the function \mathbf{G} then describes the size of the cells in \mathcal{T} . Let \mathcal{V} denote a cell in \mathcal{T} , and $\mathcal{V}_{\text{ref}} = \psi^{-1}(\mathcal{V})$ the uniform cell in \mathcal{T}_{ref} mapped to \mathcal{V} by ψ . If \mathbf{G} is sufficiently smooth, a Taylor series argument shows that

$$|\mathcal{V}| := \int_{\mathcal{V}} dy = \int_{\mathcal{V}_{\text{ref}}} \det \nabla \psi(x) dx = |\mathcal{V}_{\text{ref}}| \cdot \mathbf{G}(\psi(x_c)) + \mathcal{O}(|\Delta x|^2),$$

where x_c denotes the cell center of \mathcal{V}_{ref} . Thus, the value of \mathbf{G} in \mathcal{V} is a scaling factor that scales the uniform cell volume $|\mathcal{V}_{\text{ref}}| = \Delta x^1 \Delta x^2$ to the volume $|\mathcal{V}|$, up to some spatially fixed constant of order $\mathcal{O}(|\Delta x|)$.

For a solution to exist for (8), the function \mathbf{G} is required to satisfy the *solvability condition*

$$\int_{\Omega} \frac{1}{\mathbf{G}(y)} dy = \int_{\Omega_{\text{ref}}} \frac{\det \nabla \psi(x)}{\mathbf{G} \circ \psi(x)} dx = |\Omega_{\text{ref}}| = |\Omega|. \quad (9)$$

If the solvability condition (9) is satisfied, then the system (8) admits an infinitude of solutions. The question then becomes how to construct a solution ψ that is in some sense optimal. Our primary concern in this work is the development of a fast-running algorithm that can be easily implemented within an ALE framework for hydrodynamics simulations. We next describe a simple and efficient procedure for constructing a solution to (8).

3.2. The basic mesh generation procedure via the deformation method

The key to our fast-running algorithm is the reduction of the nonlinear equation (8) to a simple linear Poisson solve and ODE integration. Our approach is motivated, as in the works [52, 56, 32], by the deformation method of DACOROGNA AND MOSER [21].

3.2.1. Solution construction procedure. Specifically, a solution to (8) is obtained by the five step construction provided in Algorithm 1. We refer to this algorithm as SAM or, in the context of time-dependent meshing, *static SAM*.

3.2.2. Validity of construction. The proof that the map ψ constructed according to Algorithm 1 satisfies (8) proceeds as follows: define the quantity

$$\mathcal{R}(x, \tau) := J(x, \tau) [\tau \mathbf{F} \circ \eta(x, \tau) + (1 - \tau)],$$

where $J(x, \tau) := \det \nabla \eta(x, \tau)$. We shall show that $\partial_{\tau} \mathcal{R} = 0$. First, we have that

$$\partial_{\tau} (\mathbf{F} \circ \eta) = \partial_{\tau} \eta \cdot D\mathbf{F} \circ \eta = (\mathbf{v} \cdot D\mathbf{F}) \circ \eta,$$

where we have used the flowmap equation (13a). Next, the quantity $J(x, \tau)$ evolves according to

$$\partial_{\tau} J = J \operatorname{div} \mathbf{v} \circ \eta.$$

Using (14), (11a), and (12), we calculate

$$\operatorname{div} \mathbf{v} = \frac{\operatorname{div} \bar{\mathbf{v}}}{\tau \mathbf{F} + (1 - \tau)} - \frac{\tau \bar{\mathbf{v}} \cdot D\mathbf{F}}{[\tau \mathbf{F} + (1 - \tau)]^2} = \frac{1 - \mathbf{F} - \tau \mathbf{v} \cdot D\mathbf{F}}{\tau \mathbf{F} + (1 - \tau)} \quad (15)$$

Algorithm 1 : STATIC SAM

Step 1 : Assume that the physical target Jacobian function $\mathbf{G} : \Omega \rightarrow \mathbb{R}^+$ is given and satisfies the solvability condition

$$\int_{\Omega} \frac{1}{\mathbf{G}(y)} dy = |\Omega|, \quad (10)$$

and let $\mathbf{F}(y) = 1/\mathbf{G}(y)$. In practice, we are usually given an auxiliary target Jacobian function $\bar{\mathbf{G}} : \Omega \rightarrow \mathbb{R}^+$ that *does not* satisfy (10), and we define \mathbf{G} and \mathbf{F} by the following normalization procedure:

$$\bar{\mathbf{F}}(y) = \frac{1}{\bar{\mathbf{G}}(y)} \quad \longrightarrow \quad \mathbf{F}(y) = |\Omega| \frac{\bar{\mathbf{F}}(y)}{\int_{\Omega} \bar{\mathbf{F}}(y) dy} \quad \longrightarrow \quad \mathbf{G}(y) = \frac{1}{\mathbf{F}(y)}.$$

Step 2 : Solve the following linear Poisson equation with homogeneous Neumann boundary conditions for the *potential* $\Phi : \Omega \rightarrow \mathbb{R}$

$$\begin{cases} D^2\Phi(y) = 1 - \mathbf{F}(y), & y \in \Omega \\ D\Phi(y) \cdot \nu = 0, & y \in \partial\Omega \end{cases} \quad (11a)$$

$$(11b)$$

Step 3 : Define the velocity $\bar{\mathbf{v}} : \bar{\Omega} \rightarrow \mathbb{R}^2$ as

$$\bar{\mathbf{v}}(y) = D\Phi(y). \quad (12)$$

Step 4 : Solve the following ODE system for the *flowmap* $\eta : \bar{\Omega}_{\text{ref}} \times [0, 1] \rightarrow \bar{\Omega}$

$$\begin{cases} \partial_{\tau}\eta(x, \tau) = \mathbf{v} \circ \eta(x, \tau), & x \in \bar{\Omega}_{\text{ref}} \text{ and } 0 < \tau \leq 1 \\ \eta(x, 0) = x, & x \in \bar{\Omega}_{\text{ref}} \text{ and } \tau = 0 \end{cases} \quad (13a)$$

$$(13b)$$

where the *flowmap velocity* $\mathbf{v} : \bar{\Omega} \times [0, 1] \rightarrow \mathbb{R}^2$ is defined as

$$\mathbf{v}(y) = \frac{\bar{\mathbf{v}}(y)}{\tau\mathbf{F}(y) + (1 - \tau)}. \quad (14)$$

Step 5 : Define $\psi(x) := \eta(x, 1)$. Then ψ solves (8).

Now, we can compute

$$\begin{aligned} \partial_{\tau}\mathcal{R} &= \partial_{\tau}J[\tau\mathbf{F} \circ \eta(x, \tau) + (1 - \tau)] + J[\mathbf{F} \circ \eta - 1] + J\tau\partial_{\tau}(\mathbf{F} \circ \eta) \\ &= J\{\text{div } \mathbf{v}[\tau\mathbf{F} + (1 - \tau)] + \mathbf{F} - 1 + \tau\mathbf{v} \cdot D\mathbf{F}\} \circ \eta. \end{aligned}$$

Then (15) shows that $\partial_{\tau}\mathcal{R} \equiv 0$. Thus, $1 = \mathcal{R}(x, 0) = \mathcal{R}(x, 1) = \det \nabla\psi(x)\mathbf{F}(\psi(x))$, and since $\mathbf{G} = 1/\mathbf{F}$ we conclude that ψ satisfies (8a). Since $\mathbf{v}(y, \tau) \cdot \nu = 0$ for every $y \in \partial\Omega$ and $0 \leq \tau \leq 1$, then $\partial_{\tau}\eta(x, \tau) \cdot \nu = 0$ for $x \in \partial\Omega_{\text{ref}}$. Then $\eta(x, 0) \cdot \nu = x \cdot \nu \implies \eta(x, 1) \cdot \nu = \psi(x) \cdot \nu = 0$ for $x \in \partial\Omega_{\text{ref}}$ and (8b) is satisfied. \square

3.2.3. Discussion. The idea of using the deformation method as a means of constructing a map with prescribed Jacobian determinant was first used by DACOROGNA AND MOSER [21], and a first numerical implementation can be found in the paper of LIAO AND ANDERSON [52]. These works,

however, utilized the no slip boundary conditions $\psi(x) = x$, $\forall x \in \partial\Omega_{\text{ref}}$, rather than the no penetration boundary conditions (8b) which permit tangential motion of boundary nodes. The method of proof in [21], which includes an analysis of the Poisson problem (11), requires the domain Ω_{ref} to have smooth boundary $\partial\Omega_{\text{ref}}$ and so is not valid for the rectangular domains we consider in this work. A modified method, which avoids the use of the Poisson problem (11) via a direct construction of the vector field \bar{v} , is provided in [52], but the resulting numerical implementation yields poor quality grids with high levels of distortion [22]. On the other hand, as we shall demonstrate in our numerical experiments, the use of the Poisson equation (11) together with the slip boundary conditions (8b) produces smooth grids. Moreover, the arguments in [21] can be modified with the help of elliptic estimates on polygonal domains [34] to show that the procedure outlined in Algorithm 1 yields existence of a solution to (8).

The basic mesh generation scheme Algorithm 1 is similar to other algorithms in the literature e.g. [56, 32], but our numerical implementation differs from those works. In particular, we shall use the simple error analysis and convergence tests in Section 3.5 to justify our numerical implementation choices with regards to stability, accuracy, and efficiency considerations. In the following subsections, we describe in detail the two main steps of Algorithm 1, namely the Poisson solve in Step 2, and the flowmap integration in Step 4.

3.3. Numerical solution of the Poisson problem

In the following, we provide details of our numerical solution procedure for the Poisson problem (11) for the potential Φ . We assume that the target Jacobian function \mathbf{G} is smooth in $\bar{\Omega}$. We emphasize that the target Jacobian function \mathbf{G} is always provided on the uniform mesh $\mathcal{U} \subset \Omega$. Consequently, the potential Φ and its gradient $\bar{v} = D\Phi$ are also computed on \mathcal{U} . The use of a uniform mesh in SAM is essential for two reasons: first, it allows us to utilize a highly efficient and accurate spectral solver; and second, it greatly simplifies and improves the efficiency of the interpolation procedure used in the flowmap integration scheme (to be described in the next section).

3.3.1. FFT-based elliptic solve for Φ . The Poisson problem (11) is solved in frequency space using the Fast Fourier Transform (FFT). The solvability condition (10) is enforced by the normalization procedure described in Algorithm 1 with trapezoidal integration to compute integrals. The RHS of (11a) then has zero mean, and a (non-unique) solution to (11) exists. We choose a unique solution Φ with zero mean, enforced in spectral space by zeroing out the first frequency component. The use of FFT requires the forcing \mathbf{G} to be periodic; we periodize the problem by doubling the size of the domain in each direction and extending \mathbf{G} symmetrically to the extended domain⁶. In Step 3, the velocity \bar{v} is also computed via FFT.

3.3.2. Boundary conditions and order of convergence. Solutions to the Poisson problem (11) in general have limited regularity due to the presence of corner singularities in the domain, unless the function \mathbf{G} satisfies certain compatibility conditions [38]. In this work, we shall assume the stronger Neumann condition $D\mathbf{G}(y) \cdot \nu = 0$ for $y \in \partial\Omega$ to ensure high-order convergence of the numerical solution ψ in the limit of zero mesh size. If $D\mathbf{G}(y) \cdot \nu \neq 0$, then the symmetric extension of \mathbf{G} is not differentiable on the boundary $\partial\Omega$ and is only Lipschitz continuous. In this case, the potential Φ , velocity \bar{v} , and solution ψ all converge with 2nd order accuracy, but the convergence rate of the Jacobian determinant $\mathcal{J}(x)$ and cofactor matrix $a(x)$ is only 1.5. The reason for the worse convergence of these quantities is that the mixed partial derivative $D_{12}\bar{v}$ is required for the

⁶An alternative implementation with the discrete cosine transform can also be used.

high order interpolation procedure utilized in Step 4 of Algorithm 1 (to be described in detail in the following section). The structure of the Poisson problem ensures $D_{12}\bar{v}$ converges with 2nd order accuracy, and therefore so does ψ . However, 3rd order and higher derivatives of \bar{v} in general do not converge with 2nd order accuracy, and consequently neither do derivatives of ψ .

On the other hand, if the function G does satisfy the Neumann condition $DG(y) \cdot \nu = 0$ for $y \in \partial\Omega$, then the symmetric extension of G is at least twice continuously differentiable, and the quantities $\psi(x)$, $\mathcal{J}(x)$, and $a(x)$ all converge with (at least) 4th order accuracy. We confirm this high order convergence with a numerical example in Section 3.5.3.

For most of the problems we consider in this work, the function G does indeed satisfy the Neumann condition. However, even if the Neumann condition is not satisfied, the errors in the numerical solution are localized to the boundary, and the meshes produced are still of high accuracy and quality. Additionally, boundary smoothing techniques [2, 29] can be applied to obtain high order convergence. We implement a simplified version of this technique in Section 3.7 and demonstrate that the quantity $\mathcal{J}(x)$ converges with 2nd order accuracy. The details of this boundary smoothing technique are provided in Appendix B.

3.4. Numerical solution of the flowmap equation

Next, we turn to the integration of the flowmap equation (13) in Step 4 of Algorithm 1. This (Lagrangian) flowmap equation has been well-studied in the turbulence community, where it used to track fluid particles and extract turbulence statistics from a given numerically computed Eulerian velocity field [85, 48]. As in these works, we discretize in the pseudo-time variable τ with a fixed pseudo-time step $\Delta\tau$, and use an explicit integration scheme.

The RHS of (13a) consists of the composition $\mathbf{v} \circ \eta(x, \tau)$; since the flowmap velocity \mathbf{v} is only known on the uniform mesh \mathcal{U} , the composition is approximated by interpolation. The choice of time integration scheme is directly related to the particular interpolation procedure used. High-order interpolation is essential [85], since low-order (e.g. linear interpolation) schemes do not smoothly capture small scale variations of \mathbf{v} . We therefore use a simple 4th order piecewise bicubic interpolation scheme, which provides a good mix of efficiency, accuracy, and smoothness. Then, we use the explicit fourth order Runge-Kutta (RK4) method to integrate in time. As we shall explain in the next section, RK4 is the natural pairing for bicubic interpolation with regards to accuracy, stability, and algorithmic efficiency.

3.4.1. Stability condition. Note that an explicit time discretization of (13) has an associated stability (CFL) condition constraining the maximum pseudo-time step $\Delta\tau$ allowed for a given resolution N . This condition reads

$$\text{CFL}_\tau = \Delta\tau \left(\frac{\|\mathbf{v}^1\|_\infty}{\Delta x^1} + \frac{\|\mathbf{v}^2\|_\infty}{\Delta x^2} \right) \leq C, \quad (16)$$

where C is a constant that depends on the spatial and temporal scheme used to solve (13). Here, we have used the notation CFL_τ in anticipation of preventing confusion when we utilize our mesh generation scheme for gas dynamics simulations, since associated with the latter is a stability condition on the *physical* time step Δt .

Assuming, $m = n = \sqrt{N}$, the stability condition (16) requires that $\Delta\tau$ decays (at least) like $\Delta\tau = \mathcal{O}(1/\sqrt{N})$, regardless of the particular time integration scheme used. In fact, for lower order methods, more stringent conditions on $\Delta\tau$ are required [23]. The stability region for RK4 is larger than for lower order (e.g. RK2, Adams-Bashforth) methods and includes the imaginary axis corresponding to pure advection [23]. In our numerical simulations with RK4, we have found

that $\text{CFL}_\tau \leq 2$ is sufficient. In practice, the pseudo-time step constraint imposed by accuracy requirements is usually more stringent than the stability condition (16) c.f. Remark 1.

3.5. Error analysis

The purpose of this section is to provide basic error analysis and convergence tests to justify our numerical implementation choices from the standpoint of stability, accuracy, and efficiency.

3.5.1. Jacobian error metric. Assessing the accuracy and convergence behavior of the numerical solutions ψ produced with SAM requires an error metric. Since the exact solution ψ_{exact} to the scheme described in Algorithm 1 is not known, we shall instead use the L^2 Jacobian error, defined as

$$\mathcal{E}_2 := \|\mathcal{J}(x) - \mathbf{G} \circ \psi(x)\|_{L^2}. \quad (17)$$

When it is known, the exact formula for \mathbf{G} is used to compute the composition $\mathbf{G} \circ \psi$ in (17); otherwise, we use bicubic interpolation. The L^2 integral norm is approximated with trapezoidal integration. In formula (17), the Jacobian determinant \mathcal{J} is computed with a differencing scheme. To demonstrate the high order convergence of solutions, we shall use the 4th order central difference scheme (CD4) in this section; this is also the scheme required when SAM is coupled to our ALE hydrodynamics scheme c.f. Section 6.

We shall also compare SAM with the MK mesh generation scheme of [22], which we provide a brief description of in Appendix C. The MK scheme is 2nd order accurate, and we instead use a slightly modified error metric

$$\mathcal{E}_2 = \sqrt{\Delta x^1 \Delta x^2 \sum_{i=1}^{m-1} \sum_{j=1}^{n-1} |\mathcal{J}_{ij}^{\text{mid}} - \mathbf{G}(\psi_{ij}^{\text{mid}})|^2}, \quad (18)$$

where ψ_{ij}^{mid} denotes the position of the cell centers of the adaptive mesh, computed as the average position of the four surrounding nodes. The quantity \mathcal{J}^{mid} is computed at the cell centers using a 2nd order difference scheme as

$$\mathcal{J}_{ij}^{\text{mid}} = \frac{\delta \psi_{ij}^1}{\delta x^1} \frac{\delta \psi_{ij}^2}{\delta x^2} - \frac{\delta \psi_{ij}^2}{\delta x^1} \frac{\delta \psi_{ij}^1}{\delta x^2},$$

with

$$\begin{aligned} \frac{\delta \psi_{ij}^1}{\delta x^1} &= \frac{\psi_{i+1,j}^1 - \psi_{i,j}^1 + \psi_{i+1,j+1}^1 - \psi_{i,j+1}^1}{2\Delta x^1}, \\ \frac{\delta \psi_{ij}^1}{\delta x^2} &= \frac{\psi_{i,j+1}^1 - \psi_{i,j}^1 + \psi_{i+1,j+1}^1 - \psi_{i+1,j}^1}{2\Delta x^2}, \\ \frac{\delta \psi_{ij}^2}{\delta x^1} &= \frac{\psi_{i+1,j}^2 - \psi_{i,j}^2 + \psi_{i+1,j+1}^2 - \psi_{i,j+1}^2}{2\Delta x^1}, \\ \frac{\delta \psi_{ij}^2}{\delta x^2} &= \frac{\psi_{i,j+1}^2 - \psi_{i,j}^2 + \psi_{i+1,j+1}^2 - \psi_{i+1,j}^2}{2\Delta x^2}. \end{aligned}$$

For simplicity, we shall assume in the following that we are on a square mesh with $m = n = \frac{1}{\Delta x^1} = \frac{1}{\Delta x^2} = \sqrt{N}$.

3.5.2. Flowmap integration and interpolation errors. Next, we analyze the sources of error in SAM, of which there are three: (1) the FFT solve for Φ , (2) the RK4 time discretization, and (3) the bicubic interpolation routine. Each of these schemes is high-order accurate, provided the function \mathbf{G} is smooth enough. In particular, if \mathbf{G} is periodic, the FFT solve computes the potential Φ with spectral accuracy, and the associated error is dominated by the interpolation and time integration errors as the mesh is refined. We therefore focus on the latter two errors, and in the following assume that the velocity $\bar{\mathbf{v}}(y)$ is exact.

A semi-discretization of the flowmap equation (13) results in the coupled ODE system

$$\begin{cases} \frac{d}{d\tau}\eta_{ij}(\tau) = \mathbf{v}(\eta_{ij}(\tau), \tau), & 0 < \tau \leq 1 \\ \eta_{ij}(0) = x_{ij}, & \tau = 0, \end{cases} \quad (19a)$$

$$\begin{cases} \frac{d}{d\tau}\tilde{\eta}_{ij}(\tau) = \tilde{\mathbf{v}}_{ij}(\tau), & 0 < \tau \leq 1 \\ \tilde{\eta}_{ij}(0) = x_{ij}, & \tau = 0, \end{cases} \quad (19b)$$

for $1 \leq i \leq m+1$ and $1 \leq j \leq n+1$. The right-hand side of (19a) requires \mathbf{v} at the points $\eta_{ij}(\tau)$, which is not known and must be approximated using interpolation. We therefore instead solve for the collection of points $\tilde{\eta}_{ij}$ satisfying

$$\begin{cases} \frac{d}{d\tau}\tilde{\eta}_{ij}(\tau) = \tilde{\mathbf{v}}_{ij}(\tau), & 0 < \tau \leq 1 \\ \tilde{\eta}_{ij}(0) = x_{ij}, & \tau = 0 \end{cases} \quad (20a)$$

$$\begin{cases} \frac{d}{d\tau}\tilde{\eta}_{ij}(\tau) = \tilde{\mathbf{v}}_{ij}(\tau), & 0 < \tau \leq 1 \\ \tilde{\eta}_{ij}(0) = x_{ij}, & \tau = 0 \end{cases} \quad (20b)$$

where $\tilde{\mathbf{v}}_{ij}(\tau) = \mathbf{v}(\tilde{\eta}_{ij}(\tau), \tau) + \mathbf{e}_v$ is the interpolated velocity field approximation to $\mathbf{v}(\tilde{\eta}_{ij}(\tau), \tau)$ at each $\tau \in [0, 1]$, and $\mathbf{e}_v = \mathbf{e}_v(\tilde{\eta}_{ij}(\tau), \tau)$ is the associated interpolation error. Let $\|\cdot\|_\infty := \sup_{ij}$. Note that $\|\mathbf{e}_v\|_\infty$ is independent of the query points $\tilde{\eta}_{ij}$, and depends only on (derivatives of) \mathbf{v} , and τ . In fact, since

$$\begin{aligned} \sup_\tau \|\mathbf{v}(\tau)\|_\infty &\leq \|\bar{\mathbf{v}}\|_\infty \cdot \sup_\tau \|(\tau\mathbf{F} + (1-\tau))^{-1}\|_\infty \\ &\leq C\|\bar{\mathbf{v}}\|_\infty, \end{aligned}$$

the error $\mathbf{E}_v := \sup_\tau \|\mathbf{e}_v\|_\infty$ is bounded. Integration of (20a) results in an error $\mathcal{O}(\mathbf{E}_v)$ between solutions to (19) and (20), regardless of the integrator and pseudo-time step $\Delta\tau$ used.

To see why, let $\mathbf{e}_\eta(\tau) := \tilde{\eta}_{ij}(\tau) - \eta_{ij}(\tau)$ be the error when both (19) and (20) are solved exactly. By the fundamental theorem of calculus,

$$\begin{aligned} \|\mathbf{e}_\eta(\tau)\|_\infty &\leq \int_0^\tau \|\tilde{\mathbf{v}}(\tilde{\eta}_{ij}(s), s) - \mathbf{v}(\eta_{ij}(s), s)\|_\infty ds \\ &\leq \int_0^\tau \|\tilde{\mathbf{v}}(\tilde{\eta}_{ij}(s), s) - \mathbf{v}(\tilde{\eta}_{ij}(s), s)\|_\infty ds + \int_0^\tau \|\mathbf{v}(\tilde{\eta}_{ij}(s), s) - \mathbf{v}(\eta_{ij}(s), s)\|_\infty ds \\ &\leq \tau \mathbf{E}_v + \int_0^\tau \|\mathbf{v}(\tilde{\eta}_{ij}(s), s) - \mathbf{v}(\eta_{ij}(s), s)\|_\infty ds \end{aligned}$$

Assuming that the velocity \mathbf{v} is Lipschitz with Lipschitz constant L_{lip} , we have that

$$\begin{aligned} \|\mathbf{e}_\eta(\tau)\|_\infty &\leq \tau \mathbf{E}_v + L_{\text{lip}} \int_0^\tau \|\mathbf{e}_\eta(s)\|_\infty ds \\ &\leq \tau \mathbf{E}_v e^{L_{\text{lip}}\tau}, \end{aligned} \quad (21)$$

by application of Gronwall's inequality, and thus the error at the final time is $\|\mathbf{e}_\eta(1)\|_\infty = \mathcal{O}(\mathbf{E}_v)$.

It is therefore inefficient to use too small a value of $\Delta\tau$ in a time discretization of (20), since the resulting solutions converge to the exact solution of (20) rather than (19). On the other hand, using a low-accuracy integrator with high-order interpolation is a waste of the computational resources

expended in computing an accurate interpolant \tilde{v} . Let $\mathbf{E}_\eta = \|\tilde{\eta}_{ij}(1) - \eta_{ij}(1)\|_\infty$ be the error at $\tau = 1$ between the numerical solution of (20) and the exact solution of (19). We can then decompose

$$\mathbf{E}_\eta = \mathbf{E}_\tau + \mathcal{O}(\mathbf{E}_v),$$

where \mathbf{E}_τ is the global truncation error of the time integration scheme. We thus aim to choose a time-step $\Delta\tau = \Delta\tau^*$ such that $\mathbf{E}_\tau = \mathcal{O}(\mathbf{E}_v)$, and refer to $\Delta\tau^*$ as the *saturation point*. Choosing $\Delta\tau < \Delta\tau^*$ will not yield a smaller error \mathbf{E}_η . In fact, choosing $\Delta\tau = \Delta\tau^*$ can cause some cancellation between the integration and interpolation errors, which can produce a smaller error than would otherwise be obtained with $\Delta\tau < \Delta\tau^*$.

We investigate the convergence behavior under mesh refinement of the saturation point $\Delta\tau^*$ with the following numerical test: we generate a mesh on $\Omega = [0, 1]^2$ with forcing given by

$$G(y) = 1 - \delta \cos(4\pi y^1) \cos(4\pi y^2), \quad (22)$$

with $\delta = 0.75$. Since (22) is sinusoidal, the FFT solve for \bar{v} is essentially exact, and the errors in the numerical solution are therefore entirely due to interpolation and time integration. For a fixed number of cells N , we generate a sequence of meshes in which the flowmap equation (20) is numerically integrated with RK4 and with progressively smaller values of $\Delta\tau$, starting with $\Delta\tau = 1$ and ending with $\Delta\tau = 1/200$. We then repeat for increasing values of N , starting with $N = 32^2$ and ending with $N = 2048^2$. We compute the L^2 Jacobian error \mathcal{E}_2 using (17) with CD4.

The blue symbols in Figure 2(a) show the value of \mathcal{E}_2 as $\Delta\tau$ varies, for each resolution N . For each fixed N , the error decreases at a rate proportional to $\Delta\tau^{-4}$, as expected for RK4, until the saturation point $\Delta\tau^*$ is reached. The values of $\Delta\tau^*$ for each N are shown as the red stars in Figure 2(a). For each N , the value of $\Delta\tau^*$ is estimated in the following way. First, a piecewise cubic interpolant $c(\Delta\tau)$ was fitted to the data in log log space; these are shown in Figure 2(a) as the blue curves passing through the data points. Then, we find $\Delta\tau^*$ as the largest value of $\Delta\tau$ for which $|c(\Delta\tau) - \mathcal{E}_2^*| < \mathcal{E}_2^*/10$, where \mathcal{E}_2^* is the converged error computed with $\Delta\tau = 1/200$.

We see that, for this test, the saturation point $\Delta\tau^*$ is reached at the maximum possible value $\Delta\tau = 1$ for the lowest resolution $N = 32^2$. As N increases to 2048^2 , the value of $\Delta\tau^*$ decreases to approximately $\Delta\tau \approx 0.014$, and about 70 pseudo-time steps are required for the solution to converge. In practice, for the simulations considered in this paper we will generally be restricted (due to RAM constraints) to grids of size $N = 256^2$ at most, for which approximately 10 pseudo-time steps are sufficient to reach the saturation point.

Assuming sufficient smoothness of \mathbf{v} , the bicubic interpolation error is $\mathbf{E}_v = \mathcal{O}(|\Delta x|^4) = \mathcal{O}(N^{-2})$. Since RK4 has global error $\mathbf{E}_\tau = \mathcal{O}(\Delta\tau^4)$, we thus see that the saturation point $\Delta\tau^*$ scales like

$$\Delta\tau^* \sim \frac{1}{\sqrt{N}} \quad \text{as } N \rightarrow \infty. \quad (23)$$

This behavior is confirmed with the blue curve plotted in Figure 2(b). Then, if $\Delta\tau^*$ is chosen according to (23), the Jacobian error \mathcal{E}_2 converges with 4th order accuracy i.e. $\mathcal{E}_2 = \mathcal{O}(|\Delta x|^4) = \mathcal{O}(N^{-2})$.

REMARK 1. Note that the scaling (23) is consistent with the stability condition (16). The former is based purely on accuracy and efficiency considerations, while the latter is the natural stability condition associated with the transport equation (13). This consistency between accuracy, stability, and efficiency justifies our numerical implementation choices. We also note that, whereas the condition (16) depends upon $\|\mathbf{v}\|_{L^\infty}$, the scaling (23) depends upon the maximum value of 4th order derivatives of \mathbf{v} , since we are using bicubic interpolation. In practice, the meshes we generate have

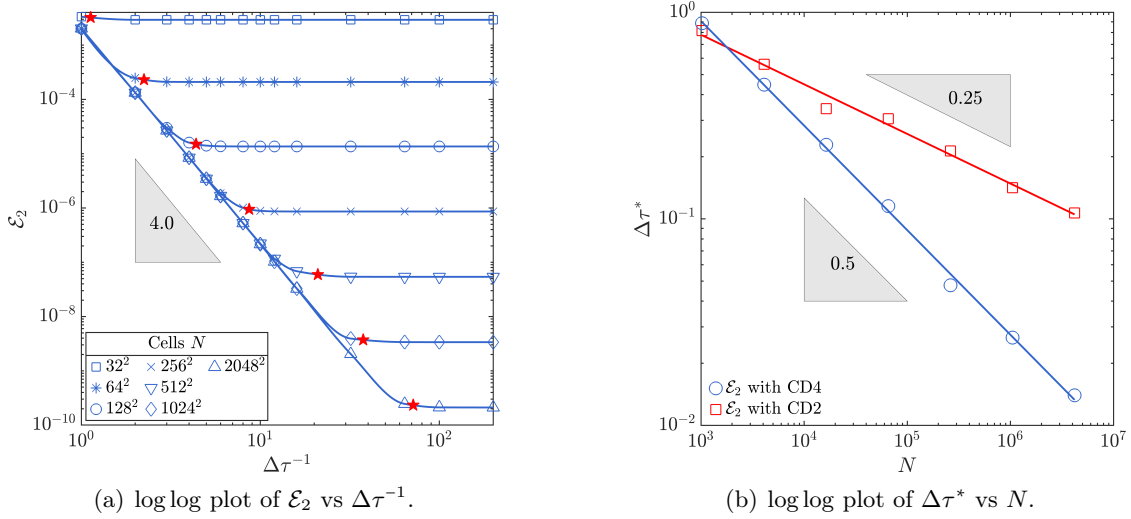


Figure 2: Spatio-temporal error analysis and convergence tests for the numerical solution of the flowmap equation. Figure 2(a) is a log log plot of the Jacobian error \mathcal{E}_2 vs (inverse of) pseudo-time step $\Delta\tau^{-1}$ at various resolutions for the target Jacobian (22). The red stars indicate the saturation point $\Delta\tau^*$. Figure 2(b) is a log log plot of the saturation point $\Delta\tau^*$ vs resolution N . The blue curve is for solutions that converge with 4th order accuracy with $\Delta\tau^*$ chosen according to (23). The red curve is for solutions that converge with 2nd order accuracy with $\Delta\tau^*$ chosen according to (24).

large deformations and it is therefore usually the case that (23) is the more stringent condition on $\Delta\tau$ than (16).

The saturation scaling in (23) is dependent upon the order of convergence desired and, in particular, the choice of differencing scheme used to compute the error metric \mathcal{E}_2 . The plot in Figure 2(a) and the corresponding blue curve in Figure 2(b) show the behavior of $\Delta\tau^*$ for \mathcal{E}_2 computed with CD4 for solutions that converge with 4th order accuracy. If 2nd order central differencing (CD2) is used in (17) instead, then the error metric does not capture the high order convergence of solutions, which therefore only converge with 2nd order accuracy i.e. $\mathcal{E}_2 = \mathcal{O}(N^{-1})$, and consequently a larger value of $\Delta\tau^*$ is then found as the saturation point. This is demonstrated in Figure 2(b) with the red curve, which shows that $\Delta\tau^* \sim \frac{1}{\sqrt[4]{N}}$ when \mathcal{E}_2 is computed with CD2. Therefore, the scaling of $\Delta\tau^*$ depends upon the order of accuracy desired, and that used to compute \mathcal{E}_2 . For our ALE simulations, we will be required to use CD4 with $\mathcal{E}_2 = \mathcal{O}(N^{-2})$, and we thus use (23). For stand-alone mesh generation experiments in which comparisons are made with other meshing schemes (which are only 2nd order accurate), we shall instead use

$$\Delta\tau^* \sim \frac{1}{\sqrt[4]{N}} \quad \text{as } N \rightarrow \infty. \quad (24)$$

If $\Delta\tau^*$ is chosen according to (24), the Jacobian error \mathcal{E}_2 converges with 2nd order accuracy i.e. $\mathcal{E}_2 = \mathcal{O}(N^{-1})$.

For high-resolution meshes with N large, experimenting with the choice of $\Delta\tau$ to find the saturation point $\Delta\tau^*$ is computationally expensive. Equations (23) and (24) provide a straightforward way to choose the optimal pseudo-time step: find the saturation point for a low-resolution mesh (which can be computed quickly), then use (23) or (24), depending on the desired order of accuracy of \mathcal{E}_2 .

3.5.3. High order convergence of solutions. To demonstrate the high order convergence of numerical solutions computed with SAM, we perform a mesh generation experiment on $\Omega = [0, 1]^2$ for the circular target Jacobian function

$$\bar{G}(y) = 1 - \delta \exp \left\{ - \left| \sigma \left((y^1 - 0.5)^2 + (y^2 - 0.5)^2 - r^2 \right) \right|^2 \right\}. \quad (25)$$

Then \bar{G} forces the mesh to resolve in an annular region containing the circle of radius r centered at $(0.5, 0.5)$. The parameters δ and σ control the smallest cell-size and width of the resolving region, respectively. We choose $\delta = 0.75$, $\sigma = 64$, and $r = 0.2$. The adaptive meshes \mathcal{T} produced using Algorithm 1 are shown in Figure 3 for 32^2 and 64^2 cell resolution.

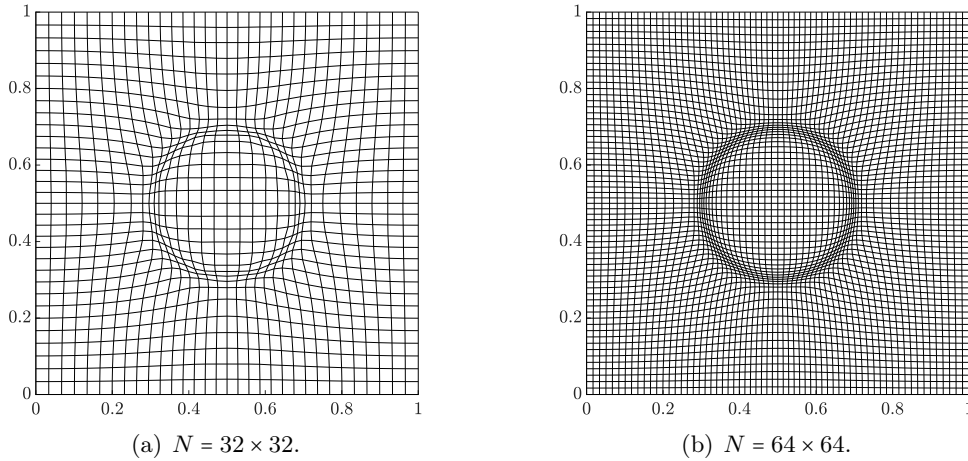


Figure 3: Adaptive meshes produced with SAM for the circular target Jacobian (25). The SAM solutions are smooth and converge with 4th order accuracy, as confirmed in Table 1.

We generate a sequence of meshes using SAM for cell resolutions $N = 32^2$ up to $N = 1024^2$. We use the scaling (23) for the pseudo-time step $\Delta\tau$ and list the Jacobian errors \mathcal{E}_2 computed using (17) with CD4 in Table 1. The data in Table 1 show that SAM solutions exhibit the expected 4th order accuracy. We note that, to the best of our knowledge, all other grid generation schemes are at best 2nd order accurate.

Scheme		Cells					
		32×32	64×64	128×128	256×256	512×512	1024×1024
SAM	Error	2.21×10^{-2}	3.12×10^{-3}	1.90×10^{-4}	1.34×10^{-5}	8.67×10^{-7}	5.49×10^{-8}
	Order	–	2.8	4.0	3.8	4.0	4.0

Table 1: Jacobian errors \mathcal{E}_2 demonstrating high order convergence of SAM solutions for the circular target Jacobian function (25).

3.6. Algorithmic complexity and CPU runtime

We next turn to the question of algorithmic performance of SAM. By far the most computationally expensive part of the algorithm is the integration of the flowmap equation (13), and, specifically, the interpolation call required at each RK4 stage to compute the composition $v \circ \eta(x, \tau)$. We therefore begin by describing a number of simple (but important) optimizations of a standard piecewise bicubic interpolation routine. These optimizations drastically improve the performance

of the routine. Again, the importance of working on the uniform mesh \mathcal{U} will become clear in the following.

3.6.1. Fast bicubic interpolation for (13). At each RK4 stage, the composition $v \circ \eta(x, \tau)$ on the RHS of (13) is computed by numerically interpolating the values v_{ij} given on the uniform mesh \mathcal{U} onto the deformed mesh given by the nodal values $\eta(x_{ij}, \tau)$.

We describe our interpolation procedure for a general function f , defined on the uniform mesh \mathcal{U} by the values f_{ij} . Suppose that we have a collection of points $\eta_{ij} = (\eta_{ij}^1, \eta_{ij}^2)$ arranged on a structured (but, in general, non-uniform) mesh \mathcal{T}_η . For each node η_{ij} , the basic interpolation procedure proceeds in the following two steps: first, perform a grid search of \mathcal{U} to find the specific uniform cell \mathcal{V}^* in which η_{ij} is located; then, approximate f in \mathcal{V}^* with a high-order bicubic interpolant \tilde{f} , and calculate $f(\eta_{ij}) \approx \tilde{f}(\eta_{ij})$. Our optimizations of this basic interpolation procedure are described in the following five subsections.

3.6.2. Fast binary grid searching. As we shall demonstrate, the grid search is the most computationally intensive part of the interpolation procedure and, indeed, the full static SAM algorithm. Suppose that the grid consists of $N = m \times n$ cells. A brute force approach, in which each cell of \mathcal{U} is checked until the cell containing η_{ij} is found, is $\mathcal{O}(N)$ in the worst case, for a single point η_{ij} . Since we require the interpolated value for every such $\eta_{ij} \in \mathcal{T}_\eta$, the algorithmic complexity of the full grid search using the brute force approach is $\mathcal{O}(N^2)$ in the worst case. Since each RK4 stage in a pseudo-time step⁷ requires one interpolation call, the total grid search time required to integrate the flowmap until $\tau = 1$ is $\mathcal{O}(4N^2/\Delta\tau)$. This is extremely computationally expensive for large N , and it is therefore essential that some optimization is performed to improve the efficiency of the grid search.

Fortunately, a simple such optimization is possible, since the discrete values f_{ij} are provided on the uniform mesh \mathcal{U} . Consequently, rather than a full $2D$ grid search, we can perform two $1D$ grid searches i.e. one for each component η_{ij}^1 and η_{ij}^2 . The $1D$ grid searches can be efficiently performed using a binary search algorithm; this is implemented in our Fortran90 code with the open source library `r8lib` [15]. In the worst case, the algorithmic complexities of these $1D$ searches are $\mathcal{O}(\log m)$ and $\mathcal{O}(\log n)$, for a single horizontal or vertical search, respectively. Therefore, the total complexity for the full grid search is $\mathcal{O}(N \log N)$, in the worst case.

3.6.3. Initial guess of target grid cell. In practice, a further optimization is possible since the binary search algorithm in `r8lib` that we use allows the user to provide a guess \mathcal{V}^* for the cell that contains the query point η_{ij} . Since the deformed mesh \mathcal{T}_η has the same connectivity structure as \mathcal{U} , we can loop through the query points one horizontal “slice” of the mesh at a time, and use the cell found from the previous query point as our guess $\mathcal{V}^* = \mathcal{I}_1^* \times \mathcal{I}_2^*$ for the current query point η_{ij} . If $\eta_{ij}^1 \notin \mathcal{I}_1^*$, then the algorithm looks in the intervals immediately to the left and right of \mathcal{I}_1^* , and if these also do not contain η_{ij}^1 , then a binary search is performed on the remaining portion of the $1D$ grid. The same is true for η_{ij}^2 . Since the deformed mesh is smooth and has the same connectivity structure as \mathcal{U} , it is highly likely that consecutive query points are contained in the same, or adjacent, or nearby cells. In this way, the grid search time is further reduced, and in particular, the complexity improves from $\mathcal{O}(N \log N)$ to $\mathcal{O}(N)$, which is optimal. We demonstrate this with an explicit example c.f. Figure 4. Further grid searching optimizations (e.g. using the grid search information from the previous RK4 stage or pseudo-time step) are possible, but we have not found them to be necessary.

⁷Except for the first stage of the first pseudo-time step, which does not require any interpolation.

3.6.4. Fast construction of bicubic interpolant. Once the grid cell containing η_{ij} is found, we use a standard bicubic interpolant to approximate f over a single cell $\mathcal{V}^* = [y_1^*, y_1^* + \Delta y_1] \times [y_2^*, y_2^* + \Delta y_2]$. It is convenient to map \mathcal{V}^* to the unit square by appropriately scaling and translating i.e. we set $\bar{y}_i = \frac{y_i - y_i^*}{\Delta y_i}$ for $i = 1, 2$, and use an interpolant of the form

$$\bar{f}(\bar{y}_1, \bar{y}_2) = \sum_{r,s=1}^3 \alpha_{rs} \bar{y}_1^{r-1} \bar{y}_2^{s-1}$$

to approximate an appropriately rescaled f over $\bar{y} \in [0, 1]^2$. The 4×4 matrix of coefficients α_{rs} is unknown and needs to be computed. Since there are 16 coefficients, we require 16 data points to solve the linear system for α_{rs} , and we use the values of f , $\Delta y_1 D_1 f$, $\Delta y_2 D_2 f$, and $\Delta y_1 \Delta y_2 D_{12} f$ at each of the four corners of the cell, where the derivatives are computed using FFT. The coefficients α_{rs} are then found by solving a linear system with a 16×16 coefficient matrix L . Since the approximating function \bar{f} is always defined on $[0, 1]^2$, the entries of L are fixed constants independent of the query point, and the inverse L^{-1} can be precomputed. Note also that if consecutive query points lie within the same cell, the corresponding coefficients of \bar{f} are the same for both and do not need to be recomputed.

3.6.5. Precomputing derivatives of v . The interpolant construction described above is for an arbitrary function f , and requires computation of the derivatives Df and $D_{12}f$ on the uniform mesh \mathcal{U} . As we shall demonstrate, the grid searching routine has optimal linear complexity $\mathcal{O}(N)$; the derivative computations, on the other hand, are performed with FFT, which is $\mathcal{O}(N \log N)$. Therefore the complexity of each interpolation call is $\mathcal{O}(N \log N)$, and the complexity of the flowmap integration is then $\mathcal{O}(N \log N / \Delta \tau)$.

However, precomputing the derivatives of f improves the complexity of each interpolation call to $\mathcal{O}(N)$. Specifically, for the interpolation $v \circ \eta(x, \tau)$, we require the derivatives $Dv(y, \tau)$ and $D_{12}v(y, \tau)$ for each $0 \leq \tau \leq 1$. From (14), we can compute

$$D_i v^j(y, \tau) = \frac{D_i \bar{v}^j - \tau v^j D_i F}{\tau F + (1 - \tau)}, \quad (26a)$$

$$D_{12} v^j(y, \tau) = \frac{D_{12} \bar{v}^j - \tau [v^j D_{12} F + D_1 v^j D_2 F + D_2 v^j D_1 F]}{\tau F(y) + (1 - \tau)}, \quad (26b)$$

for $i, j = 1, 2$.

Therefore, we can precompute and store the derivatives $D\bar{v}^j$, $D_{12}\bar{v}^j$, DF , and $D_{12}F$ before the flowmap integration step, then construct the required derivatives for interpolation at each time τ using (26) in $\mathcal{O}(N)$ operations. The complexity of flowmap integration is then $\mathcal{O}(N / \Delta \tau)$.

The derivatives of \bar{v} used in (26) are always computed with FFT and are (at least) 2nd order accurate. If the function G satisfies the Neumann condition, then derivatives of F are also computed with FFT; otherwise, we use CD2 in the interior of Ω and 2nd order one-sided differences at the boundary.

3.6.6. Interpolation experiments. Next, we perform a numerical experiment to demonstrate the efficiency of our fast interpolation implementation. We return to the circular target Jacobian function (25) and use SAM to generate a sequence of progressively finer meshes \mathcal{T} , starting with 128^2 cells and doubling the resolution in each direction until the final mesh contains 8192^2 cells. Then, we perform a single interpolation of a given function f from the uniform mesh \mathcal{U} to \mathcal{T} ,

and calculate the computational runtime of the interpolation procedure. We shall compare our fast bicubic algorithm with (a) bicubic interpolation with brute force grid searching, and (b) an industry standard cubic spline interpolation package `PPPack` [14]. The latter algorithm provides a more reasonable benchmark against which to compare our method.

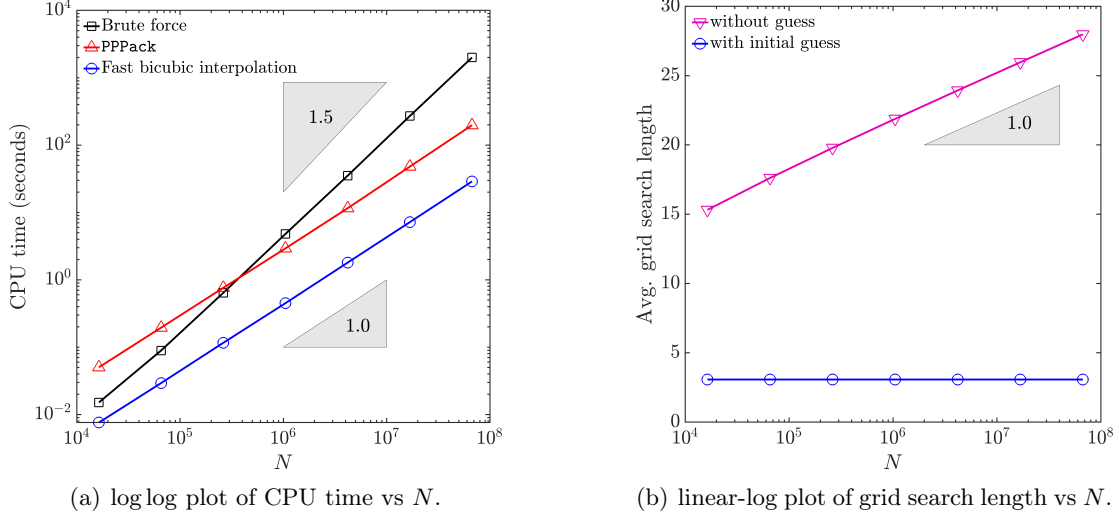


Figure 4: Plots demonstrating the efficiency of the simple optimized bicubic interpolation algorithm. Figure (a) is log log plot of CPU time vs number of cells N for different interpolation methods, and Figure (b) is linear-log plot of average search path length vs N for the fast interpolation routine with and without initial guessing.

The results from the timing experiment are provided in Figure 4(a). Our fast interpolation algorithm is approximately 7 times faster than `PPPack`, and about 70 times faster than the brute force approach at 8192^2 cell resolution. Moreover, both our fast interpolation and `PPPack` exhibit optimal linear complexity $\mathcal{O}(N)$, whereas the brute force approach is $\mathcal{O}(N^{1.5})$. The use of an initial guess in our interpolation algorithm is responsible for the improvement from $\mathcal{O}(N \log N)$ to $\mathcal{O}(N)$. For a given mesh, define the *average grid search path length* as the average number of intervals (both horizontal and vertical) that need to be searched during interpolation. Then, as shown in Figure 4(b), the grid search path length remains constant ≈ 3 as the mesh is refined, which results in $\mathcal{O}(N)$ complexity. On the other hand, if an initial guess is not used, then the grid search path length grows like $\log N$ and the complexity of the algorithm degrades to $\mathcal{O}(N \log N)$.

We conclude this subsection by mentioning two other grid searching procedures that have been utilized in the context of grid generation [33], namely ray tracing and distance searching. The main advantage of these methods is that they can be used on deformed grids; on the other hand, they are of complexity $\mathcal{O}(N^2)$ in the worst case, and consequently too slow for our purposes of time-dependent dynamic mesh generation. It is therefore crucial that the algorithms we develop are formulated on a uniform mesh so as to take advantage of the simple (but powerful) optimized interpolation routine.

3.6.7. Total complexity of Algorithm 1. The algorithmic complexity of SAM as described in Algorithm 1 is computed as the sum of the complexity of each of its steps. The FFT solve is $\mathcal{O}(N \log N)$. Each interpolation call is $\mathcal{O}(N)$ as shown in Figure 4(a). The number of interpolation calls is $\mathcal{O}(1/\Delta\tau^*) = \mathcal{O}(\sqrt{N})$ by (23), so that the complexity of the flowmap integration is $\mathcal{O}(N^{1.5})$. All other computations in Algorithm 1 are $\mathcal{O}(N)$. Therefore, the flowmap integration step is the dominating calculation and Algorithm 1 is $\mathcal{O}(N^{1.5})$. This is demonstrated in Figure 5, which shows

a breakdown of the computational runtime for $N = 32^2$ to $N = 2048^2$.

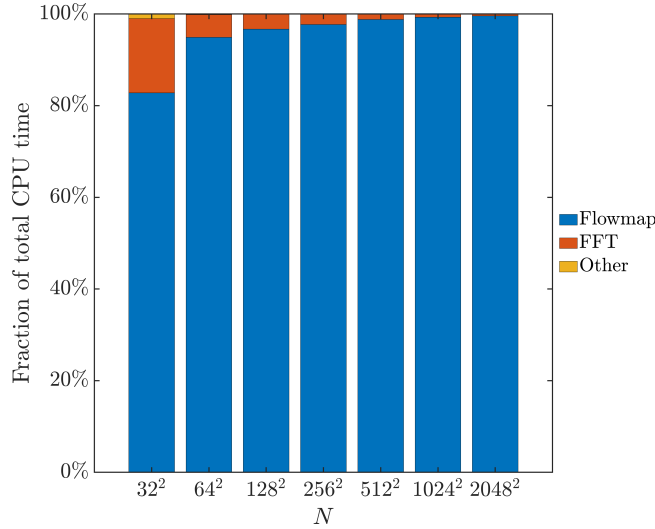


Figure 5: Computational runtime breakdown of Algorithm 1 for $N = 32^2$ through $N = 2048^2$.

The $\mathcal{O}(N^{1.5})$ complexity of SAM is worse than the state-of-the-art MK mesh generation scheme [22, 18], which appears to be of optimal linear complexity $\mathcal{O}(N)$. However, we note the following observations:

1. First, the MK solutions are 2nd order accurate, whereas the $\mathcal{O}(N^{1.5})$ complexity of SAM is for 4th order accurate solutions using the scaling (23). For 2nd order accuracy, we instead use (24), and the complexity of the SAM scheme improves to $\mathcal{O}(N^{1.25})$.
2. Next, though the CPU runtimes for MK and SAM scale like $\mathcal{O}(N)$ and $\mathcal{O}(N^{1.25})$, respectively, the constants in front of the respective coefficients are very different; in particular, the coefficient of $N^{1.25}$ for SAM is approximately two orders of magnitude smaller than the coefficient of N for MK. Consequently, SAM is faster than MK for a large range of resolutions up to (at least) $N \approx 4 \times 10^{12}$, as will be demonstrated in Section 3.7.
3. The solutions in the MK scheme are obtained by an iterative process which terminates when the nonlinear residuals have converged within some relative error tolerance ϵ_r . In [22], this tolerance is fixed as $\epsilon_r = 10^{-4}$, and the authors show that the algorithm is of linear complexity for some bounded range of resolutions $N \leq N_{\epsilon_r}$ that depends on ϵ_r . For $N > N_{\epsilon_r}$, the fixed value of ϵ_r is insufficient to ensure 2nd order convergence of the residuals. The value of ϵ_r must therefore be decreased, and the MK runtimes increase accordingly. It is unclear to us precisely how this affects the complexity of the MK scheme, but it is highly likely that SAM is faster than MK even for very large grids with $N > 4 \times 10^{12}$. This issue is discussed further with an explicit example in Section 3.7.

3.7. Benchmarking against a state-of-the-art mesh generation scheme

Now, we perform a numerical experiment to benchmark SAM against the state-of-the-art MK mesh generation scheme [22], a brief description of which is provided in Appendix C.

3.7.1. Mesh with radially symmetric target Jacobian function. The test problem [22] we consider is as follows: the domain is $\Omega = [0, 1]^2$, and the target Jacobian function is

$$\bar{G}(y) = 2 + \cos(8\pi r), \quad (27)$$

where $r = \sqrt{(y^1 - 0.5)^2 + (y^2 - 0.5)^2}$ is the radial coordinate. The 32^2 cell mesh computed with SAM is shown in Figure 6.

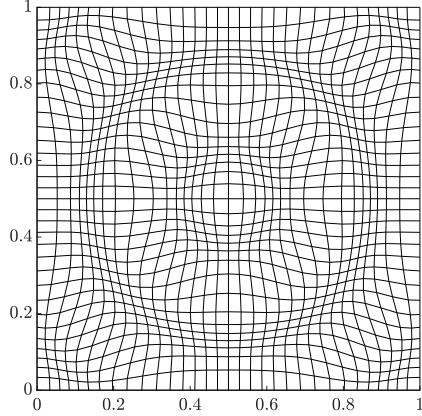


Figure 6: 32×32 mesh \mathcal{T} for the radial sinusoidal target function (27). The mesh is computed using SAM without boundary smoothing to enforce the Neumann condition.

The function \bar{G} is radially symmetric, and consequently does not satisfy the Neumann condition $D\bar{G} \cdot \nu \neq 0$ c.f. Section 3.3. As such, the resulting solutions computed with SAM do not display 2nd order accuracy in the limit $N \rightarrow \infty$, though, as shown in Table 2, the order of convergence only degrades to approximately 1.8 for the resolutions considered. Nonetheless, we shall additionally consider a modified version of this test problem in which the function $\bar{G}(y)$ in (27) is replaced by the function $\bar{G}^*(y)$, where $\bar{G}^*(y)$ is such that $D\bar{G}^* \cdot \nu = 0$ on $\partial\Omega$. The function \bar{G}^* is equal to \bar{G} in the interior of Ω , but is mollified with an appropriate cut-off function in a small region near the boundary $\partial\Omega$ to enforce the Neumann condition (see Appendix B for further details). The mesh \mathcal{T}^* produced using SAM with \bar{G}^* is shown in Figure 7(a), and a comparison with the mesh \mathcal{T} for \bar{G} is shown in Figure 7(b), from which it can be seen that the two meshes are very similar: they are nearly identical in the interior, with small differences near the boundary. While the solutions for \bar{G} do not attain the full 2nd order accuracy, the solutions for \bar{G}^* do.

We compute a sequence of meshes for $N = 16^2$ up to $N = 256^2$ using SAM. The L^2 Jacobian errors \mathcal{E}_2 , computed with formula (18), are listed in Table 2, along with the errors for the MK scheme obtained from [22]. The magnitude of the errors are roughly the same for both schemes at the resolutions considered. In particular, while the SAM solutions for \bar{G} only display ≈ 1.8 order of convergence, the magnitude of the errors is better than MK at lower resolutions, and similar at higher resolutions. We note that the lower order of convergence of the SAM solutions at low-resolutions is not due to larger errors at these resolutions, but rather due to the high accuracy of the spectral solver at very low-resolutions. Consequently, the order of accuracy appears lower for N small, but increases as N increases. The SAM solutions for \bar{G}^* have smaller errors than MK across all the resolutions considered. Moreover, the SAM solutions for \bar{G}^* display 2nd order accuracy as N increases⁸. We also find that the L^2 mesh displacement $\|\psi(x) - x\|_{L^2} \approx 0.0178$ is comparable to the value of 0.0174 for MK reported in Table 1 of [22].

⁸We have verified this up to $N = 2048^2$ but for brevity do not show the results here.

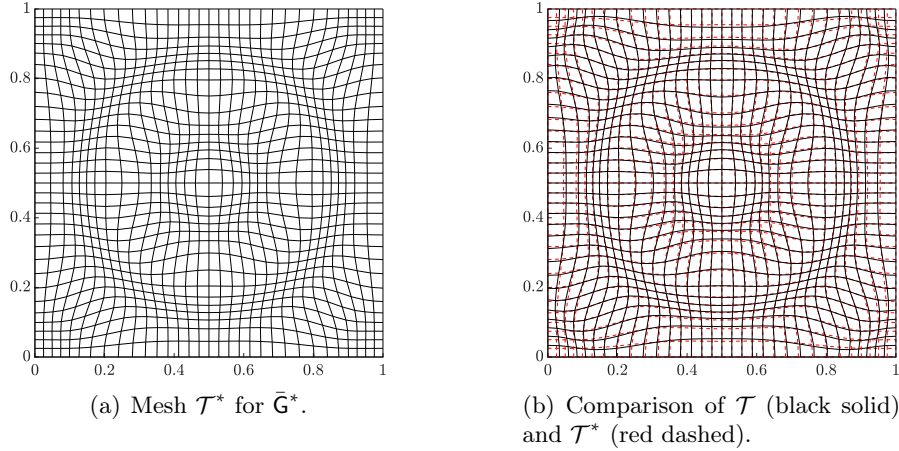


Figure 7: SAM algorithm with boundary smoothing for the radial sinusoidal target function (27). Figure (a) is the 32×32 cell mesh \mathcal{T}^* produced for the modified target Jacobian \bar{G}^* , and Figure (b) is a comparison of the mesh \mathcal{T} without boundary smoothing for the target Jacobian \bar{G} (black solid), and the mesh \mathcal{T}^* for \bar{G}^* (red dashed).

Scheme		Cells				
		16×16	32×32	64×64	128×128	256×256
MK	Error	9.64×10^{-2}	2.80×10^{-2}	5.78×10^{-3}	1.46×10^{-3}	3.67×10^{-4}
	Order	–	1.78	2.28	1.99	1.99
SAM with \bar{G}	Error	6.30×10^{-2}	2.35×10^{-2}	6.72×10^{-3}	2.00×10^{-3}	5.87×10^{-4}
	Order	–	1.43	1.80	1.75	1.77
SAM with \bar{G}^*	Error	2.50×10^{-2}	1.70×10^{-2}	5.43×10^{-3}	1.44×10^{-3}	3.35×10^{-4}
	Order	–	0.56	1.64	1.92	2.10

Table 2: Comparison of L^2 Jacobian errors and convergence rates for the MK and SAM schemes applied to (27). The data for the MK scheme is taken from Table 1 of [22].

3.7.2. CPU runtime comparison of SAM vs MK. Next, we benchmark the computational efficiency of our SAM scheme against the MK scheme. We list in Table 3 the CPU runtimes for the MK scheme and the SAM scheme, where the MK runtimes are taken from Table 1 of [22]. To account for the different machines on which the MK and SAM schemes were run on, we multiply the MK runtimes by a factor of $4/3$, where the factor of $4/3$ is determined from a machine comparison experiment, the details of which are provided in Appendix C. We then list the speed-up factor of the SAM scheme over the MK scheme in the final row of Table 3. At lower resolutions, the SAM scheme is more than two orders of magnitude in time faster than the MK scheme. At higher resolutions, this speed-up factor degrades due to the $\mathcal{O}(N)$ complexity of the MK scheme vs the $\mathcal{O}(N^{1.25})$ complexity of SAM. Nonetheless, SAM is still 50 times faster than MK at $N = 256^2$.

Scheme		Cells				
		16×16	32×32	64×64	128×128	256×256
MK	T_{CPU}	0.13	0.53	1.73	6.53	25.33
SAM	T_{CPU}	0.001	0.004	0.017	0.124	0.522
	speed-up factor	111	134	103	53	49

Table 3: CPU runtimes for the MK scheme vs the SAM scheme. The results for the MK scheme are taken from Table 1 of [22] then multiplied by $\frac{4}{3}$ to account for machine difference.

The apparent $\mathcal{O}(N)$ complexity of the MK scheme suggests that, at some critical resolution, the MK scheme becomes more computationally efficient than SAM. Based on the known time complexities of the MK and SAM schemes, and the data reported in Table 3, we can estimate the critical resolution N at which MK becomes more computationally efficient than SAM as $N \approx 4 \times 10^{12}$. For 2D grids, this means that SAM is faster than MK for grids of resolution up to approximately $N \approx 2^{21} \times 2^{21}$, which is many orders of magnitude greater than the largest resolutions considered in this work. Assuming the same speed-up factors for 3D grids, SAM is faster up to resolutions of approximately $N \approx 16,000^3$.

In fact, however, the $\mathcal{O}(N)$ complexity of MK is only for a *bounded range of resolutions* N for which the largest residual error smaller than the (constant) relative tolerance is sufficient to ensure convergence of the numerical solution. Indeed, as the mesh is refined, this relative tolerance must be decreased, and the runtimes increase accordingly. While we are not aware of how this affects the complexity of the MK scheme, it is nonetheless highly likely that SAM is faster than MK even for very large grids with $N > 4 \times 10^{12}$.

4. FAST DYNAMIC ADAPTIVE MESHING

Having described in detail the formulation and implementation of the static SAM scheme in Section 3, we next describe our dynamic mesh generation scheme.

4.1. Dynamic formulation

Let Ω_{ref} again denote the reference domain, with coordinates $x = (x^1, x^2) \in \Omega_{\text{ref}}$. Given a time interval $t \in [0, T]$, we seek to construct a time dependent diffeomorphism $\psi : \Omega_{\text{ref}} \times [0, T] \rightarrow \Omega$ mapping, for each $t \in [0, T]$, the reference domain Ω_{ref} to the physical domain Ω . Again, we assume that Ω_{ref} and Ω represent the same mathematical domain. We denote the time-dependent mesh on Ω by $\mathcal{T}(t)$, which will be found as the image of \mathcal{T}_{ref} under the action of $\psi(\cdot, t)$.

The time-dependent map $\psi : \Omega_{\text{ref}} \times [0, T] \rightarrow \Omega$ is constructed by prescribing, for each $t \in [0, T]$, its Jacobian determinant. Let $\mathbf{G} : \Omega \times [0, T] \rightarrow \mathbb{R}^+$ denote a given time-dependent (physical) target Jacobian function. Then ψ satisfies

$$\begin{cases} \det \nabla \psi(x, t) = \mathbf{G} \circ \psi(x, t), & (x, t) \in \Omega_{\text{ref}} \times [0, T] \\ \psi(x, t) \cdot \nu = x \cdot \nu, & (x, t) \in \partial \Omega_{\text{ref}} \times [0, T] \end{cases} \quad (28a)$$

$$(28b)$$

The target Jacobian function \mathbf{G} must satisfy, for each $t \in [0, T]$, the following integral constraint to ensure that (28) has a solution:

$$\int_{\Omega} \frac{1}{\mathbf{G}(y, t)} dy = \int_{\Omega_{\text{ref}}} \frac{\det \nabla \psi(x, t)}{\mathbf{G} \circ \psi(x, t)} dx = |\Omega|. \quad (29)$$

4.1.1. Temporal discretization. We uniformly discretize the time domain $[0, T]$ into K intervals of length Δt and set $t_k = k\Delta t$ for $k = 0, 1, \dots, K$. Denote $\mathbf{G}_k := \mathbf{G}(\cdot, t_k)$, $\psi_k := \psi(\cdot, t_k)$, and $\mathcal{T}_k = \mathcal{T}(t_k)$. Then each $\psi_k : \Omega_{\text{ref}} \rightarrow \Omega$ is a diffeomorphism satisfying

$$\begin{cases} \det \nabla \psi_k(x) = \mathbf{G}_k \circ \psi_k(x), & x \in \Omega_{\text{ref}} \\ \psi_k(x) \cdot \nu = x \cdot \nu, & x \in \partial \Omega_{\text{ref}} \end{cases} \quad (30a)$$

$$(30b)$$

with each target Jacobian function $\mathbf{G}_k : \Omega \rightarrow \mathbb{R}^+$ satisfying the integral constraint

$$\int_{\Omega} \frac{1}{\mathbf{G}_k(y)} dy = \int_{\Omega_{\text{ref}}} \frac{\det \nabla \psi_k(x)}{\mathbf{G}_k \circ \psi_k(x)} dx = |\Omega|. \quad (31)$$

4.1.2. Discussion. The simplest possible strategy for (30) is to compute each map ψ_k using static SAM. Our numerical experiments indicate that static SAM is optimal in terms of efficiency for a single mesh generation call. However, for unsteady fluids simulations which require dynamic meshing at every time-step, the use of static SAM can be expensive due to the computational bottleneck in the flowmap integration stage.

Specifically, suppose that the target Jacobian function has large deviation from the identity i.e. $\|1/\mathbf{G} - 1\|_{L^\infty} \gg 1$. Then the associated potential Φ solving (11) has large gradients, and the flowmap velocity (14) will therefore be large in magnitude. Consequently, many pseudo-time steps will be required in the flowmap integration to preserve stability and accuracy of the computed numerical solution for $\eta(x, \tau)$. Each pseudo-time step requires the evaluation of the composition $\mathbf{v} \circ \eta(x, \tau)$, numerically computed by interpolation, and this is the calculation which requires the most computational expense. In the next section, we resolve this issue via a novel reformulation of (30).

4.2. Reformulation in terms of near-identity maps

4.2.1. The perturbation formulation. We next provide a reformulation of the dynamic mesh generation equations (30) so that, at each time stage k , the diffeomorphism we solve for is a near-identity transformation of the reference domain Ω_{ref} . This new *perturbation formulation* for dynamic meshing preserves space-time smoothness of the map $\psi(x, t)$, but also allows for a simple and fast numerical implementation.

Assume that we are given the map ψ_k and the target Jacobian functions \mathbf{G}_k and \mathbf{G}_{k+1} , and suppose that we wish to compute the map ψ_{k+1} . Rather than computing the map ψ_{k+1} directly by solving (30), we instead solve for the *perturbation map* $\delta\psi_{k+1} : \Omega_{\text{ref}} \rightarrow \Omega_{\text{ref}}$ defined implicitly by

$$\psi_{k+1}(x) = \psi_k \circ \delta\psi_{k+1}(x). \quad (32)$$

That is, we suppose that the map ψ_{k+1} can be found as the image of ψ_k acting on a near-identity transformation $\delta\psi_{k+1}$ on the reference domain Ω_{ref} (see Figure 8).

The chain rule and inverse function theorem show that $\delta\psi_{k+1}$ satisfies the following equation

$$\begin{cases} \det \nabla \delta\psi_{k+1}(x) = P_{k+1} \circ \delta\psi_{k+1}(x), & x \in \Omega_{\text{ref}} \\ \delta\psi_{k+1}(x) \cdot \nu = x \cdot \nu, & x \in \partial\Omega_{\text{ref}} \end{cases} \quad (33a)$$

$$(33b)$$

with the function $P_{k+1} : \Omega_{\text{ref}} \rightarrow \mathbb{R}^+$ defined as

$$P_{k+1}(x) = \left(\frac{\mathbf{G}_{k+1}}{\mathbf{G}_k} \right) \circ \psi_k(x). \quad (34)$$

4.2.2. The smooth-in-time adaptive meshing algorithm. The system (33) is of exactly the same form as (8), and the identical solution procedure described in Section 3.2 for static mesh generation can therefore be used to find the solution $\delta\psi_{k+1}$. Then ψ_{k+1} is computed according to (32). A complete description of the smooth-in-time dynamic meshing scheme is provided in Algorithm 2.

4.2.3. Discussion. The key to the efficiency of dynamic SAM is the reformulation in terms of the perturbation map $\delta\psi_{k+1}$ satisfying (33). Specifically, while it may be that both \mathbf{G}_k and \mathbf{G}_{k+1} have large deviation from 1 i.e. $\|1/\mathbf{G}_k - 1\|_{L^\infty} \gg 1$ and $\|1/\mathbf{G}_{k+1} - 1\|_{L^\infty} \gg 1$, we may nonetheless have that

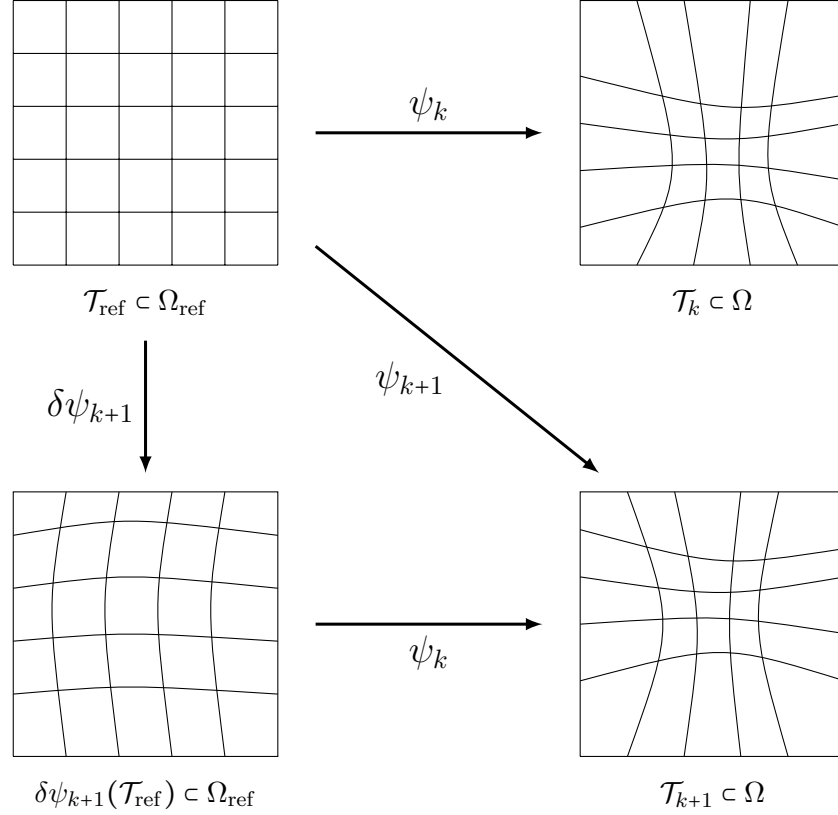


Figure 8: Schematic of the meshes, and the maps between them, for dynamic mesh generation.

$\|1/P_{k+1} - 1\|_{L^\infty} \ll 1$. Indeed, this is the case in ALE simulations, which are naturally constrained by a CFL condition that limits the evolution of the numerical solution over a single time-step. Since $\|1/P_{k+1} - 1\|_{L^\infty} \ll 1$, this means that only very few pseudo-time steps are required for the flowmap integration, which greatly improves the speed of the algorithm. In this paper we take $\Delta\tau = 1$ in dynamic SAM for all resolutions i.e. only a single pseudo-time step is taken. Additionally, we note that since the dynamic scheme is based directly on the static scheme, its implementation is similarly simple, and the resulting numerical solutions are accurate with high convergence rates.

We emphasize here that our perturbation formulation (33) differs from the methods considered in [68, 33] in an important way. In particular, our perturbation map $\delta\psi_{k+1}$ is a near identity transformation of the *uniform reference domain* Ω_{ref} , whereas the schemes in [68, 33] define a perturbation map via $\bar{\psi}_{k+1} = \delta\bar{\psi}_{k+1} \circ \bar{\psi}_k$, rather than through (32). This means that the $\bar{\psi}_k$ solutions in [68, 33] are different from our ψ_k SAM solutions. Moreover, the equation for $\delta\bar{\psi}_{k+1}$ is posed on the deformed mesh \mathcal{T}_k , and thus neither the spectral solver for the Poisson problem (11), nor the fast bicubic interpolation procedure can be used. Consequently, SAM is simpler, faster, and more accurate than the schemes in [68, 33]. For instance, the scheme in [33] has order of accuracy 1.5, whereas our dynamic SAM solutions converge with 4th order accuracy if the data is sufficiently smooth. Additionally, the interpolation routine in [33] requires $\mathcal{O}(N^{1.5})$ grid searching on deformed grids, in contrast to our $\mathcal{O}(N)$ fast interpolation algorithm on uniform grids.

Algorithm 2 : DYNAMIC SAM

Step 1 : Set $t = 0$. Given an initial target Jacobian function $\mathbf{G}_0 : \Omega \rightarrow \mathbb{R}^+$, compute the initial diffeomorphism ψ_0 according to the static solution scheme from Section 3.2.

Step 2 : For $t = t_{k+1}$, assume that we are given the following: the map ψ_k and target Jacobian function $\mathbf{G}_k : \Omega \rightarrow \mathbb{R}^+$, both from the previous time step $t = t_k$, and the target Jacobian function $\mathbf{G}_{k+1} : \Omega \rightarrow \mathbb{R}^+$ at the current time level.

Define $P_{k+1} : \Omega_{\text{ref}} \rightarrow \mathbb{R}^+$ by (34), and assume that it satisfies the solvability condition

$$\int_{\Omega_{\text{ref}}} \frac{1}{P_{k+1}(x)} dx = \int_{\Omega_{\text{ref}}} \left(\frac{\mathbf{G}_k}{\mathbf{G}_{k+1}} \right) \circ \psi_k(x) dx = |\Omega_{\text{ref}}|, \quad (35)$$

In general, we will be given target Jacobian functions $\bar{\mathbf{G}}_k$ and $\bar{\mathbf{G}}_{k+1}$ such that the corresponding $\bar{P}_{k+1} = (\bar{\mathbf{G}}_{k+1}/\bar{\mathbf{G}}_k) \circ \psi_k$ does not satisfy (35). In this case, we define P_{k+1} according to the following normalization procedure:

$$\bar{Q}_{k+1}(x) = \frac{1}{\bar{P}_{k+1}(x)} \longrightarrow Q_{k+1}(x) = |\Omega| \frac{\bar{Q}_{k+1}(x)}{\int_{\Omega_{\text{ref}}} \bar{Q}_{k+1}(x) dx} \longrightarrow P_{k+1}(x) = \frac{1}{Q_{k+1}(x)}.$$

Step 3 : Solve (33) for the perturbation map $\delta\psi_{k+1} : \Omega_{\text{ref}} \rightarrow \Omega_{\text{ref}}$ using the solution procedure in Section 3.2.

Step 4 : Define $\psi_{k+1} : \Omega_{\text{ref}} \rightarrow \Omega$ by (32). If $t_{k+1} = T$, then stop; otherwise, set $t = t_{k+2}$, and return to **Step 2**.

4.3. Restarted dynamic mesh generation

The perturbation formulation (33), by design, follows the time history of $\psi(x, t)$. That is to say, the solution $\psi(x, t)$ at time $t = t_k$ depends upon the solution for all $t < t_k$. As such, numerical solutions to (33) are susceptible to increasing grid distortion and mesh tangling, a common ailment of Lagrangian-type methods. To mitigate this issue, we can periodically *restart* the dynamic mesh generation by computing at time $t = t_k$ the map ψ_k directly with static SAM, rather than with dynamic SAM. In this way, the greater efficiency of dynamic SAM is utilized, while grid distortion errors are controlled with the use of static SAM, thereby preventing mesh tangling. The restarting criterion is chosen as $\lambda_k > \Lambda \lambda_{\text{ref}}$, where λ_k is the L^1 grid distortion at time step t_k , λ_{ref} is a ‘reference’ grid distortion (defined in Algorithm 3), and Λ is a user prescribed parameter. In this paper, we use $\Lambda = 1.01$. A description of our restarted dynamic SAM scheme is provided in Algorithm 3.

4.4. Numerical implementation aspects

The dynamic SAM solution process at each time-step t_k is essentially identical to static SAM, and we therefore refer to Section 3 for the main implementation details.

4.4.1. Stability and accuracy constraints for Δt and $\Delta \tau$. A key aspect of SAM is the consistency between the scaling of the pseudo-time step $\Delta \tau$ according to the stability condition (16) and the accuracy/efficiency constraint (23) c.f. Remark 1. When the target Jacobian \mathbf{G} has

Algorithm 3 : RESTARTED DYNAMIC SAM

Step 0 : Choose the maximum grid distortion parameter $\Lambda > 1$.

Step 1 : Set $t = 0$. Given an initial target Jacobian function $G_0 : \Omega \rightarrow \mathbb{R}^+$, compute the initial diffeomorphism ψ_0 according to the static solution scheme from Section 3.2. Let λ_{ref} be the (reference) L^1 grid distortion of the adaptive mesh \mathcal{T}_0 , computed according to (36).

Step 2 : For $t = t_{k+1} > 0$, compute the average grid distortion of the map ψ_k

$$\lambda_k := \left\| \frac{1}{2} \text{Tr} (\nabla \psi_k \nabla \psi_k^T) \right\|_{L^1} . \quad (36)$$

Step 3 : If $\lambda_k > \Lambda \lambda_{\text{ref}}$, then compute the map ψ_{k+1} using static SAM Algorithm 1 and recalculate λ_{ref} according to (36). Otherwise, compute ψ_{k+1} using dynamic SAM Algorithm 2. If $t_{k+1} = T$, then stop; otherwise, set $t = t_{k+2}$, and return to **Step 2**.

large deviation from 1, it is usually the case that (23) is the more stringent condition on $\Delta\tau$ than (16). For dynamic SAM, however, it is sometimes the case that (16) represents a similar or stronger condition on $\Delta\tau$ than (23), since both the function $P_{k+1}(x)$ and its derivatives are of similar magnitude (and close to zero). The consistency between (16) and (23) guarantees that dynamic SAM grids are constructed in both a stable and accurate manner.

Moreover, when dynamic SAM is implemented for ALE gas dynamics (or any hyperbolic system), a further consistency relation ensures that dynamic SAM grids can be constructed in a highly efficient manner with optimal complexity. We recall first that the *physical* time step Δt in an (Eulerian) simulation is constrained according to the CFL condition

$$\text{CFL} = \Delta t \cdot \mathcal{S} \left(\frac{1}{\Delta y^1} + \frac{1}{\Delta y^2} \right) \leq 1, \quad (37)$$

where, \mathcal{S} is the maximum wave speed of the flow. The condition (37) forces the time step Δt to decay like $\Delta t \sim 1/\sqrt{N}$ as $N \rightarrow \infty$, which is a constraint of exactly the same form as the conditions (16) and (23) on $\Delta\tau$. A Taylor series argument shows that

$$\begin{aligned} 1 - \frac{1}{P_{k+1}(x)} &= \Delta t \cdot \frac{\partial_t G(\psi(x, t_k), t_k)}{G(\psi(x, t_k), t_k)} + \mathcal{O}(\Delta t^2) \\ \implies \|1 - 1/P(\cdot, t)\|_{L^\infty} &= \mathcal{O}(\Delta t) = \mathcal{O}(1/\sqrt{N}), \end{aligned} \quad (38)$$

since $\partial_t G \sim \mathcal{O}(1)$ by (37). Since the stability condition for the pseudo-time step $\Delta\tau$ scales according to (16), and $\|v\|_{L^\infty} = \mathcal{O}(1/\sqrt{N})$ by (38), we see that $\Delta\tau = \mathcal{O}(1)$ i.e. the pseudo-time step $\Delta\tau$ can be kept fixed across resolutions N . Dynamic SAM is therefore designed to automatically satisfy both internal and external (i.e. in ALE implementations) consistency requirements.

5. DYNAMIC MESH GENERATION EXPERIMENTS

In this section, we present and discuss the results of several dynamic mesh generation experiments conducted with the static, dynamic, and restarted SAM algorithms. Unless otherwise stated, all experiments are conducted on the unit square $\Omega = [0, 1]^2$ with an equal number of cells in the horizontal and vertical directions $m = n = \sqrt{N}$.

5.1. Static mesh with large zoom-in factor

This static test problem demonstrates the ability of dynamic SAM to generate smooth meshes with large zoom-in factors which, in practical applications, can be used to track very small scale structures with only a few total number of cells. On the other hand, when the target function \mathbf{G} has large gradients (as is the case for large zoom-in meshes), numerical errors in the Poisson solve often lead to poor quality grids containing non-convex elements [22, 33].

As an example, consider the circular target Jacobian function $\mathbf{G}_\delta(y)$ given by (25) with $\sigma = 64$, $r = 0.2$, and $0 \leq \delta < 1$. When $\delta \approx 1$, static SAM is unable to produce grids with non-convex elements, regardless of the choice of pseudo-time step $\Delta\tau$. That is, for each N , there exists a corresponding δ_{\max} such that the grids produced with static SAM for $\delta > \delta_{\max}$ contain non-convex elements. An example of such a grid is shown for $N = 64^2$ and $\delta = 0.95$ in Figures 9(a) and 9(b). The function \mathbf{G}_δ is such that $\|1 - 1/\mathbf{G}_\delta\|_{L^\infty} \approx \frac{1}{1-\delta} \rightarrow \infty$ as $\delta \rightarrow 1$. When $\delta \approx 1$, large errors in the numerical solution of the Poisson problem lead to grids with non-convex elements.

Dynamic SAM provides a simple method for producing smooth grids with large zoom-in factor δ . We define the time-dependent function

$$\mathbf{G}(y, s) = (1 - s) + s\mathbf{G}_\delta(y). \quad (39)$$

Then (39) linearly interpolates between 1 at $s = 0$ and \mathbf{G}_δ at $s = 1$, and applying dynamic SAM with sufficiently many time steps Δs yields smooth grids with no non-convex elements. As an example, we set $\Delta s = 0.05$ and construct a 64^2 cell mesh using Algorithm 2 with $\delta = 0.996$ in (25). We take only a single pseudo-time step in the flowmap integration, and the total runtime of the simulation is only 0.65 seconds. The resulting grid, shown in Figures 9(c) and 9(d), is smooth with the smallest element approximately 250 times smaller than a uniform cell. In Section 7, we consider large zoom-in meshing for the more complicated Rayleigh-Taylor test.

5.2. Propagating circular front

5.2.1. Problem description. Our first dynamic mesh generation experiment tracks a circular front propagating radially outwards with radial velocity 1. The time-dependent target Jacobian function is defined as

$$\bar{\mathbf{G}}(y, t) = 1 - \delta \exp \left\{ - \left| \sigma \left[(y^1 - 0.5)^2 + (y^2 - 0.5)^2 - r(t)^2 \right] \right|^2 \right\}. \quad (40)$$

The parameters are chosen as $\delta = 0.75$, $\sigma = 64$, and the radius is $r(t) = 0.2 + t$. We generate a sequence of meshes for $0 \leq t \leq 0.1$.

The choice of time step Δt depends upon N as

$$\Delta t = \frac{0.64}{2\sqrt{N}}. \quad (41)$$

This choice of scaling for Δt is motivated by (37). Since the radial velocity of the propagating front is 1, we can estimate that the CFL number associated with (41) is 0.64.

5.2.2. Results. The 64^2 cell adaptive meshes $\mathcal{T}(t)$ for (40) are shown in the top row of Figure 10 at various times t . The computed meshes \mathcal{T}_k are smooth and are correctly resolved around the evolving circular front. The meshes $\delta\psi_k(\mathcal{T}_{\text{ref}})$ are shown at the same times in the bottom row of Figure 10; from these figures, it is clear that $\delta\psi_k(\mathcal{T}_{\text{ref}})$ is a near-identity transformation of the uniform mesh \mathcal{T}_{ref} . For this problem, the function \mathbf{G} is such that $\|1 - 1/\mathbf{G}(\cdot, t)\|_{L^\infty} \approx 2.43$. The perturbation density P , on the other hand, is an order of magnitude smaller at $\|1 - 1/P(\cdot, t)\|_{L^\infty} \approx 0.3$, which permits the use of the large pseudo-time step $\Delta\tau = 1$ in the flowmap integration.

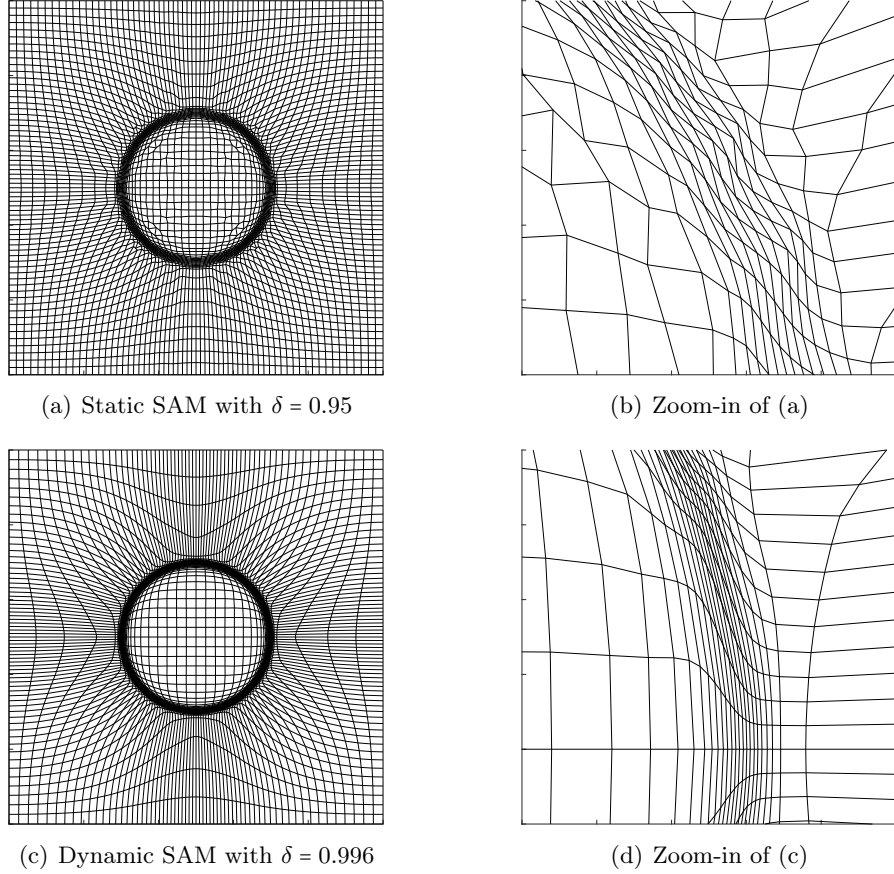


Figure 9: Test problem 5.1 demonstrating smooth large zoom-in meshing using dynamic SAM. Shown are the 64^2 cell meshes with large zoom-in parameter δ for the circular target Jacobian function (25). Figure (a) is the poor quality mesh containing non-convex elements produced with static SAM with $\delta = 0.95$, and (b) is a zoom-in of (a) near the refining region. Figure (c) is the smooth large zoom-in mesh produced with dynamic SAM with $\delta = 0.996$ and with smallest cell 250 times smaller than a uniform cell, and (d) is a zoom-in.

5.2.3. Comparison with static SAM. Next, we conduct a grid resolution study with N ranging from $N = 32^2$ to $N = 512^2$, and compare the results of dynamic SAM with those of static SAM. The Jacobian errors \mathcal{E}_2 at the final time $t = 0.1$ are shown in Table 4. Both schemes exhibit approximately 4th order accuracy, as expected, but the dynamic SAM solutions have slightly smaller errors. This is due to the higher accuracy of the Poisson solve in the dynamic method vs the static method.

Moreover, as shown in Table 4, dynamic SAM runtimes are consistently smaller than static SAM runtimes: the speed-up factor increases from 1.2 at $N = 32^2$ to 14.5 at $N = 512^2$. The runtimes in Table 4 show that, while static SAM is of complexity $\mathcal{O}(N^{1.5}/\Delta t) = \mathcal{O}(N^2)$, dynamic SAM is of optimal complexity $\mathcal{O}(N/\Delta t) = \mathcal{O}(N^{1.5})$.

5.3. Uniformly rotating patch

5.3.1. Problem description. Our next mesh generation experiment assesses the performance of SAM for target Jacobian functions of the form

$$\bar{G}(y, t) = \frac{1}{1 + M \exp \left\{ -\sigma \left| [(y^1 - 0.5 - r \cos(2\pi t))^2 + (y^2 - 0.5 - r \sin(2\pi t))^2 - R^2] \right|^2 \right\}}. \quad (42)$$

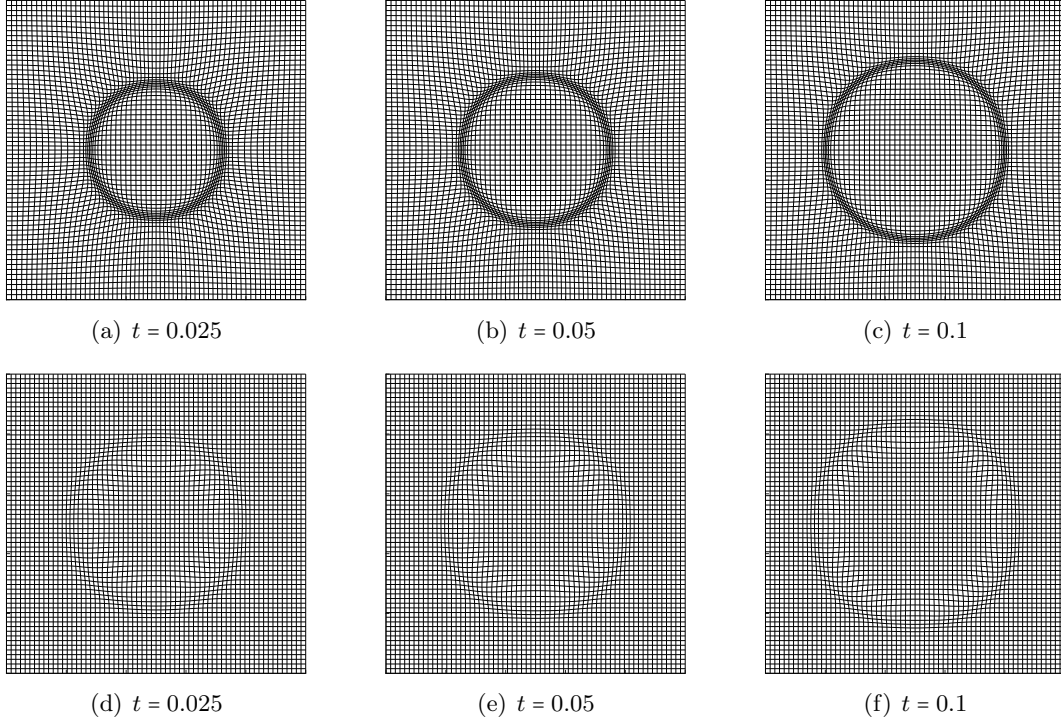


Figure 10: Test problem 5.2: tracking a propagating circular front modeling a shock wave. Shown are the 64^2 cell meshes produced using dynamic SAM for the circular target Jacobian function (40). The top row shows the adaptive meshes $\mathcal{T}(t)$, while the bottom row shows the corresponding “perturbation meshes” $\delta\psi_k(\mathcal{T}_{\text{ref}})$ that are clearly near identity deformations of the uniform mesh.

Equation (42) forces the mesh to concentrate nodes within a uniformly rotating (with angular velocity $\omega = 2\pi$) circular patch of radius $R > 0$, whose center is a distance $r \geq 0$ from $(0.5, 0.5)$. The constant $M \geq 0$ determines the zoom-in factor, and σ controls the width of the transition region from fine to coarse scale of the mesh.

5.3.2. Comparison with the schemes in [72]. The case $M = 5$, $\sigma = 50$, $r = 0.25$, and $R = 0.1$ in (42) corresponds to a test problem from [72]. Therein, the authors compare four different mesh generation methods and conclude that the so-called Parabolic Monge-Kantorovich method (PMKP) is the best method among the four for (42), both in terms of accuracy as well as efficiency. The PMKP method is similar to the MK scheme, but replaces the nonlinear Newton-Krylov solver in MK with a parabolization (in pseudo-time τ) and time-stepping until a steady state is reached. The solution in PMKP is only found in the asymptotic limit $\tau \rightarrow \infty$, whereas the SAM solution is computed at pseudo-time $\tau = 1$. Moreover, the explicit integration of the parabolic PDE requires that the pseudo-time step scales like $\Delta\tau \sim \frac{1}{N}$ to ensure 2nd order convergence. In contrast, the flowmap ODEs solved for in static SAM require only that $\Delta\tau \sim \frac{1}{\sqrt{N}}$, while for dynamic SAM we can keep $\Delta\tau = \mathcal{O}(1)$.

We set $N = 40^2$, $\Delta t = 0.01$, and generate a sequence of meshes for $0 \leq t \leq 1$. The adaptive meshes generated with static, dynamic, and restarted SAM are shown in Figure 11 at various times t . The Jacobian errors, mean grid distortion, and cumulative simulation runtimes are provided in Table 5.

Scheme		Cells				
		32×32	64×64	128×128	256×256	512×512
Static SAM	\mathcal{E}_2	3.45×10^{-2}	9.88×10^{-3}	5.92×10^{-4}	2.97×10^{-5}	1.97×10^{-6}
	Order	–	1.8	4.1	4.3	3.9
	T_{CPU} (sec)	0.12	1.4	21.1	305	5247
Dynamic SAM	\mathcal{E}_2	3.81×10^{-2}	5.35×10^{-3}	3.81×10^{-4}	2.72×10^{-5}	1.77×10^{-6}
	Order	–	2.8	3.8	3.8	4.0
	T_{CPU} (sec)	0.10	0.74	5.22	42.6	363
	speed-up factor	1.2	1.9	4.0	7.2	14.5

Table 4: Test problem 5.2: tracking a propagating circular front. We list the L^2 Jacobian errors \mathcal{E}_2 at $t = 0.1$, convergence rates, and total CPU runtimes for static and dynamic SAM. The results confirm that dynamic SAM produces high order accurate solutions and is of optimal complexity.

For the purposes of comparison with [72], we also provide the *mesh fidelity measure* $\hat{\mathcal{E}}_2$, defined by

$$\hat{\mathcal{E}}_2 := \left| \|\mathcal{J}(\cdot, t)/G \circ \psi(\cdot, t)\|_{L^2} - 1 \right|. \quad (43)$$

The superior accuracy of SAM produces fidelity measures $\hat{\mathcal{E}}_2$ that are two orders of magnitude smaller than those produced with the PMKP method (see Tables 6 and 7 in [72]). Moreover, the SAM runtimes are more than an order magnitude smaller than the PMKP runtimes provided in [72] e.g. 2.861 sec vs 75 sec for static SAM vs PMKP.

Scheme		Time				
		$t = 0$	$t = 0.25$	$t = 0.5$	$t = 0.75$	$t = 1.0$
Static SAM	$\hat{\mathcal{E}}_2$	2.50×10^{-4}	2.50×10^{-4}	2.50×10^{-4}	2.50×10^{-4}	2.50×10^{-4}
	\mathcal{E}_2	1.632×10^{-2}	1.632×10^{-2}	1.632×10^{-2}	1.632×10^{-2}	1.632×10^{-2}
	λ	1.190	1.190	1.190	1.190	1.190
	T_{CPU} (sec)	0.025	0.746	1.456	2.163	2.861
Dynamic SAM	$\hat{\mathcal{E}}_2$	2.50×10^{-4}	2.45×10^{-4}	2.88×10^{-4}	3.07×10^{-5}	6.14×10^{-5}
	\mathcal{E}_2	1.632×10^{-2}	1.346×10^{-2}	1.468×10^{-2}	1.693×10^{-2}	2.024×10^{-2}
	λ	1.190	1.223	1.330	1.491	1.710
	T_{CPU} (sec)	0.025	0.332	0.654	1.001	1.338
Restarted SAM	$\hat{\mathcal{E}}_2$	2.50×10^{-4}	3.10×10^{-4}	2.49×10^{-4}	3.05×10^{-4}	2.60×10^{-4}
	\mathcal{E}_2	1.632×10^{-2}	1.013×10^{-2}	1.578×10^{-2}	8.467×10^{-2}	1.513×10^{-2}
	λ	1.190	1.194	1.190	1.196	1.190
	T_{CPU} (sec)	0.025	0.381	0.753	1.100	1.465

Table 5: Test problem 5.3: tracking a uniformly rotating patch. We provide the mesh fidelity measure $\hat{\mathcal{E}}_2$, L^2 Jacobian error \mathcal{E}_2 , L^1 distortion λ , and cumulative CPU runtime T_{CPU} at various times t for the static, dynamic, and restarted SAM schemes. The mesh fidelity measures $\hat{\mathcal{E}}_2$ of SAM solutions are two orders of magnitude smaller than those provided in [72]. Additionally, restarted SAM is more than 50 times faster than the schemes in [72].

Since static SAM constructs the map ψ directly from the uniform mesh, the meshes at $t = 0.25, 0.5, 0.75, 1.0$ are simply rotated versions of the initial grid. This is confirmed in Table 5, which shows that static SAM produces grids with identical grid quality metrics at these times.

Dynamic SAM is twice as fast as static SAM for this test; on the other hand, it necessarily tracks the history of the simulation, and the rotating target Jacobian produces grids with increasing levels

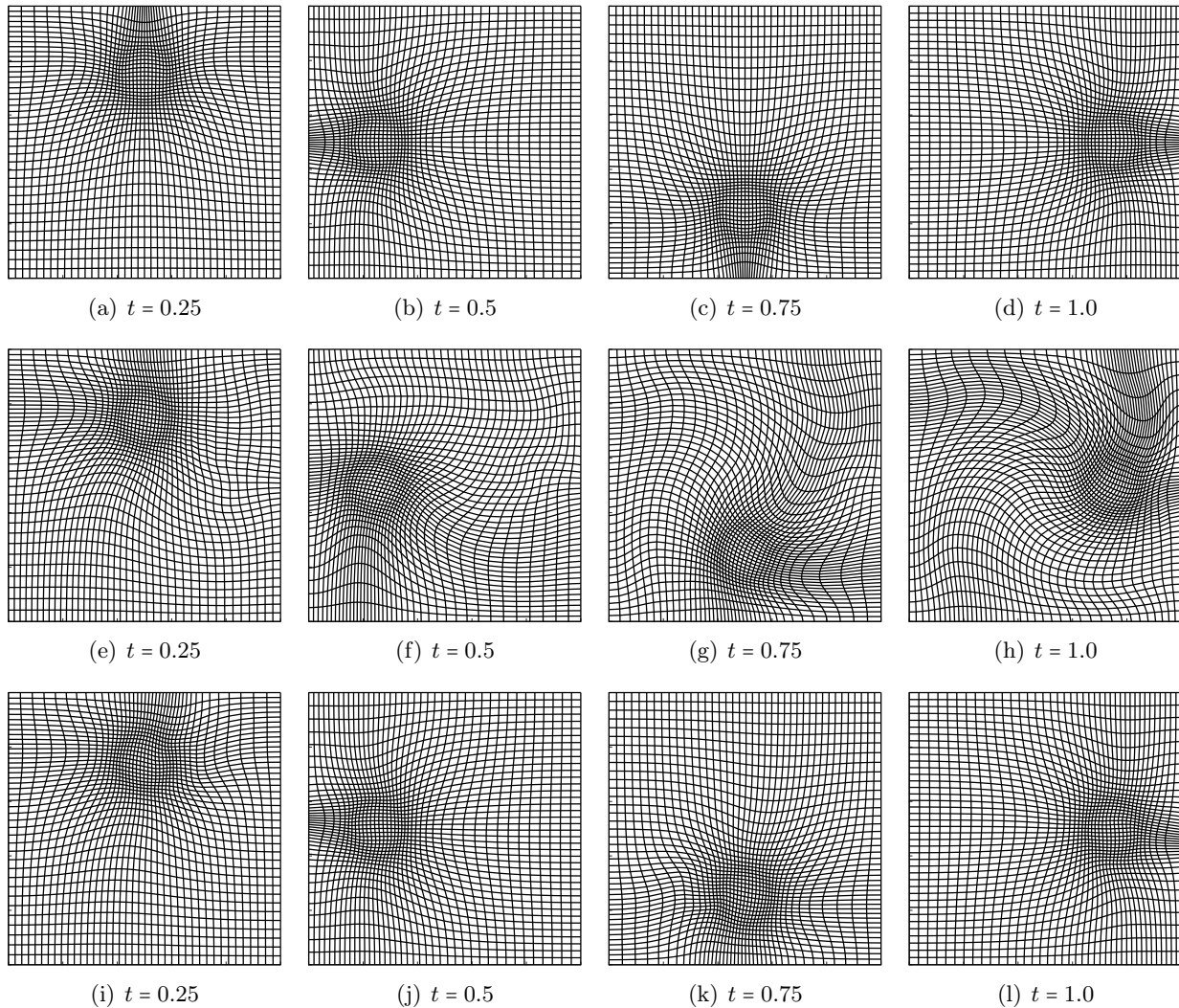


Figure 11: Test problem 5.3: tracking a uniformly rotating patch with target function (42). Shown are plots of the 40^2 cell adaptive meshes at various times t . The meshes are produced using static SAM (top), dynamic SAM (middle), and restarted SAM (bottom). Restarted SAM removes the grid distortion errors associated with Lagrangian methods.

of distortion. Interestingly, the Jacobian errors of dynamic SAM are smaller than static SAM for $t = 0.25$ and $t = 0.5$ due to the high accuracy with which the Poisson problem is solved for in the perturbation formulation. For $t > 0.6$, however, grid distortion errors outweigh the improved accuracy for the Poisson solve, and dynamic SAM errors become larger than static SAM errors. This is demonstrated in Figure 12(a) and Figure 12(b), which provide plots of the evolution of \mathcal{E}_2 and λ , respectively. Restarted SAM combines the best aspects of static and dynamic SAM i.e. smoothness and efficiency, respectively. As shown in the bottom row of Figure 11, and confirmed in Table 5 and Figure 12, restarted SAM grids are of comparable accuracy and smoothness to static SAM grids, but require essentially the same amount of computational expense as dynamic SAM.

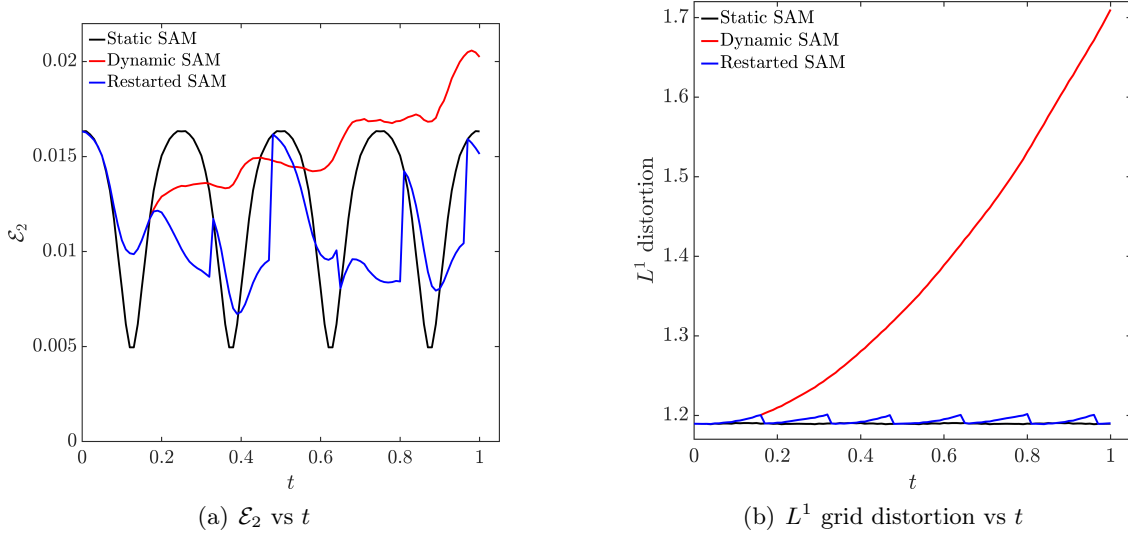


Figure 12: Test problem 5.3: tracking a uniformly rotating patch. Shown are (a) L^2 Jacobian error \mathcal{E}_2 and (b) L^1 grid distortion history of the grids produced using static, dynamic, and restarted SAM. Restarted SAM efficiently controls grid distortion and Jacobian errors.

5.4. Differential rotation with small scales

5.4.1. Problem description. Our final dynamic mesh generation test models a Gaussian “blob” deforming under a rotating flow in which the angular velocity is dependent upon the distance from the center of the blob [18]. The time-dependent target Jacobian function is defined as

$$\bar{G}(y, t) = \frac{1}{1 + 4 \exp \left[-r(y)^2 \left(\frac{\cos^2 \theta_0(y, t)}{\sigma_1} + \frac{\sin^2 \theta_0(y, t)}{\sigma_2} \right) \right]}, \quad (44)$$

where $r(y) = |y - 0.5|$ is the radial coordinate, $\theta_0(y, t) = \theta(y) + \omega(r)t$, and $\theta(y) = \arctan \left(\frac{y^2 - 0.5}{y^1 - 0.5} \right)$. The parameters σ_1 and σ_2 control the aspect ratio of the blob, while $\omega(r)$ is the angular velocity. As in [18], we set $\sigma_1 = 0.05$, $\sigma_2 = 0.001$, and

$$\omega(r) = 1.6 \max [(0.5 - r)r, 0].$$

The function (44) describes the evolution of an initially smooth Gaussian blob $\bar{G}(y, 0)$ advected by an incompressible velocity field $V = (V_r, V_\theta) = (0, r\omega(r))$, where V_r and V_θ are the velocity components in the r and θ directions, respectively. The initial blob is smooth but will develop arbitrarily small scales for $t > 0$ due to the radial dependence of the angular velocity. As in [18], we set the grid resolution at $N = 128^2$, the time-step as $\Delta t = 1$, and generate a sequence of meshes for $0 \leq t \leq 90$. The final grid at $t = 90$ computed with static SAM is shown in Figure 13.

5.4.2. Comparison of static, dynamic, and restarted SAM. The results of static, dynamic, and restarted SAM simulations are provided in Figure 14, which shows zoomed-in plots of the meshes near $(0.5, 0.5)$ at various times t . All three schemes produce grids that are untangled, but while static SAM grids are smooth, the dynamic SAM grids contain more distorted elements. This is confirmed in Figure 15, which provides plots of the time history of the L^2 Jacobian error (17) and L^1 distortion (36). Static and dynamic SAM produce grids with similar Jacobian errors, but while

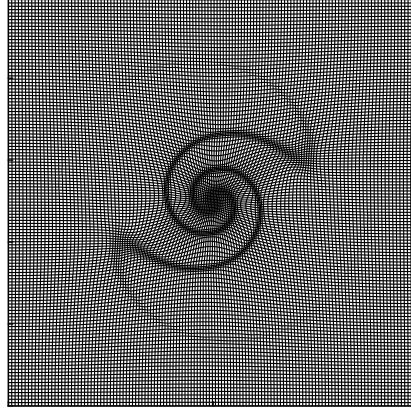


Figure 13: Test problem 5.4: tracking small scale vortical structures in flows with differential rotation. Shown is the 128^2 cell mesh at the final time $t = 90$ computed using static SAM with the target function (44). This figure can be compared with Figure 8 in [18].

static SAM grids have mean distortion of ≈ 1.0375 , the distortion of dynamic SAM grids increases monotonically to ≈ 1.085 at $t = 90$.

On the other hand, the total CPU runtime is 34.6 seconds vs 10.2 seconds for static SAM vs dynamic SAM. For restarted SAM, the restart criterion $\lambda_k > \Lambda\lambda_{\text{ref}}$ forces the grid to reset a total of 6 times during the simulation. As shown in Figure 15 and in the final row of Figure 14, the restarted SAM grids are smooth and comparable to static SAM grids. The CPU runtime for restarted dynamic SAM is only 12.1 seconds, a mild increase over the dynamic SAM runtime.

A comparison of Figure 15 with Fig. 10 from [18] shows that the MK grids are of similar quality to static and restarted dynamic SAM. Our previous numerical experiments (c.f. Table 3) indicate that each static SAM mesh generation at $N = 128^2$ cell resolution is more than 50 times faster than each MK mesh generation. We can thus estimate that, for the current example, restarted SAM is at least $50 \times \frac{34.6}{12.1} \approx 143$ times faster than MK mesh generation.

6. SAM-ALE SCHEME FOR GAS DYNAMICS

We next couple our SAM scheme to a very simple FD WENO-based ALE scheme. The purpose of this section is to demonstrate the ability of SAM-ALE to reproduce high-resolution uniform runs using fewer cells and less total CPU time. The numerical method for the ALE system of equations we use is highly simplified and not meant to be representative of the full class of ALE solvers. Nonetheless, even for the two very difficult test problems presented in Section 7, the highly simplified scheme performs remarkably well.

For the notation used in this section, we refer the reader to Section 2.

6.1. The 2D ALE-Euler system

6.1.1. Equations in Eulerian coordinates. The 2D compressible Euler system in Eulerian coordinates $y = (y^1, y^2) \in \Omega$ can be written in the following compact conservation-law form

$$\partial_t \mathbf{Q} + D_i \mathbf{F}^i(\mathbf{Q}) = 0, \quad (y, t) \in \Omega \times (0, T), \quad (45a)$$

$$\mathbf{Q}(y, 0) = \mathbf{Q}_0(y), \quad (y, t) \in \Omega \times \{0\}. \quad (45b)$$

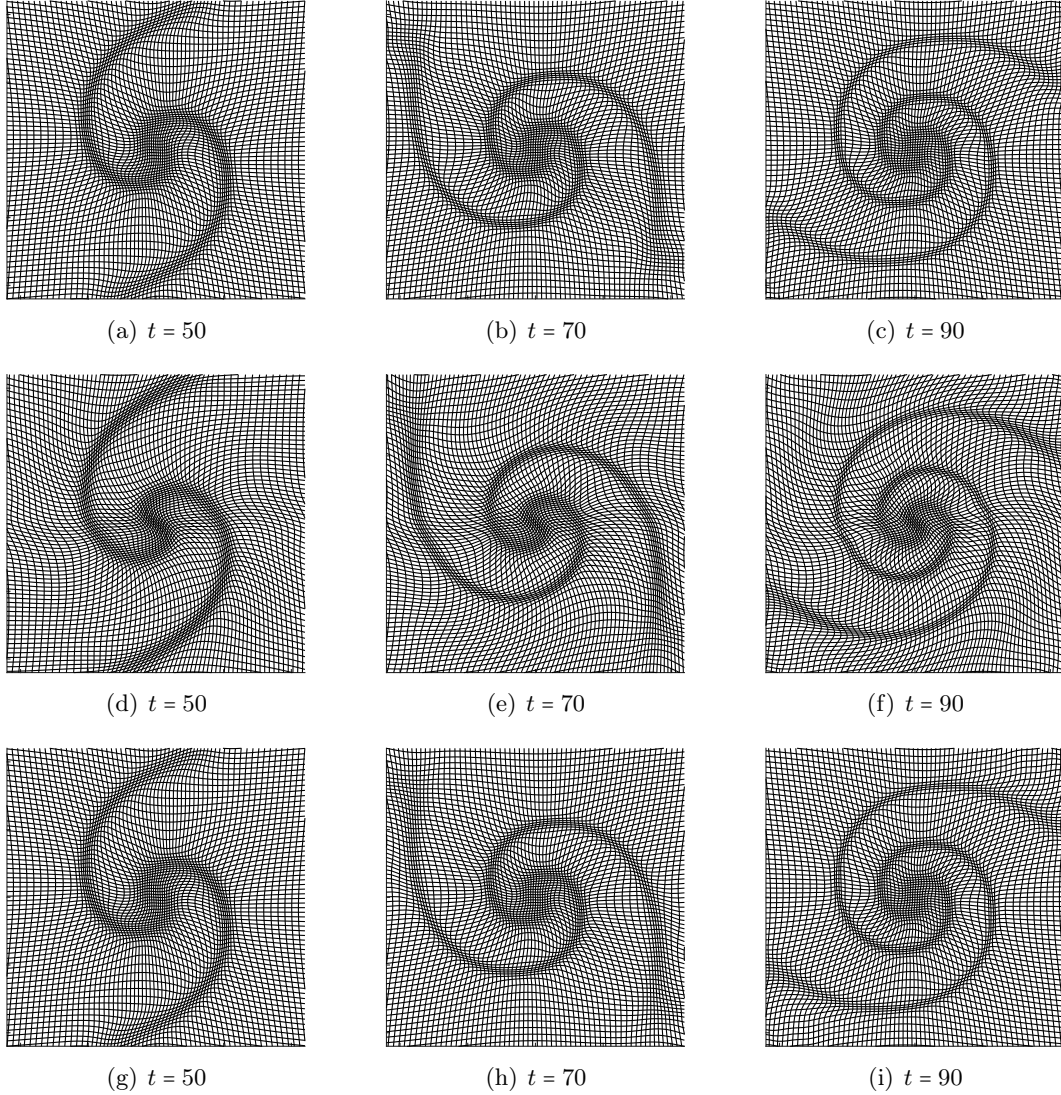


Figure 14: Test problem 5.4: tracking small scale vortical structures in flows with differential rotation using (44). Shown are zoomed in plots of the 128^2 cell adaptive meshes at various times t . The meshes are produced using static SAM (top), dynamic SAM (middle), and restarted dynamic SAM (bottom). Restarted SAM is at least 143 times faster than the MK scheme and produces smooth meshes without the grid distortion errors associated with Lagrangian-type schemes.

Here, Q is the vector of conserved variables, and $F^1(Q)$ and $F^2(Q)$ are the *flux functions*, defined as

$$Q = \begin{pmatrix} \rho \\ \rho u^1 \\ \rho u^2 \\ E \end{pmatrix} \quad \text{and} \quad F^i(Q) = \begin{pmatrix} \rho u^i \\ \rho u^1 u^i + \delta_1^i p \\ \rho u^2 u^i + \delta_2^i p \\ u^i (E + p) \end{pmatrix}. \quad (46)$$

The velocity vector is $u = (u^1, u^2)$ with horizontal component u^1 and vertical component u^2 , $\rho > 0$ is the fluid density (assumed strictly positive), E denotes the energy, and p is the pressure defined by the ideal gas law,

$$p = (\gamma - 1) \left(E - \frac{1}{2} \rho |u|^2 \right), \quad (47)$$

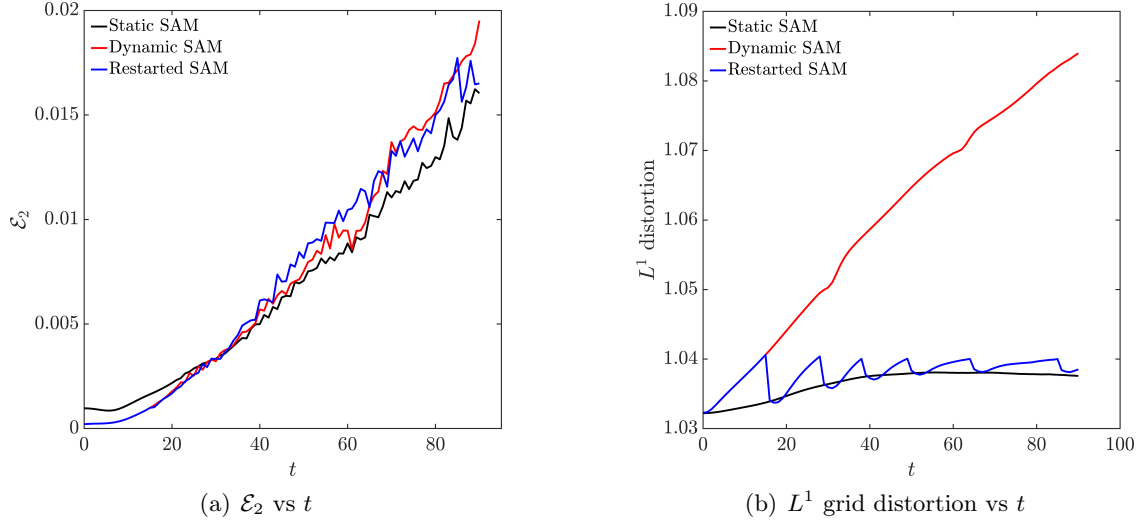


Figure 15: Test problem 5.4: tracking small scale vortical structures in flows with differential rotation using (44). Shown are (a) L^2 Jacobian error \mathcal{E}_2 and (b) L^1 grid distortion history of the grids produced using static, dynamic, and restarted SAM. The errors are comparable to those provided in [18], and restarted SAM controls the grid distortion associated with Lagrangian-type schemes.

where γ is the adiabatic constant, which we will assume takes the value $\gamma = 1.4$, unless otherwise stated.

6.1.2. Equations in ALE coordinates. Let Ω_{ref} be the fixed reference domain with coordinates (x^1, x^2) , and assume that we have, for each $t \geq 0$, a smooth ALE map $\psi(\cdot, t) : \Omega_{\text{ref}} \rightarrow \Omega$. Denote by the regular font f the ALE counterpart to the Eulerian variable written with upright font \mathbf{f} i.e. $f(x, t) = \mathbf{f} \circ \psi(x, t)$. The 2D ALE-Euler system can then be written in conservation law form as

$$\partial_t Q + \partial_j F^j(Q) = 0, \quad (x, t) \in \Omega_{\text{ref}} \times (0, T), \quad (48a)$$

$$Q(x, 0) = Q_0(x), \quad (x, t) \in \Omega_{\text{ref}} \times \{0\}, \quad (48b)$$

where the conserved ALE variables Q and flux functions $F^j(Q)$ are given as

$$Q = \begin{pmatrix} \mathcal{J}\rho \\ \mathcal{J}\rho u^1 \\ \mathcal{J}\rho u^2 \\ \mathcal{J}E \end{pmatrix} \quad \text{and} \quad F^j(Q) = \begin{pmatrix} \rho \alpha_i^j (u^i - \psi_t^i) \\ \rho u^1 \alpha_i^j (u^i - \psi_t^i) + \alpha_1^j p \\ \rho u^2 \alpha_i^j (u^i - \psi_t^i) + \alpha_2^j p \\ E \alpha_i^j (u^i - \psi_t^i) + p \alpha_i^j u^i \end{pmatrix}. \quad (49)$$

Here, α_i^j denotes the components of the cofactor matrix defined by (4), and ψ_t^i is the i^{th} component of the mesh velocity. It is also convenient to introduce the *ALE transport velocity* $v(x, t)$ with j^{th} component $v^j := \frac{1}{\mathcal{J}} \alpha_i^j (u^i - \psi_t^i)$. The flux function F^j is then given as

$$F^j(Q) = \begin{pmatrix} \mathcal{J}\rho v^j \\ \mathcal{J}\rho u^1 v^j + \alpha_1^j p \\ \mathcal{J}\rho u^2 v^j + \alpha_2^j p \\ \mathcal{J}E v^j + p \alpha_i^j u^i \end{pmatrix}. \quad (50)$$

The 2D ALE-Euler system (48) is hyperbolic in the sense that each of $\nabla_Q F^j(Q)$ is diagonalizable with real eigenvalues (or wave speeds), which are given explicitly by

$$\lambda^{j,\pm} = \frac{1}{\mathcal{J}}(v^j \pm c) \quad \text{and} \quad \lambda^{j,0} = \frac{1}{\mathcal{J}}v^j \quad (\text{repeated}), \quad (51)$$

with $c = \sqrt{\gamma p / \rho}$ the sound speed.

6.1.3. Geometric conservation law and free-stream preservation. An explicit computation shows that the Jacobian determinant $\mathcal{J}(x, t)$ satisfies the *geometric conservation law* (GCL) [76]

$$\partial_t \mathcal{J} - \partial_j (a_i^j \psi_t^i) = 0. \quad (52)$$

For (48), an equivalent property to the GCL is the *free-stream preservation property*, which states that an initially uniform flow (i.e. $\mathbf{Q}_0 \equiv \text{constant}$) is preserved under evolution by (48a) i.e. $\mathbf{Q} \equiv \text{constant}$ for every $t > 0$. Numerical schemes that fail to preserve the free-stream produce unacceptably large errors that corrupt small-scale vortical structures [39, 80, 17, 62, 46].

Any sane finite difference scheme preserves the free-stream on static uniform meshes. On dynamic adaptive meshes, however, this is no longer a given, and indeed many standard schemes (including WENO [44]) fail to preserve the free-stream. As such, we design our numerical scheme to ensure free-stream preservation by explicitly incorporating (52) into the system of conservation laws to be solved [39, 84]. Specifically, we append to (48) the equation (52) and consider the modified system

$$\partial_t \tilde{Q} + \partial_j \tilde{F}^j(\tilde{Q}) = 0, \quad (x, t) \in \Omega_{\text{ref}} \times (0, T), \quad (53a)$$

$$\tilde{Q}(x, 0) = \tilde{Q}_0(x), \quad (x, t) \in \Omega_{\text{ref}} \times \{0\}, \quad (53b)$$

with

$$\tilde{Q} = \begin{pmatrix} \mathcal{J} \rho \\ \mathcal{J} \rho u^1 \\ \mathcal{J} \rho u^2 \\ \mathcal{J} E \\ \mathcal{J} \end{pmatrix} \quad \text{and} \quad \tilde{F}^j(\tilde{Q}) = \begin{pmatrix} \mathcal{J} \rho v^j \\ \mathcal{J} \rho u^1 v^j + a_1^j p \\ \mathcal{J} \rho u^2 v^j + a_2^j p \\ \mathcal{J} E v^j + p a_i^j u^i \\ -a_i^j \psi_t^i \end{pmatrix}. \quad (54)$$

We emphasize that, while the cofactor matrix a_i^j is computed directly from the map ψ according to (4), the Jacobian determinant \mathcal{J} is computed (using the same numerical method used for the other equations in (53)) via (52) and *not* by the usual determinant formula $\mathcal{J} = \partial_1 \psi^1 \partial_2 \psi^2 - \partial_1 \psi^2 \partial_2 \psi^1$ *except at the initial time* $t = 0$.

6.2. The C -method for 2D ALE-Euler

Next, we describe some aspects of our numerical framework for solving (53). Specifically, we adapt the C -method, introduced in the Eulerian setting in [66, 67], to the ALE setting. One of the key features of the C -method is space-time smooth tracking of shock/contact fronts and their geometries via so-called C -functions. The C -functions are space-time smoothed versions of localized solution gradients, and are found as the solutions to auxiliary scalar reaction diffusion equations. These C -functions in turn allow us to implement both directionally isotropic (for shock stabilization) and anisotropic (for contact stabilization) artificial viscosity schemes. In particular, the C -method is a PDE-level modification of (53). Consequently, the methods developed in [66, 67] can be implemented in the ALE context in a straightforward manner. For the purposes of brevity, we omit some of the details here and refer the reader to [67] and Appendix A.

6.2.1. WENO-type reconstruction and computation of a_i^j . We discretize the uniform mesh and index the nodes by $x_{r,s} = (x_r^1, x_s^2)$. At each $x_{r,s}$ we construct numerical flux functions $\hat{F}_{r+\frac{1}{2},s}^1$ and $\hat{F}_{r,s+\frac{1}{2}}^2$ that will be used to approximate the derivatives $\partial_1 \tilde{F}^1(\tilde{Q})|_{x_{r,s}}$ and $\partial_2 \tilde{F}^2(\tilde{Q})|_{x_{r,s}}$, respectively. We describe the procedure for $\hat{F}_{r+\frac{1}{2},s}^1$. For ease of notation, we drop the superscript 1 and let $\tilde{F}^1 \equiv \tilde{F}$. Decompose $\tilde{F} = \tilde{F}^v + \tilde{F}^p + \tilde{F}^E + \tilde{F}^{\mathcal{J}}$ with

$$\tilde{F}^v = \begin{pmatrix} \mathcal{J}\rho v^j \\ \mathcal{J}\rho u^1 v^j \\ \mathcal{J}\rho u^2 v^j \\ \mathcal{J}E v^j \\ 0 \end{pmatrix}, \quad \tilde{F}^p = \begin{pmatrix} 0 \\ a_1^j p \\ a_2^j p \\ 0 \\ 0 \end{pmatrix}, \quad \tilde{F}^E = \begin{pmatrix} 0 \\ 0 \\ 0 \\ p a_i^j u^i \\ 0 \end{pmatrix}, \quad \tilde{F}^{\mathcal{J}} = \begin{pmatrix} 0 \\ 0 \\ 0 \\ 0 \\ -a_i^j \psi_t^i \end{pmatrix}. \quad (55)$$

Each component of the advection term \tilde{F}^v is approximated at the half-point $x_{r+\frac{1}{2},s}$ as

$$\hat{F}_{r+\frac{1}{2},s}^v = \text{WENO}(q, \mathcal{J}v^j) := q_{r+\frac{1}{2},s}(\mathcal{J}v^j)_{r+\frac{1}{2},s}, \quad (56)$$

where q denotes one of the variables $q \in \{\rho, \rho u^1, \rho u^2, E\}$ and $q_{r+\frac{1}{2},s}$ is computed using a standard 5th order WENO reconstruction [69] of q with upwinding based on the sign of $(\mathcal{J}v^j)_{r+\frac{1}{2},s}$. The velocity $(\mathcal{J}v^j)_{r+\frac{1}{2},s}$ is computed according to the 4th order average

$$(w)_{r+\frac{1}{2},s} := \frac{-w_{r-1,s} + 7w_{r,s} + 7w_{r+1,s} - w_{r+2,s}}{12}. \quad (57)$$

The additional advection terms $\hat{F}_{r+\frac{1}{2},s}^E$ and $\hat{F}_{r+\frac{1}{2},s}^{\mathcal{J}}$ can be approximated in a similar fashion to (56). The pressure term $\hat{F}_{r+\frac{1}{2},s}^p$ is approximated by the 4th order average (57). Finally, the total flux is given by the sum $\hat{F}_{r+\frac{1}{2},s} = \hat{F}_{r+\frac{1}{2},s}^v + \hat{F}_{r+\frac{1}{2},s}^p + \hat{F}_{r+\frac{1}{2},s}^E + \hat{F}_{r+\frac{1}{2},s}^{\mathcal{J}}$. The semi-discrete scheme for (53) then reads

$$\partial_t \tilde{Q}_{r,s} + \frac{\hat{F}_{r+\frac{1}{2},s}^1 - \hat{F}_{r-\frac{1}{2},s}^1}{\Delta x^1} + \frac{\hat{F}_{r,s+\frac{1}{2}}^2 - \hat{F}_{r,s-\frac{1}{2}}^2}{\Delta x^2} = 0. \quad (58)$$

For free-stream flows, we have that $q_{r,s} \equiv \text{constant}$ and the scheme becomes linear, due to the linear averaging (57). In particular, it is easy to verify that the free-stream is preserved, provided the components of the cofactor matrix a_i^j are computed by 4th order central differencing of the map ψ as

$$[\partial_1 \psi^j]_{r,s} = \frac{\psi_{r-2,s}^j - 8\psi_{r-1,s}^j + 8\psi_{r+1,s}^j - \psi_{r+2,s}^j}{12\Delta x^1}, \quad (59)$$

and similarly for $[\partial_2 \psi^j]_{r,s}$.

To confirm this, we perform a free-stream test on the 50×50 time-dependent moving mesh defined by

$$\begin{cases} \psi^1(x^1, x^2, t) = x^1 + 0.4 \sin\left(\frac{3\pi t}{T}\right) \sin\left(\frac{3\pi}{8}(x^2 + 8)\right) \end{cases} \quad (60a)$$

$$\begin{cases} \psi^2(x^1, x^2, t) = x^2 + 0.8 \sin\left(\frac{3\pi t}{T}\right) \sin\left(\frac{3\pi}{8}(x^1 + 8)\right) \end{cases} \quad (60b)$$

for $(x^1, x^2) \in [-8, +8]^2$ and $0 \leq t \leq T = 80$. The initial data is uniform $U_0 \equiv 1$ and we employ periodic boundary conditions. The magnitude of the density error at the final time $t = T$ is $\|\rho(\cdot, T) - 1\|_{L^\infty} = 9.10 \times 10^{-14}$ i.e. the scheme maintains free stream flows to machine precision.

For non-smooth problems with shocks or contacts, it is necessary to add an artificial viscosity term to the right-hand side of (53a), and the semi-discrete scheme (58) must be modified appropriately. The details of the particular form of artificial viscosity we use is provided in Appendix A.

REMARK 2. The simplified WENO-type reconstruction procedure outlined above is similar in some respects to the WENO schemes based on the so-called *alternative flux formulation*, first introduced in [70] and explored extensively in several recent works [45, 46, 63, 19, 57]. In particular, both schemes define the flux $\hat{F}_{r+\frac{1}{2},s}$ by first reconstructing the variables $q_{r+\frac{1}{2},s}$. On the other hand, the alternative flux formulation WENO schemes utilize characteristic decompositions and (exact or approximate) Riemann solvers. The resulting algorithms are more expensive but also more robust. Nonetheless, for simple problems, both the simplified WENO and alternative flux WENO schemes produce similar results [66, 67]. For more challenging problems, the simplified WENO scheme produces oscillatory solutions; these oscillations can be suppressed with C -method artificial viscosity.

6.2.2. Explicit interface tracking. The C -method utilizes a simple method for tracking of contact discontinuities which we first describe in the Eulerian setting i.e. for the system (45). Let $\mathbf{z} : \mathcal{I} \times [0, T] \rightarrow \Omega$ be a parametrization of the material interface with parameter $\alpha \in \mathcal{I} \subset \mathbb{R}$, and with components $\mathbf{z} = (z^1, z^2)$. In many simulations, the contact discontinuity is a closed or periodic curve, and in this case we take $\mathcal{I} = [-\pi, \pi]$. Given an initial parametrization \mathbf{z}_0 of the contact discontinuity, the interface $\mathbf{z}(\alpha, t)$ is found as the solution to

$$\begin{cases} \partial_t \mathbf{z}(\alpha, t) = \bar{\mathbf{u}} \circ \mathbf{z}(\alpha, t), & \alpha \in \mathcal{I} \text{ and } 0 < t \leq T \\ \mathbf{z}(\alpha, 0) = \mathbf{z}_0(\alpha), & \alpha \in \mathcal{I} \text{ and } t = 0 \end{cases} \quad (61a)$$

$$\quad (61b)$$

Here, the velocity $\bar{\mathbf{u}}$ is defined as the average $\bar{\mathbf{u}} = \frac{1}{2}(\mathbf{u}^+ + \mathbf{u}^-)$, with \mathbf{u}^\pm denoting the fluid velocity on either side of the interface. In a numerical implementation, the average $\bar{\mathbf{u}}$ is approximated by bilinear interpolation of \mathbf{u} onto \mathbf{z} .

The ALE analog of the (Lagrangian) interface tracking algorithm described above can be derived by defining the ALE interface parametrization $z : \mathcal{I} \times [0, T]$ as the image of \mathbf{z} under the action of the inverse ALE map $\psi^{-1} : \Omega \times [0, T] \rightarrow \Omega_{\text{ref}}$ i.e.

$$z(\alpha, t) = \psi^{-1} \circ \mathbf{z}(\alpha, t).$$

If the map ψ resolves mesh points around \mathbf{z} , then the ALE interface z represents a “zoomed-in” version of \mathbf{z} that magnifies small scale structures c.f. Figure 20(d).

A chain rule computation shows that z is the solution to

$$\begin{cases} \partial_t z(\alpha, t) = \bar{\mathbf{v}} \circ z(\alpha, t), & \alpha \in \mathcal{I} \text{ and } 0 < t \leq T \\ z(\alpha, 0) = z_0(\alpha), & \alpha \in \mathcal{I} \text{ and } t = 0 \end{cases} \quad (62a)$$

$$\quad (62b)$$

where $\bar{\mathbf{v}} = \frac{1}{2}(\mathbf{v}^+ + \mathbf{v}^-)$. The initial interface z_0 is defined by

$$z_0(\alpha) = \psi^{-1} \circ \mathbf{z}(\alpha, 0). \quad (63)$$

In a numerical implementation, the initial ALE interface z can be computed as the roots of $\psi_0(z_0) = z_0$ using e.g. Newton’s method.

6.3. Coupled SAM-ALE algorithm

Our SAM algorithm is coupled to the ALE C -method by defining an appropriate target Jacobian function \mathbf{G}_k . In this work, for simplicity, we shall assume that \mathbf{G}_k is explicitly defined, either by some particular formula (as in the Noh test), or via the interface \mathbf{z}_k (for the RT test). Future work will investigate coupling of SAM-ALE by means of balanced monitoring of solution gradients [78]. In the case of RT instability, it is important to use the interface \mathbf{z} to control adaptation since it allows high mesh concentration in KH roll up zones, in contrast to the balanced monitoring approach in which the magnitudes of solution gradients decrease in KH zones due to mixing [74].

The complete SAM-ALE algorithm is provided in Algorithm 4.

Algorithm 4 : COUPLED SAM-ALE

Step 0 : Initialization $t = 0$.

- (a) Define the initial Eulerian data \mathbf{Q}_0 on the uniform mesh $\mathcal{U} \subset \Omega$ and the initial interface parametrization $\mathbf{z}_0(\alpha)$.
- (b) Define the initial target Jacobian function \mathbf{G}_0 on \mathcal{U} . Compute the initial ALE map $\psi_0 : \Omega_{\text{ref}} \rightarrow \Omega$ and adaptive mesh $\mathcal{T}_0 = \psi_0(\mathcal{T}_{\text{ref}}) \subset \Omega$ using static SAM Algorithm 1.
- (c) Define the initial ALE data \mathbf{Q}_0 . Compute the initial ALE interface z_0 using Newton's method.

Step 1 : Time-stepping $t = t_k \geq 0$. Assume that we are given all quantities at $t = t_k$.

- (a) Define the target Jacobian function \mathbf{G}_{k+1} and compute the map ψ_{k+1} and adaptive mesh \mathcal{T}_{k+1} according to restarted dynamic SAM Algorithm 3.
 - (b) Compute the cofactor matrix a_i^j using (59). Define the mesh velocity $\partial_t \psi_{k+1} = \frac{\psi_{k+1} - \psi_k}{\Delta t}$.
 - (c) Compute the ALE variables \tilde{Q}_{k+1} and z_{k+1} using the C -method and RK4 time-stepping. The mesh, cofactor matrix, and mesh velocity are kept fixed over the time step.
 - (d) Compute the interface $\mathbf{z}_{k+1} = \psi_{k+1} \circ z_{k+1}$.
 - (e) If $t_{k+1} = T$, then stop; else, set $t = t_{k+1}$ and return to **Step 1(a)**.
-

7. SAM-ALE SIMULATIONS OF GAS DYNAMICS

7.1. Noh implosion

The first test is the 2D Noh implosion: an initially cold gas is directed towards the origin with speed 1 and instantaneously implodes at the origin, resulting in a radially symmetric infinite strength shock propagating outwards with speed 1/3. This is an extremely difficult test problem and almost all codes report errors in the form of wall heating, lack of symmetry, incorrect shock speeds, or even failure to run [55]. This is the case for both Lagrangian-type codes with artificial viscosity [54, 7, 20], as well as sophisticated AMR codes such as RAGE [31]. Extensive numerical testing in [77] showed that catastrophic anomalies occur in AMR solutions, with the anomalies persisting, or even worsening as the grid is refined. These anomalies occur due to spurious wave reflections on discontinuous grids [79, 30].

7.1.1. Problem description. The domain is $\Omega = [0, 1]^2$, the adiabatic constant is $\gamma = 5/3$, and the initial data is

$$\begin{bmatrix} \rho_0 \\ (\rho u^1)_0 \\ (\rho u^2)_0 \\ E_0 \end{bmatrix} = \begin{bmatrix} 1 \\ -\cos(\theta) \\ -\sin(\theta) \\ 0.5 + 10^{-6}/(\gamma - 1) \end{bmatrix} \chi_{r>0} + \begin{bmatrix} 1 \\ 0 \\ 0 \\ 0.5 + 10^{-6}/(\gamma - 1) \end{bmatrix} \chi_{r=0}, \quad (64)$$

where $r = |y|$ is the radial coordinate, $\theta \in [0, \frac{\pi}{2})$ is the polar angle, and χ_A is the indicator function on the set A . We employ reflecting boundary conditions on the left and bottom boundaries and use the exact solution to impose the boundary conditions at the top and right boundaries. The problem is run until the final time $T = 2$.

7.1.2. Uniform mesh simulations. We apply the C -method as described in [67] on 50×50 , 100×100 , and 200×200 meshes with time step Δt set so that $\text{CFL} \approx 0.25$. The C -method artificial viscosity coefficients in (73) are fixed as $\beta_u = 0.35$, $\beta_E = 2.5$, and $\mu = 0$. The scatter plots of density vs r in Figure 16 show that the C -method produces stable non-oscillatory solutions that maintain radial symmetry. Moreover, the smooth artificial viscosity almost entirely removes the wall-heating error in the higher resolution runs.

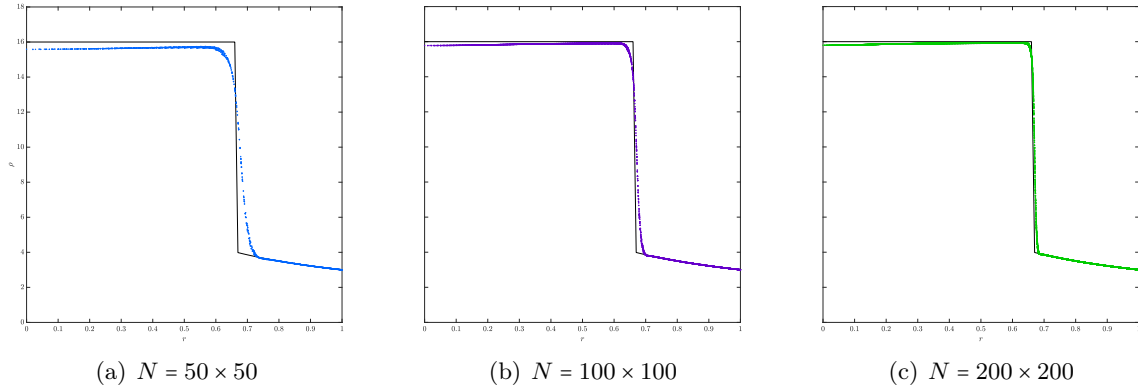


Figure 16: Uniform mesh runs for the 2D Noh problem. Shown are the density scatter plots vs radial coordinate r . The black curve in each subfigure is the exact solution. The shock fronts are sharp and the solutions free of the spurious asymmetry, wall-heating, oscillation, and shock-racing errors associated with the majority of numerical methods for this test.

7.1.3. SAM-ALE simulations. Next, we apply SAM-ALE on a 50×50 dynamic adaptive mesh. For simplicity, we choose a specially designed forcing function G for the mesh generation, defined as

$$C_\psi(y^1, y^2, t) = \exp[-400(r^2 - t^2/9)],$$

$$G(y, t) = \frac{\alpha}{1 + \frac{\delta}{1-\delta} \frac{C_\psi(y, t)}{\int_\Omega C_\psi(y, t) dy}}, \quad (65)$$

where α is a constant chosen so that $\int_\Omega 1/G(y, t) dy = |\Omega| = 1$. This forcing function is designed, using the known analytical solution, to track the moving shock. In the future, a shock-tracking scheme analogous to the z -type advection (61) for contract tracking will be employed to define G . The z -type advection can track the shock with high accuracy, and the resulting G is almost exactly

the same as (65). As such, for simplicity we use the specially designed function (65) in this work, with the understanding that similar results can be obtained when z -type shock tracking is used instead. The particular normalization used to define G is motivated by the balanced monitoring method [78]. We set the time-step as $\Delta t = 5 \times 10^{-4}$, which yields $\text{CFL} \approx 0.2$, and choose artificial viscosity parameters $\beta_u = 0.1$, $\beta_E = 0.7$, and $\mu = 0$.

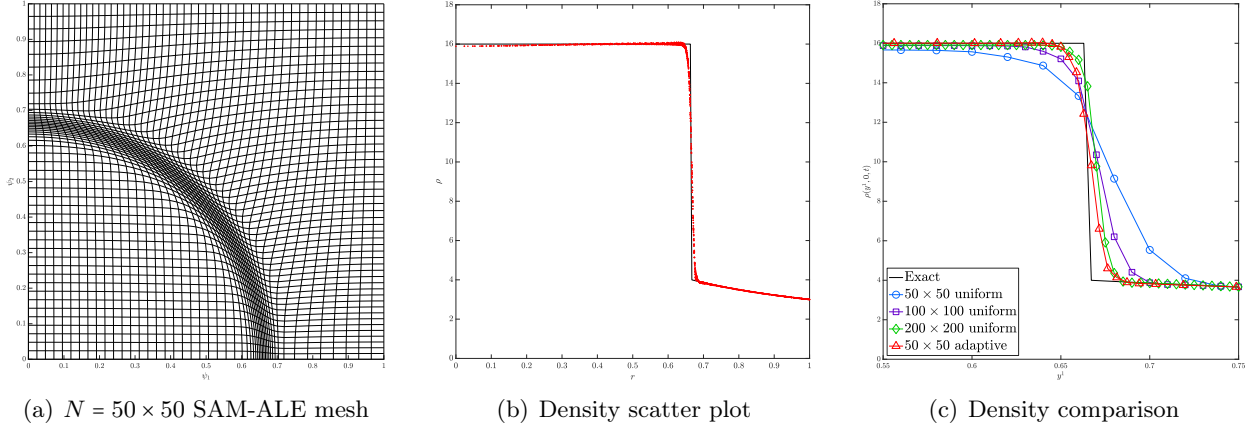


Figure 17: SAM-ALE simulations of the Noh implosion. Shown are (a) adaptive mesh \mathcal{T} , (b) density scatter plot, and (c) comparison of uniform vs SAM-ALE density zoom-in at the shock. The smooth concentration and alignment of the mesh in the vicinity of the shock front allows for a sharp shock representation in the SAM-ALE solution, comparable to the high-resolution 200×200 uniform mesh solution.

The results are shown in Figure 17. The shock front is sharp, the wall-heating error is very small, and solution symmetry is well preserved. The latter is a consequence of both C -method artificial viscosity as well as grid alignment with the shock front. The density cross sections $\rho(y^1, 0, t)$ along the y^1 -axis for the various simulations are shown in Figure 17(c), which clearly shows that the 50×50 adaptive simulation outperforms the low-res and mid-res simulations, and is comparable to the high-res simulation. The wall heating error is smallest for the adaptive simulation, and the sharpness of the shock fronts for the 200×200 uniform and 50×50 adaptive simulations are comparable. As shown in Table 6, the adaptive mesh simulation produces the solution with the smallest L^2 error in the density. Moreover, the adaptive simulation is approximately 6 times faster than the high-res simulation, and requires roughly the same amount of memory as the lowest resolution uniform run.

Simulation	Simulation statistic		
	L^2 density error	CPU time (secs)	Memory usage (MBs)
50×50 uniform	1.019×10^0	4	7.5
100×100 uniform	6.917×10^{-1}	30	14.6
200×200 uniform	5.406×10^{-1}	244	43.7
50×50 adaptive	4.897×10^{-1}	41	7.8

Table 6: Comparison of simulation statistics for the uniform and adaptive mesh C -method simulations for the Noh problem. The low-res SAM-ALE simulation is more accurate than the high-res uniform simulation, while running 6 times faster and requiring only 18% as much memory.

7.2. Rayleigh-Taylor instability

Our second test problem is the classical RT instability. This test poses a huge challenge for Lagrangian and ALE methods due to the complex geometry of the evolving unstable interface. As such, limited RT ALE simulations are available in the literature (but see [86, 59, 25, 35] for some examples). In fact, the RT problem is so challenging for ALE codes that very often the goal is simply to perform a simulation that runs until the final time without excessive mesh tangling, at which point the simulation breaks down [59, 4].

7.2.1. Problem description. We add the source term $\tilde{S}(x, t) = (0, 0, -\mathcal{J}\rho g, -\mathcal{J}\rho g u^2, 0, 0)^T$ to the right-hand side of (53a). The domain is $\Omega = [-0.25, 0.25] \times [0, 1]$ and we apply periodic and free-flow conditions in the y^1 and y^2 directions [65]. The initial data is $u_0 = 0$, and

$$\rho_0 = \begin{cases} 5 - \rho^- g y^2 & , \text{ if } y^2 < 0.5 \\ 5 - 0.5\rho^- g - \rho^+ g(y^2 - 0.5) & , \text{ if } y^2 \geq 0.5 \end{cases}, \quad (66a)$$

$$\rho_0(y^1, y^2) = \rho^- + \frac{\rho^+ - \rho^-}{2} \left[1 + \tanh\left(\frac{y^2 - \eta_0(y^1)}{h}\right) \right], \quad (66b)$$

where $\rho^+ = 2$ and $\rho^- = 1$, $\eta_0(y^1) = 0.5 - 0.01 \cos(4\pi y^1)$, $h = 0.005$, and $g = 1$. The problem is run until the final time $T = 2.5$.

7.2.2. Uniform mesh simulations. We compute a sequence of uniform mesh simulations for resolutions $N = 64 \times 128$ through $N = 512 \times 1024$ with $\text{CFL} \approx 0.45$. The artificial viscosity parameters are set as $\mu = 7.5 \times 10^{-4}$ and $\beta_u = \beta_E = 0$, and we show heatmap plots of the density in Figure 18. As the resolution is increased, more small-scale structure can be seen in the main KH roll up region. The artificial viscosity term suppresses further secondary instabilities that usually occur with other dimensionally split numerical methods [55, 1].

7.2.3. Mesh generation with large zoom-in factor. Next, we aim to produce a 64×128 adaptive mesh with large zoom-in factor that resolves around the material interface \mathbf{z} and define a target Jacobian function as

$$\mathbf{G}_\delta(y, t) = 1 - \delta \exp\left(-\left|\sigma \min_\alpha |y - \mathbf{z}(\alpha, t)|\right|^2\right), \quad (67)$$

with $\sigma = 25$. For this resolution, the meshes produced with dynamic SAM contain non-convex elements for δ larger than approximately 0.85, as shown in Figure 19(a). These non-convex elements arise due to a strong cusp-type flow in the region between the ‘‘stem’’ of the mushroom and the roll up region. The choice $\delta = 0.85$ produces a mesh with smallest cell size only approximately 3.8 times smaller than a uniform mesh cell. Increasing the value of δ further produces a mesh with more non-convex elements, which in turn causes spurious errors in the computed numerical solution as shown in Figure 19(b).

A simple technique to resolve this issue is to use the large zoom-in algorithm described in Section 5.1. Specifically, we use the large mesh zoom-in algorithm (with 25 sub time steps) in combination with restarted dynamic SAM. The 64×128 adaptive mesh with $\delta = 0.97$ is shown in Figure 19(c), from which it can be seen that the mesh is smooth and all elements are convex. The smallest cell size in the mesh is approximately 13.5 times smaller than a uniform cell. The large mesh zoom-in algorithm is applied only when the mesh resets, and the increase in CPU runtime is therefore negligible.

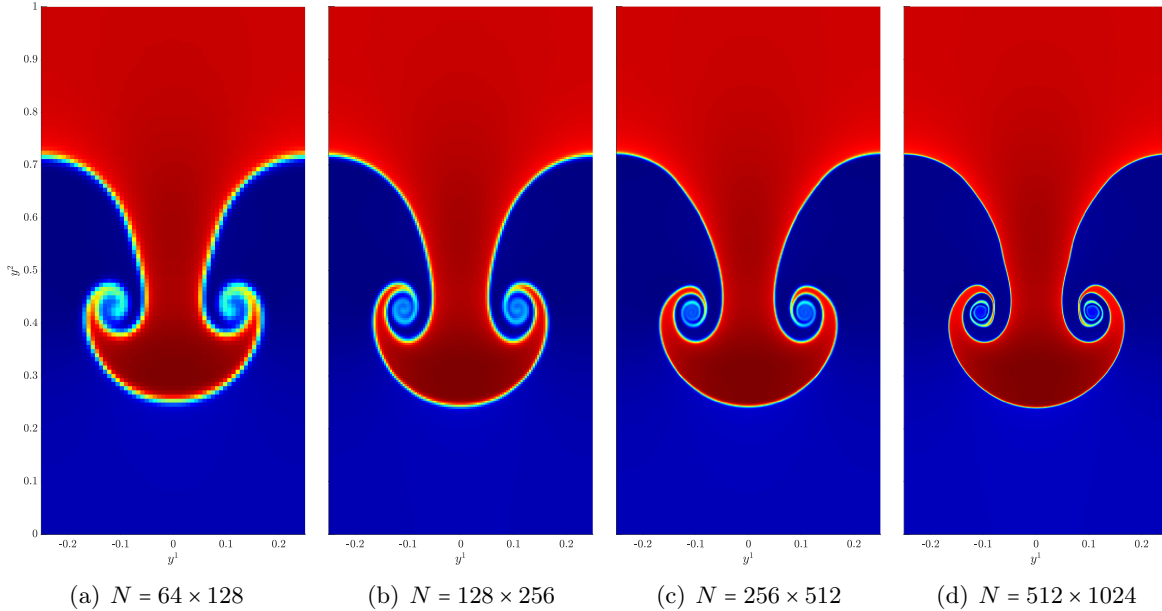


Figure 18: Uniform mesh simulations of RT instability with sharper fronts and more small scale structure in the KH zone as the resolution increases.

7.2.4. Comparison of adaptive and uniform simulations. We perform a 64×128 cell SAM-ALE simulation with zoom-in parameter $\delta = 0.97$ and $\Delta t = 1.5625 \times 10^{-4}$. Plots of the adaptive mesh and density heatmap are provided in Figure 20(a) and Figure 20(b), and we refer to Figure 19(c) for the mesh zoom-in. A comparison with the uniform mesh simulations in Figure 18 shows that the 64×128 SAM-ALE simulation has a much sharper interface and exhibits more small-scale roll-up than the 64×128 uniform simulation, and is roughly comparable to the $N = 256 \times 512$ simulation. However, some of the small-scale structure is not observed in the SAM-ALE density. Interestingly, this roll up is captured by the interface z , shown in Figure 20(c). This suggests that a more robust ALE solver (e.g. WENO with alternative flux formulation) may produce improved results⁹. The ALE interface z is shown in Figure 20(d) and is clearly a zoomed-in version of z , with the small scale KH zones magnified and represented over a much larger region.

Runtime (sec)	Cells				
	64×128	128×256	256×512	512×1024	64×128 SAM-ALE
T_{CPU}	6.9×10^1	4.9×10^2	4.3×10^3	3.78×10^4	1.1×10^3

Table 7: Total CPU runtime for uniform and adaptive simulations of RT instability.

The CPU runtimes of the various simulations are provided in Table 7, from which we see that the SAM-ALE simulation is approximately 4 times and 33 times faster than the 256×512 and 512×1024 uniform runs, respectively. For this problem, the CPU time spent on mesh generation is roughly the same as the time spent on ALE calculations. Since SAM is roughly 50-100 times faster than MK mesh generation, it is clear that an MK-ALE scheme cannot provide a speed-up over uniform mesh simulations. On the other hand, the use of a more robust ALE solver can only improve the relative efficiency of SAM-ALE, since the main computational expense will be the ALE

⁹See also [78] for a comparison of Lax-Friedrichs vs low dissipation HLLC flux reconstruction in the FV framework.

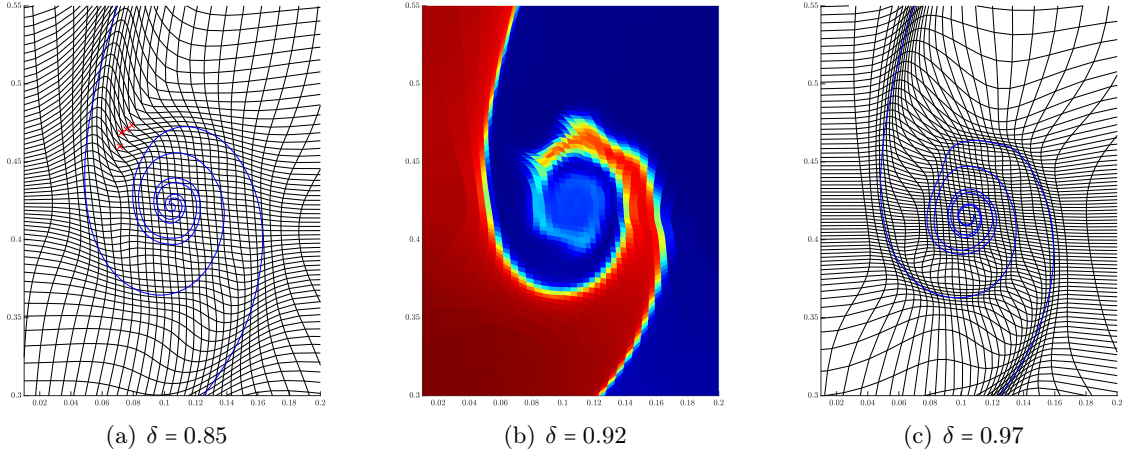


Figure 19: 64×128 adaptive mesh simulations of RT with large zoom-in factor. Figure (a) is a zoom-in of the mesh computed with restarted SAM and $\delta = 0.85$. The interface z is shown as the blue curve, and the non-convex elements are indicated by red crosses. Figure (b) is a zoom-in of the density with $\delta = 0.92$. The non-convex elements cause spurious instabilities along the interface. Figure (c) shows the mesh computed with the large zoom-in algorithm; all the elements are convex and the mesh is smooth.

calculations rather than mesh generation.

The time histories of the L^2 and L^∞ norms of the vorticity ω for the uniform and adaptive mesh simulations are shown in Figure 21. These figures confirm that the 64×128 SAM-ALE run is comparable to the 256×512 uniform run. In fact, for $t \leq 1.75$, when the mesh zoom-in factor is approximately 20 times, the 64×128 SAM-ALE run closely approximates the 512×1024 uniform run. For $t > 1.75$, the mesh zoom-in factor decreases due to the stretching of the interface and the adaptive mesh is no longer able to capture the smallest scales that are present in the 512×1024 run. The decrease in the mesh zoom-in factor is a consequence of the fact that the number of cells in the mesh are fixed. So-called h - r adaptive mesh methods [24] are a way to overcome this issue; the simplicity of our algorithmic framework suggests that a dynamic h - r method based on SAM can be readily formulated and implemented, and this will be investigated in future work.

A. THE C -METHOD FOR 2D ALE-EULER

We provide a brief review of the C -method for adding space-time smooth artificial viscosity to shocks and contacts [67]. The most important feature of the C -method is smooth tracking of shock/contact fronts and their geometries via so-called C -functions. The C -functions are space-time smoothed versions of localized solution gradients, and are found as the solutions to auxiliary scalar reaction diffusion equations. Specifically, we use C to denote a smoothed shock tracking function, and $\vec{\tau}$ to denote the vector valued function $\vec{\tau} = (\tau^1, \tau^2)$. The function τ is a smoothed version of the tangent vector to an evolving contact discontinuity. These C -functions allow us to implement both directionally isotropic (for shock stabilization) and anisotropic (for contact stabilization) artificial viscosity schemes.

To summarize the method, it is convenient to introduce advection, artificial viscosity, and C -equation operators as follows.

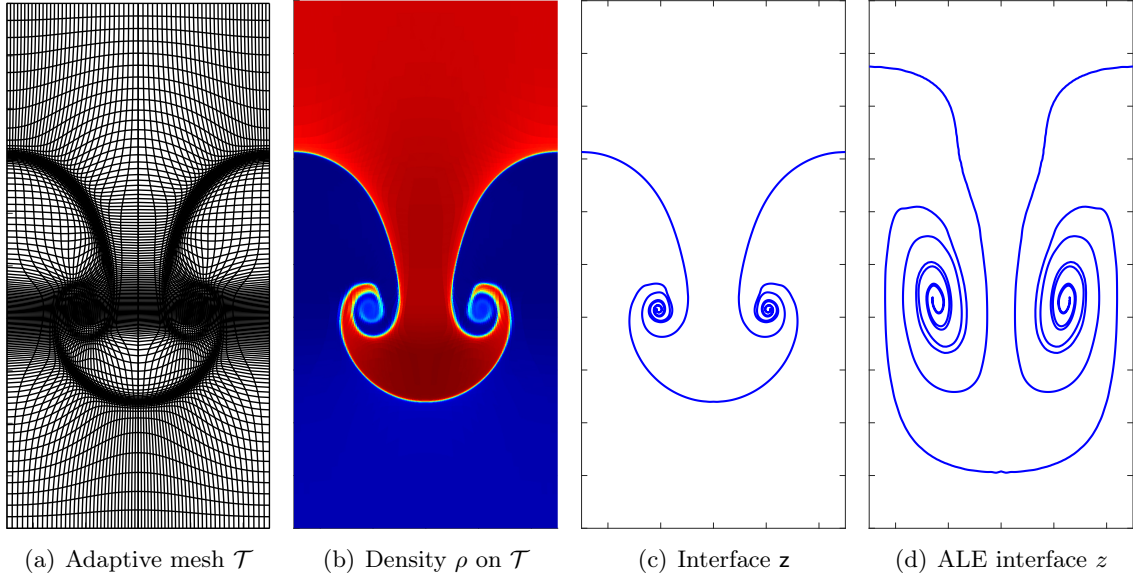


Figure 20: 64×128 SAM-ALE simulation of RT instability with $\delta = 0.97$.

A.0.1. ALE advection operator. For a scalar function $Q : \Omega_{\text{ref}} \rightarrow \mathbb{R}$, and a vector-valued function $v : \Omega_{\text{ref}} \rightarrow \mathbb{R}^2$, define

$$\mathcal{A}[Q; v] := \partial_k (Q a_l^k v^l). \quad (68)$$

A.0.2. ALE isotropic artificial viscosity operator. For a scalar function $Q : \Omega_{\text{ref}} \rightarrow \mathbb{R}$, define

$$\mathcal{D}[Q; \beta] := \partial_k (\tilde{\beta} \rho C a_i^k a_i^l \partial_l Q), \quad (69)$$

with

$$\tilde{\beta} = \frac{|\Delta x|^2}{\max C} \beta.$$

The constant β is an isotropic artificial viscosity parameter for shock stabilization.

A.0.3. ALE anisotropic artificial viscosity operator. For a scalar function $Q : \Omega_{\text{ref}} \rightarrow \mathbb{R}$, we define

$$\mathcal{D}^\tau [Q; \mu] := \partial_k [\tilde{\mu} \rho \tau^i \tau^j a_i^k a_j^l \partial_l Q], \quad (70)$$

with

$$\tilde{\mu} = \frac{|\Delta x|^2}{\alpha^2} \mu. \quad (71)$$

Here, μ is the anisotropic artificial viscosity parameter for contact discontinuity stabilization and $\alpha = \max_x \{|\tau^1|, |\tau^2|\}$.

A.0.4. ALE C-equation operator. For a scalar function $H : \Omega_{\text{ref}} \rightarrow \mathbb{R}$ and scalar forcing function $Q : \Omega_{\text{ref}} \rightarrow \mathbb{R}$, let

$$\mathcal{L}[H; Q] := \frac{\mathcal{S}}{\varepsilon |\Delta x|} (Q - H) + \kappa \mathcal{S} |\Delta x| \Delta H. \quad (72)$$

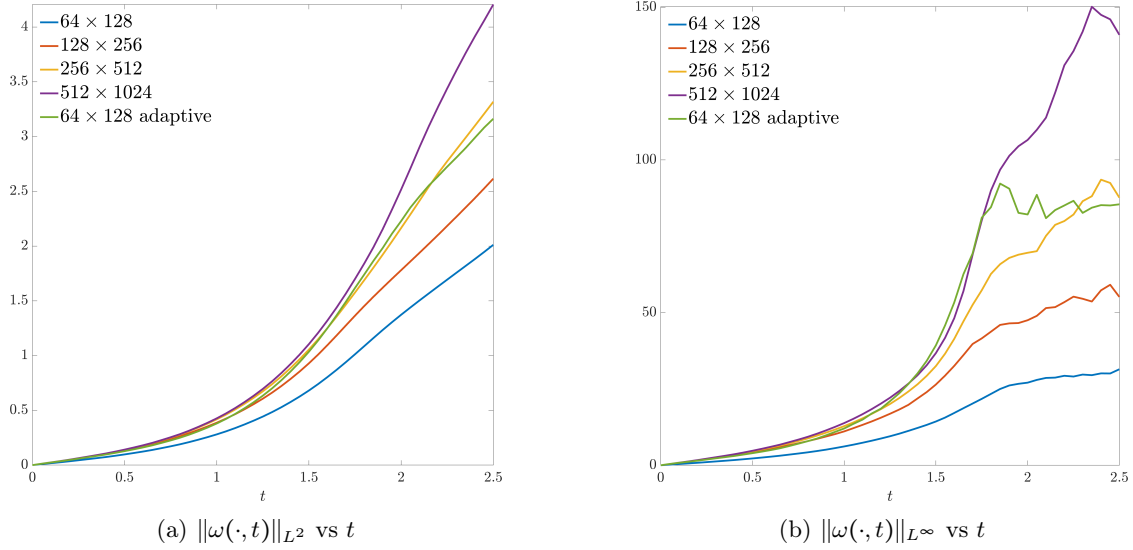


Figure 21: Time history of the L^2 and L^∞ norms of the vorticity for uniform and adaptive mesh simulations of RT instability.

A.0.5. The complete ALE-Euler- C system. Now, we can write the full ALE-Euler- C system as

$$\partial_t(\mathcal{J}\rho) + \mathcal{A}[\rho; u - \psi_t] = 0, \quad (73a)$$

$$\partial_t(\mathcal{J}\rho u^r) + \mathcal{A}[\rho u^r; u - \psi_t] = \mathcal{D}^\tau[u^r; \mu] + \mathcal{D}[u^r; \beta_u] - \partial_j(a_r^j p), \quad \text{for } r = 1, 2, \quad (73b)$$

$$\partial_t(\mathcal{J}E) + \mathcal{A}[E; u - \psi_t] + \mathcal{A}[p; u] = \mathcal{D}[E/\rho; \beta_E], \quad (73c)$$

$$\partial_t \mathcal{J} - \mathcal{A}[1; \psi_t] = 0, \quad (73d)$$

$$\partial_t C - \mathcal{L}[C; F] = 0, \quad (73e)$$

$$\partial_t \tau^r - \mathcal{L}[\tau^r; F^r] = 0, \quad \text{for } r = 1, 2. \quad (73f)$$

The forcing functions for (73e) and (73f) are defined as follows. The shock C forcing function is given by

$$\hat{F} = \frac{|\frac{1}{\mathcal{J}} a_i^j \partial_j \rho|}{\max |\frac{1}{\mathcal{J}} a_i^j \partial_j \rho|}, \quad (74)$$

while the components of the forcing to the contact tangent vector τ equations are defined by

$$F^1 = -\frac{1}{\mathcal{J}} a_2^j \partial_j \rho \quad \text{and} \quad F^2 = \frac{1}{\mathcal{J}} a_1^j \partial_j \rho. \quad (75)$$

The initial conditions for C and τ are defined by solving the time-dependent versions of (73e) and (73f).

B. BOUNDARY SMOOTHING FOR NON-NEUMANN FUNCTIONS

Herein, we describe a simple boundary smoothing technique for non-Neumann functions. Let $x_{\text{mid}}^r = \frac{1}{2}(x_{\text{min}}^r + x_{\text{max}}^r)$, for $r = 1, 2$. Define smooth cutoff functions

$$\begin{aligned}\phi^1(\xi) &= \frac{1}{2} \left[\tanh\left(\frac{\xi - (x_{\text{min}}^1 + d_1)}{\varepsilon}\right) - \tanh\left(\frac{\xi - (x_{\text{max}}^1 - d_1)}{\varepsilon}\right) \right], \\ \phi^2(\eta) &= \frac{1}{2} \left[\tanh\left(\frac{\eta - (x_{\text{min}}^2 + d_2)}{\varepsilon}\right) - \tanh\left(\frac{\eta - (x_{\text{max}}^2 - d_2)}{\varepsilon}\right) \right],\end{aligned}$$

where ε is a smoothing parameter, which we choose as $\varepsilon = 0.01$. The function ϕ^1 is equal to 1 in the interior of the domain, then smoothly decreases to 0 at a distance d_1 near the left and right boundaries. The function ϕ^2 behaves similarly. We set $d_r = 0.05(x_{\text{max}}^r - x_{\text{min}}^r)$.

Given a non-Neumann function \mathbf{G} , we first compute the derivatives $D_1\mathbf{G}$, $D_2\mathbf{G}$, and $D_{12}\mathbf{G}$. We then compute

$$\begin{aligned}\mathcal{I}^{(1)}(y^1) &= \int_{x_{\text{mid}}^1}^{y^1} \phi^1(\xi) D_1\mathbf{G}(\xi, x_{\text{mid}}^2) d\xi, \\ \mathcal{I}^{(2)}(y^2) &= \int_{x_{\text{mid}}^2}^{y^2} \phi^2(\eta) D_2\mathbf{G}(x_{\text{mid}}^1, \eta) d\eta, \\ \mathcal{I}^{(3)}(y^1, y^2) &= \int_{x_{\text{mid}}^2}^{y^2} \int_{x_{\text{mid}}^1}^{y^1} \phi^1(\xi) D_{12}\mathbf{G}(\xi, \eta) d\xi d\eta,\end{aligned}$$

and define

$$\mathbf{G}^*(y^1, y^2) := \mathbf{G}(x_{\text{mid}}^1, x_{\text{mid}}^2) + \mathcal{I}^{(1)}(y^1) + \mathcal{I}^{(2)}(y^2) + \mathcal{I}^{(3)}(y^1, y^2).$$

The function \mathbf{G}^* then satisfies $D\mathbf{G}^* \cdot \nu = 0$ on $\partial\Omega$.

C. THE MK SCHEME

The MK scheme solves for the unique [8, 16] diffeomorphism ψ satisfying (8) that minimizes the L^2 displacement $\|\psi(x) - x\|_{L^2}$. The MK formulation is developed by writing $\psi = x + \nabla\Psi$, where Ψ is a scalar potential. The equation governing Ψ is found by minimizing a functional consisting of the L^2 displacement and a local Lagrange multiplier, where the latter is used to enforce the Jacobian constraint (8). The resulting equation for Ψ is fully nonlinear, and the MK scheme uses an iterative Newton-Krylov solver with multigrid preconditioning to find an approximation to the solution Ψ , within some error tolerance ϵ .

C.1. Machine comparison

To reliably compare the runtimes of our static SAM Algorithm 1 with the MK scheme as listed in [22], we need to account for the different machines on which these codes were run. Therefore, we perform the following machine comparison experiment. In [22], the authors also report the CPU runtimes for a deformation method of LIAO AND ANDERSON [52], whose description is provided in the Appendix of [22]. We coded a numerical implementation of this method, which we refer to as LA, and ran the numerical experiments from [22] on our machine. The runtimes for LA on our machine, along with the LA runtimes from Table 3 of [22], are shown in Table 8. These data show that our machine runs approximately 34% to 42% slower than the machine on which the MK simulations in [22] were performed. We shall therefore assume, as a conservative estimate, that our machine is approximately 33% slower than the machine in [22].

Scheme		Cells				
		16 × 16	32 × 32	64 × 64	128 × 128	256 × 256
LA on [22] machine	T_{CPU}	0.2	0.9	3.4	13.6	55.0
LA on our machine	T_{CPU}	0.3	1.2	4.8	18.6	73.7
	% slowdown	51%	35%	42%	37%	34%

Table 8: CPU runtimes for the LA scheme on the machine from [22] and the LA scheme on our machine. The data for the LA scheme in the top row is taken from Table 3 of [22].

Acknowledgements. Research reported in this publication was supported by NSF grant DMS-2007606 and DTRA grant HDTRA11810022. This research was also supported by Defense Nuclear Nonproliferation, NA-22 and NA-24; we note that the views of the authors do not necessarily reflect the views of the USG. This work was also supported by the Laboratory Directed Research and Development Program of the Los Alamos National Laboratory, which is under the auspices of the National Nuclear Security Administration of the U.S. Department of Energy under DOE Contracts W-7405-ENG-36 and LA-UR-10-04291.

We would like to thank the UNM Center for Advanced Research Computing, supported in part by the National Science Foundation, for providing high performance computing resources used in this work.

REFERENCES

- [1] A. S. Almgren, V. E. Beckner, J. B. Bell, M. S. Day, L. H. Howell, C. C. Joggerst, M. J. Lijewski, A. Nonaka, M. Singer, and M. Zingale. CASTRO: A new compressible astrophysical solver. I. Hydrodynamics and self-gravity. *The Astrophysical Journal*, 715(2):1221–1238, may 2010. doi: 10.1088/0004-637x/715/2/1221. URL <https://doi.org/10.1088%2F0004-637x%2F715%2F2%2F1221>.
- [2] A. Averbuch, M. Israeli, and L. Vozovoi. A fast Poisson solver of arbitrary order accuracy in rectangular regions. *SIAM Journal on Scientific Computing*, 19(3):933–952, 1998. doi: 10.1137/S1064827595288589. URL <https://doi.org/10.1137/S1064827595288589>.
- [3] B. N. Azarenok, S. A. Ivanenko, and T. Tang. Adaptive mesh redistribution method based on godunov’s scheme. *Communications in Mathematical Sciences*, 1(1):152–179, 2003.
- [4] A. J. Barlow, P.-H. Maire, W. J. Rider, R. N. Rieben, and M. J. Shashkov. Arbitrary Lagrangian Eulerian methods for modeling high-speed compressible multimaterial flows. *Journal of Computational Physics*, 322:603–665, 2016. ISSN 0021-9991. doi: <https://doi.org/10.1016/j.jcp.2016.07.001>. URL <https://www.sciencedirect.com/science/article/pii/S0021999116302807>.
- [5] M. Berger and P. Colella. Local adaptive mesh refinement for shock hydrodynamics. *Journal of Computational Physics*, 82(1):64–84, 1989. ISSN 0021-9991. doi: [https://doi.org/10.1016/0021-9991\(89\)90035-1](https://doi.org/10.1016/0021-9991(89)90035-1). URL <https://www.sciencedirect.com/science/article/pii/S0021999189900351>.
- [6] J. Brackbill and J. Saltzman. Adaptive zoning for singular problems in two dimensions. *Journal of Computational Physics*, 46(3):342–368, 1982. ISSN 0021-9991. doi: [https://doi.org/10.1016/0021-9991\(82\)90020-1](https://doi.org/10.1016/0021-9991(82)90020-1). URL <https://www.sciencedirect.com/science/article/pii/S0021999182900201>.

- [7] J. Breil. *Numerical methods for Lagrangian and Arbitrary-Lagrangian-Eulerian Hydrodynamic Contribution to the simulation of High-Energy-Density-Physics Problems*. Habilitation à diriger des recherches, Université de Bordeaux, June 2016. URL <https://hal.archives-ouvertes.fr/tel-01467157>.
- [8] Y. Brenier. Polar factorization and monotone rearrangement of vector-valued functions. *Comm. Pure Appl. Math.*, 44(4):375–417, 1991. ISSN 0010-3640. doi: 10.1002/cpa.3160440402. URL <https://doi.org/10.1002/cpa.3160440402>.
- [9] P. Browne, C. Budd, C. Piccolo, and M. Cullen. Fast three dimensional r-adaptive mesh redistribution. *Journal of Computational Physics*, 275:174–196, 2014. ISSN 0021-9991. doi: <https://doi.org/10.1016/j.jcp.2014.06.009>. URL <https://www.sciencedirect.com/science/article/pii/S0021999114004161>.
- [10] G. L. Bryan, M. L. Norman, B. W. O'Shea, T. Abel, J. H. Wise, M. J. Turk, D. R. Reynolds, D. C. Collins, P. Wang, S. W. Skillman, B. Smith, R. P. Harkness, J. Bordner, J. hoon Kim, M. Kuhlen, H. Xu, N. Goldbaum, C. Hummels, A. G. Kritsuk, E. Tasker, S. Skory, C. M. Simpson, O. Hahn, J. S. Oishi, G. C. So, F. Zhao, R. Cen, and Y. L. and. ENZO: AN ADAPTIVE MESH REFINEMENT CODE FOR ASTROPHYSICS. *The Astrophysical Journal Supplement Series*, 211(2):19, mar 2014. doi: 10.1088/0067-0049/211/2/19. URL <https://doi.org/10.1088/0067-0049/211/2/19>.
- [11] C. Budd, B. Leimkuhler, and M. Piggott. Scaling invariance and adaptivity. *Applied Numerical Mathematics*, 39(3):261–288, 2001. ISSN 0168-9274. doi: [https://doi.org/10.1016/S0168-9274\(00\)00036-2](https://doi.org/10.1016/S0168-9274(00)00036-2). URL <https://www.sciencedirect.com/science/article/pii/S0168927400000362>.
- [12] C. J. Budd, W. Huang, and R. D. Russell. Moving mesh methods for problems with blow-up. *SIAM Journal on Scientific Computing*, 17(2):305–327, 1996. doi: 10.1137/S1064827594272025. URL <https://doi.org/10.1137/S1064827594272025>.
- [13] C. J. Budd, W. Huang, and R. D. Russell. Adaptivity with moving grids. *Acta Numerica*, 18: 111-241, 2009. doi: 10.1017/S0962492906400015.
- [14] J. Burkardt. Piecewise Polynomial Package for Fortran90. <http://www.netlib.org/pppack/index.html>, 2007. Accessed: 2021-07-21.
- [15] J. Burkardt. r8lib utility routines for Fortran90. https://people.sc.fsu.edu/~jburkardt/f_src/r8lib/r8lib.html, 2007. Accessed: 2021-07-21.
- [16] L. A. Caffarelli. Interior $W^{2,p}$ estimates for solutions of the Monge-Ampère equation. *Ann. of Math. (2)*, 131(1):135–150, 1990. ISSN 0003-486X. doi: 10.2307/1971510. URL <https://doi.org/10.2307/1971510>.
- [17] X. Cai and F. Ladeinde. Performance of weno scheme in generalized curvilinear coordinate systems. In *46th AIAA Aerospace Sciences Meeting and Exhibit*, page 36, 2008. doi: <https://doi.org/10.2514/6.2008-36>.
- [18] L. Chacón, G. Delzanno, and J. Finn. Robust, multidimensional mesh-motion based on Monge-Kantorovich equidistribution. *Journal of Computational Physics*, 230(1):87–103, 2011. ISSN 0021-9991. doi: <https://doi.org/10.1016/j.jcp.2010.09.013>. URL <https://www.sciencedirect.com/science/article/pii/S0021999110005073>.

- [19] A. J. Christlieb, X. Feng, Y. Jiang, and Q. Tang. A high-order finite difference WENO scheme for ideal magnetohydrodynamics on curvilinear meshes. *SIAM Journal on Scientific Computing*, 40(4):A2631–A2666, 2018. doi: 10.1137/17M115757X. URL <https://doi.org/10.1137/17M115757X>.
- [20] A. W. Cook, M. S. Ulitsky, and D. S. Miller. Hyperviscosity for unstructured ale meshes. *International Journal of Computational Fluid Dynamics*, 27(1):32–50, 2013. doi: 10.1080/10618562.2012.756477. URL <https://doi.org/10.1080/10618562.2012.756477>.
- [21] B. Dacorogna and J. Moser. On a partial differential equation involving the jacobian determinant. *Annales de l’I.H.P. Analyse non linéaire*, 7(1):1–26, 1990. URL <http://eudml.org/doc/78211>.
- [22] G. Delzanno, L. Chacón, J. Finn, Y. Chung, and G. Lapenta. An optimal robust equidistribution method for two-dimensional grid adaptation based on Monge-Kantorovich optimization. *Journal of Computational Physics*, 227(23):9841–9864, 2008. ISSN 0021-9991. doi: <https://doi.org/10.1016/j.jcp.2008.07.020>. URL <https://www.sciencedirect.com/science/article/pii/S0021999108004105>.
- [23] E. Deriaz. Stability conditions for the numerical solution of convection-dominated problems with skew-symmetric discretizations. *SIAM Journal on Numerical Analysis*, 50(3):1058–1085, 2012. ISSN 00361429. URL <http://www.jstor.org/stable/41582935>.
- [24] V. Dobrev, P. Knupp, T. Kolev, K. Mittal, and V. Tomov. hr-adaptivity for nonconforming high-order meshes with the target matrix optimization paradigm. *Engineering with Computers*, pages 1–17, 2021. doi: <https://doi.org/10.1007/s00366-021-01407-6>.
- [25] V. A. Dobrev, T. V. Kolev, and R. N. Rieben. High-order curvilinear finite element methods for lagrangian hydrodynamics. *SIAM Journal on Scientific Computing*, 34(5):B606–B641, 2012. doi: 10.1137/120864672. URL <https://doi.org/10.1137/120864672>.
- [26] J. Duan and H. Tang. Entropy stable adaptive moving mesh schemes for 2d and 3d special relativistic hydrodynamics. *Journal of Computational Physics*, 426:109949, 2021. ISSN 0021-9991. doi: <https://doi.org/10.1016/j.jcp.2020.109949>. URL <https://www.sciencedirect.com/science/article/pii/S0021999120307233>.
- [27] J. Duan and H. Tang. High-order accurate entropy stable adaptive moving mesh finite difference schemes for special relativistic (magneto)hydrodynamics. *Journal of Computational Physics*, 456:111038, 2022. ISSN 0021-9991. doi: <https://doi.org/10.1016/j.jcp.2022.111038>. URL <https://www.sciencedirect.com/science/article/pii/S0021999122001000>.
- [28] A. S. Dvinsky. Adaptive grid generation from harmonic maps on Riemannian manifolds. *Journal of Computational Physics*, 95(2):450–476, 1991. ISSN 0021-9991. doi: [https://doi.org/10.1016/0021-9991\(91\)90285-S](https://doi.org/10.1016/0021-9991(91)90285-S). URL <https://www.sciencedirect.com/science/article/pii/S002199919190285S>.
- [29] H. Feng and S. Zhao. FFT-based high order central difference schemes for three-dimensional Poisson’s equation with various types of boundary conditions. *Journal of Computational Physics*, 410:109391, June 2020. doi: 10.1016/j.jcp.2020.109391.
- [30] B. Fryxell, K. Olson, P. Ricker, F. X. Timmes, M. Zingale, D. Q. Lamb, P. MacNeice, R. Rosner, J. W. Truran, and H. Tufo. FLASH: An adaptive mesh hydrodynamics code for modeling

- astrophysical thermonuclear flashes. *The Astrophysical Journal Supplement Series*, 131(1): 273–334, nov 2000. doi: 10.1086/317361. URL <https://doi.org/10.1086/317361>.
- [31] M. Gittings, R. Weaver, M. Clover, T. Betlach, N. Byrne, R. Coker, E. Dendy, R. Hueckstaedt, K. New, W. R. Oakes, D. Ranta, and R. Stefan. The RAGE radiation-hydrodynamic code. *Computational Science & Discovery*, 1(1):015005, nov 2008. doi: 10.1088/1749-4699/1/1/015005. URL <https://doi.org/10.1088/1749-4699/1/1/015005>.
- [32] M. Grajewski, M. Köster, and S. Turek. Mathematical and numerical analysis of a robust and efficient grid deformation method in the finite element context. *SIAM Journal on Scientific Computing*, 31(2):1539–1557, 2009. doi: 10.1137/050639387. URL <https://doi.org/10.1137/050639387>.
- [33] M. Grajewski, M. Köster, and S. Turek. Numerical analysis and implementational aspects of a new multilevel grid deformation method. *Applied Numerical Mathematics*, 60(8):767–781, 2010. ISSN 0168-9274. doi: <https://doi.org/10.1016/j.apnum.2010.03.017>. URL <https://www.sciencedirect.com/science/article/pii/S0168927410000474>.
- [34] P. Grisvard. *Elliptic Problems in Nonsmooth Domains*. Society for Industrial and Applied Mathematics, 2011. doi: 10.1137/1.9781611972030. URL <https://epubs.siam.org/doi/abs/10.1137/1.9781611972030>.
- [35] J.-L. Guermond, B. Popov, and L. Saavedra. Second-order invariant domain preserving ALE approximation of hyperbolic systems. *Journal of Computational Physics*, 401:108927, 2020. ISSN 0021-9991. doi: <https://doi.org/10.1016/j.jcp.2019.108927>. URL <https://www.sciencedirect.com/science/article/pii/S0021999119306321>.
- [36] P. He and H. Tang. An adaptive moving mesh method for two-dimensional relativistic hydrodynamics. *Communications in Computational Physics*, 11(1):114–146, 2012.
- [37] P. He and H. Tang. An adaptive moving mesh method for two-dimensional relativistic magnetohydrodynamics. *Computers & Fluids*, 60:1–20, 2012.
- [38] T. Hell and A. Ostermann. Compatibility conditions for dirichlet and neumann problems of poisson’s equation on a rectangle. *Journal of Mathematical Analysis and Applications*, 420: 1005–1023, 2014. doi: <https://doi.org/10.1016/j.jmaa.2014.06.034>.
- [39] R. G. Hindman. Generalized coordinate forms of governing fluid equations and associated geometrically induced errors. *AIAA Journal*, 20(10):1359–1367, 1982. doi: 10.2514/3.51196. URL <https://doi.org/10.2514/3.51196>.
- [40] W. Huang. Metric tensors for anisotropic mesh generation. *Journal of Computational Physics*, 204(2):633–665, 2005. ISSN 0021-9991. doi: <https://doi.org/10.1016/j.jcp.2004.10.024>. URL <https://www.sciencedirect.com/science/article/pii/S0021999104004310>.
- [41] W. Huang and R. D. Russell. Moving mesh strategy based on a gradient flow equation for two-dimensional problems. *SIAM Journal on Scientific Computing*, 20(3):998–1015, 1998. doi: 10.1137/S1064827596315242. URL <https://doi.org/10.1137/S1064827596315242>.
- [42] W. Huang and R. D. Russell. *Adaptive moving mesh methods*, volume 174. Springer Science & Business Media, 2010. doi: <https://doi.org/10.1007/978-1-4419-7916-2>.

- [43] W. Huang and W. Sun. Variational mesh adaptation ii: error estimates and monitor functions. *Journal of Computational Physics*, 184(2):619–648, 2003. ISSN 0021-9991. doi: [https://doi.org/10.1016/S0021-9991\(02\)00040-2](https://doi.org/10.1016/S0021-9991(02)00040-2). URL <https://www.sciencedirect.com/science/article/pii/S0021999102000402>.
- [44] G.-S. Jiang and C.-W. Shu. Efficient implementation of weighted ENO schemes. *J. Comput. Phys.*, 126(1):202–228, 1996. ISSN 0021-9991. doi: 10.1006/jcph.1996.0130. URL <https://doi.org/10.1006/jcph.1996.0130>.
- [45] Y. Jiang, C.-W. Shu, and M. Zhang. An alternative formulation of finite difference weighted ENO schemes with Lax–Wendroff time discretization for conservation laws. *SIAM Journal on Scientific Computing*, 35(2):A1137–A1160, 2013. doi: 10.1137/120889885. URL <https://doi.org/10.1137/120889885>.
- [46] Y. Jiang, C.-W. Shu, and M. Zhang. Free-stream preserving finite difference schemes on curvilinear meshes. *Methods and applications of analysis*, 21(1):1–30, 2014. doi: <https://dx.doi.org/10.4310/MAA.2014.v21.n1.a1>.
- [47] P. Knupp, L. G. Margolin, and M. Shashkov. Reference Jacobian Optimization-Based Rezone Strategies for Arbitrary Lagrangian Eulerian Methods. *Journal of Computational Physics*, 176(1):93–128, Feb. 2002. doi: 10.1006/jcph.2001.6969.
- [48] K. Kontomaris, T. J. Hanratty, and J. B. McLaughlin. An Algorithm for Tracking Fluid Particles in a Spectral Simulation of Turbulent Channel Flow. *Journal of Computational Physics*, 103(2):231–242, Dec. 1992. doi: 10.1016/0021-9991(92)90398-I.
- [49] R. Li, T. Tang, and P. Zhang. Moving mesh methods in multiple dimensions based on harmonic maps. *Journal of Computational Physics*, 170(2):562–588, 2001. ISSN 0021-9991. doi: <https://doi.org/10.1006/jcph.2001.6749>. URL <https://www.sciencedirect.com/science/article/pii/S002199910196749X>.
- [50] S. Li and L. Petzold. Moving mesh methods with upwinding schemes for time-dependent pdes. *Journal of Computational Physics*, 131(2):368–377, 1997. ISSN 0021-9991. doi: <https://doi.org/10.1006/jcph.1996.5611>. URL <https://www.sciencedirect.com/science/article/pii/S0021999196956119>.
- [51] S. Li, J. Duan, and H. Tang. High-order accurate entropy stable adaptive moving mesh finite difference schemes for (multi-component) compressible euler equations with the stiffened equation of state, 2022. URL <https://arxiv.org/abs/2202.07989>.
- [52] G. Liao and D. Anderson. A new approach to grid generation. *Applicable Analysis*, 44(3-4):285–298, 1992. doi: 10.1080/00036819208840084. URL <https://doi.org/10.1080/00036819208840084>.
- [53] G. Liao, F. Liu, G. C. de la Pena, D. Peng, and S. Osher. Level-set-based deformation methods for adaptive grids. *Journal of Computational Physics*, 159(1):103–122, 2000. ISSN 0021-9991. doi: <https://doi.org/10.1006/jcph.2000.6432>. URL <https://www.sciencedirect.com/science/article/pii/S0021999100964325>.
- [54] K. Lipnikov and M. Shashkov. A framework for developing a mimetic tensor artificial viscosity for Lagrangian hydrocodes on arbitrary polygonal meshes. *Journal of Computational Physics*, 229(20):7911–7941, 2010. ISSN 0021-9991. doi: <https://doi.org/10.1016/j.jcp.2010.06.045>. URL <https://www.sciencedirect.com/science/article/pii/S0021999110003694>.

- [55] R. Liska and B. Wendroff. Comparison of several difference schemes on 1D and 2D test problems for the Euler equations. *SIAM J. Sci. Comput.*, 25(3):995–1017, 2003. ISSN 1064-8275. doi: 10.1137/S1064827502402120. URL <https://doi.org/10.1137/S1064827502402120>.
- [56] F. Liu, S. Ji, and G. Liao. An adaptive grid method and its application to steady Euler flow calculations. *SIAM Journal on Scientific Computing*, 20(3):811–825, 1998. doi: 10.1137/S1064827596305738. URL <https://doi.org/10.1137/S1064827596305738>.
- [57] Z. Liu, Y. Jiang, M. Zhang, and Q. Liu. High order finite difference weno methods for shallow water equations on curvilinear meshes. *Communications on Applied Mathematics and Computation*, pages 1–44, 2022. doi: <https://doi.org/10.1007/s42967-021-00183-w>.
- [58] D. Long and J. Thuburn. Numerical wave propagation on non-uniform one-dimensional staggered grids. *J. Comput. Phys.*, 230(7):2643–2659, apr 2011. ISSN 0021-9991. doi: 10.1016/j.jcp.2010.12.040. URL <https://doi.org/10.1016/j.jcp.2010.12.040>.
- [59] R. Loubère, P.-H. Maire, M. Shashkov, J. Breil, and S. Galera. Reale: A reconnection-based arbitrary-Lagrangian-Eulerian method. *Journal of Computational Physics*, 229(12):4724–4761, 2010. ISSN 0021-9991. doi: <https://doi.org/10.1016/j.jcp.2010.03.011>. URL <https://www.sciencedirect.com/science/article/pii/S002199911000121X>.
- [60] D. Luo, W. Huang, and J. Qiu. A quasi-lagrangian moving mesh discontinuous galerkin method for hyperbolic conservation laws. *Journal of Computational Physics*, 396:544–578, 2019. ISSN 0021-9991. doi: <https://doi.org/10.1016/j.jcp.2019.06.061>. URL <https://www.sciencedirect.com/science/article/pii/S0021999119304693>.
- [61] P. MacNeice, K. M. Olson, C. Mobarry, R. de Fainchtein, and C. Packer. Paramesh: A parallel adaptive mesh refinement community toolkit. *Computer Physics Communications*, 126(3): 330–354, 2000. ISSN 0010-4655. doi: [https://doi.org/10.1016/S0010-4655\(99\)00501-9](https://doi.org/10.1016/S0010-4655(99)00501-9). URL <https://www.sciencedirect.com/science/article/pii/S0010465599005019>.
- [62] T. Nonomura, N. Iizuka, and K. Fujii. Freestream and vortex preservation properties of high-order WENO and WCNS on curvilinear grids. *Computers & Fluids*, 39(2):197–214, 2010. doi: <https://doi.org/10.1016/j.compfluid.2009.08.005>.
- [63] T. Nonomura, D. Terakado, Y. Abe, and K. Fujii. A new technique for freestream preservation of finite-difference weno on curvilinear grid. *Computers & Fluids*, 107:242–255, 2015. ISSN 0045-7930. doi: <https://doi.org/10.1016/j.compfluid.2014.09.025>. URL <https://www.sciencedirect.com/science/article/pii/S0045793014003624>.
- [64] H. S. Pathak and R. K. Shukla. Adaptive finite-volume weno schemes on dynamically redistributed grids for compressible euler equations. *Journal of Computational Physics*, 319:200–230, 2016.
- [65] R. Ramani and S. Shkoller. A multiscale model for Rayleigh-Taylor and Richtmyer-Meshkov instabilities. *J. Comput. Phys.*, 405:109177, 2020. doi: 10.1016/j.jcp.2019.109177. URL <https://doi.org/10.1016/j.jcp.2019.109177>.
- [66] R. Ramani, J. Reisner, and S. Shkoller. A space-time smooth artificial viscosity method with wavelet noise indicator and shock collision scheme, Part 1: The 1-D case. *Journal of Computational Physics*, 387:81–116, 2019. ISSN 0021-9991. doi: <https://doi.org/10.1016/j.jcp.2019.02.049>. URL <https://www.sciencedirect.com/science/article/pii/S0021999119301664>.

- [67] R. Ramani, J. Reisner, and S. Shkoller. A space-time smooth artificial viscosity method with wavelet noise indicator and shock collision scheme, Part 2: The 2-*D* case. *J. Comput. Phys.*, 387:45–80, 2019. ISSN 0021-9991. doi: 10.1016/j.jcp.2019.02.048. URL <https://doi.org/10.1016/j.jcp.2019.02.048>.
- [68] B. Semper and G. Liao. A moving grid finite-element method using grid deformation. *Numerical Methods for Partial Differential Equations*, 11:603–615, 1995. doi: <https://doi.org/10.1002/num.1690110606>.
- [69] C.-W. Shu. *Essentially non-oscillatory and weighted essentially non-oscillatory schemes for hyperbolic conservation laws*, pages 325–432. Springer Berlin Heidelberg, Berlin, Heidelberg, 1998. ISBN 978-3-540-49804-9. doi: 10.1007/BFb0096355. URL <https://doi.org/10.1007/BFb0096355>.
- [70] C.-W. Shu and S. Osher. Efficient Implementation of Essentially Non-oscillatory Shock-Capturing Schemes. *Journal of Computational Physics*, 77(2):439–471, Aug. 1988. doi: 10.1016/0021-9991(88)90177-5.
- [71] J. M. Stone, T. A. Gardiner, P. Teuben, J. F. Hawley, and J. B. Simon. Athena: A new code for astrophysical MHD. *The Astrophysical Journal Supplement Series*, 178(1):137–177, sep 2008. doi: 10.1086/588755. URL <https://doi.org/10.1086/588755>.
- [72] M. Sulman, J. Williams, and R. Russell. Optimal mass transport for higher dimensional adaptive grid generation. *Journal of Computational Physics*, 230(9):3302–3330, 2011. ISSN 0021-9991. doi: <https://doi.org/10.1016/j.jcp.2011.01.025>. URL <https://www.sciencedirect.com/science/article/pii/S0021999111000507>.
- [73] M. M. Sulman, J. Williams, and R. D. Russell. An efficient approach for the numerical solution of the Monge-Ampère equation. *Applied Numerical Mathematics*, 61(3):298–307, 2011. ISSN 0168-9274. doi: <https://doi.org/10.1016/j.apnum.2010.10.006>. URL <https://www.sciencedirect.com/science/article/pii/S0168927410001819>.
- [74] H. Tang and T. Tang. Adaptive mesh methods for one- and two-dimensional hyperbolic conservation laws. *SIAM Journal on Numerical Analysis*, 41(2):487–515, 2003. doi: 10.1137/S003614290138437X. URL <https://doi.org/10.1137/S003614290138437X>.
- [75] T. Tang. Moving mesh methods for computational fluid dynamics. In *Recent advances in adaptive computation*, volume 383 of *Contemp. Math.*, pages 141–173. Amer. Math. Soc., Providence, RI, 2005. doi: 10.1090/conm/383/07162. URL <https://doi.org/10.1090/conm/383/07162>.
- [76] P. D. Thomas and C. K. Lombard. Geometric Conservation Law and Its Application to Flow Computations on Moving Grids. *AIAA Journal*, 17(10):1030–1037, Oct. 1979. doi: 10.2514/3.61273.
- [77] F. X. Timmes, G. Gisler, and G. M. Hrbek. Automated analyses of the tri-lab verification test suite on uniform and adaptive grids for code project a, 2005.
- [78] A. van Dam, P. A. Zegeling, et al. Balanced monitoring of flow phenomena in moving mesh methods. *Communications in Computational Physics*, 7(1):138, 2010. doi: 10.4208/cicp.2009.09.033.

- [79] R. Vichnevetsky and L. Turner. Spurious scattering from discontinuously stretching grids in computational fluid dynamics. *Applied Numerical Mathematics*, 8(3):289–299, 1991. ISSN 0168-9274. doi: [https://doi.org/10.1016/0168-9274\(91\)90058-8](https://doi.org/10.1016/0168-9274(91)90058-8). URL <https://www.sciencedirect.com/science/article/pii/0168927491900588>.
- [80] M. R. Visbal and D. V. Gaitonde. On the use of higher-order finite-difference schemes on curvilinear and deforming meshes. *Journal of Computational Physics*, 181(1):155–185, 2002. doi: <https://doi.org/10.1006/jcph.2002.7117>.
- [81] R. Wang, H. Feng, and R. J. Spiteri. Observations on the fifth-order weno method with non-uniform meshes. *Applied Mathematics and Computation*, 196(1):433–447, 2008. ISSN 0096-3003. doi: <https://doi.org/10.1016/j.amc.2007.06.024>. URL <https://www.sciencedirect.com/science/article/pii/S0096300307006972>.
- [82] A. M. Winslow. Numerical solution of the quasilinear poisson equation in a nonuniform triangle mesh. *Journal of Computational Physics*, 1(2):149–172, 1966. ISSN 0021-9991. doi: [https://doi.org/10.1016/0021-9991\(66\)90001-5](https://doi.org/10.1016/0021-9991(66)90001-5). URL <https://www.sciencedirect.com/science/article/pii/0021999166900015>.
- [83] A. M. Winslow. Adaptive-mesh zoning by the equipotential method. *UCID-19062, Lawrence Livermore National Laboratory*, 4 1981. doi: 10.2172/6227449. URL <https://www.osti.gov/biblio/6227449>.
- [84] X. Yang, W. Huang, and J. Qiu. A moving mesh weno method for one-dimensional conservation laws. *SIAM Journal on Scientific Computing*, 34:A2317–A2343, 01 2012. doi: 10.1137/110856381.
- [85] P. K. Yeung and S. B. Pope. An Algorithm for Tracking Fluid Particles in Numerical Simulations of Homogeneous Turbulence. *Journal of Computational Physics*, 79(2):373–416, Dec. 1988. doi: 10.1016/0021-9991(88)90022-8.
- [86] P. A. Zegeling, W. D. de Boer, and H. Z. Tang. Robust and efficient adaptive moving mesh solution of the 2-D Euler equations. In *Recent advances in adaptive computation*, volume 383 of *Contemp. Math.*, pages 375–386. Amer. Math. Soc., Providence, RI, 2005. doi: 10.1090/conm/383/07179. URL <https://doi.org/10.1090/conm/383/07179>.